UNIVERSITÀ DEGLI STUDI DI NAPOLI FEDERICO II

Scuola Politecnica e delle Scienze di Base

PhD course in Industrial Engineering (XXXII Cycle)

Department of Industrial Engineering

Doctoral Thesis

New techniques for quasi-isothermal volumetric machines and their use in thermodynamic cycles.

COORDINATORE

Ch.mo Prof. Ing. Michele Grassi

TUTOR

Ch.mo Prof. Ing. Massimo Cardone

CANDIDATO

Ing. Bonaventura Gargiulo

A.D. 2020

Acknowledgements

A body, though one, has many parts, but all its many parts form one body (1Corinthiants 12,12)

I must start acknowledging the former professor Raffaele Cozzolino, who started this project and even now it continues to give his practical and theoretical support to all of us. His experience and his lateral thinking approach have been priceless.

Right after, I really have to thank my tutor, Prof. Massimo Cardone, who gave me the actual possibility to experience the laboratory and deepen my knowledge on the acquisition systems. His support throughout the experimental activities was essential to solve many technical problems.

I also thank Mr. Salvatore De Cristofaro. You have been not only an essential aid, but also a great friend. Thank you for all those mornings when you listen to me.

To Dr. Pierpaolo Ricci, Dr. Fabio Vollaro and Ing. Giampaolo Trombetta. Our paths are not the same anymore but thank you for the time we worked together.

I would like to acknowledge Mr. Luigi Galano, Mr. Paolo Galano, Mr. Ernesto Scarpati and Mr. Luigi Gargiulo for the mechanical machining. You all made me feel at home: thank you.

To all my dear friends. I know. I was cold, I was absent, I was not the good friend you though I were. I'm sorry.

At the time you gave me life and now you keep me sane. For sure, I would not be here without you. My dear family, whatever acknowledgement would be insufficient. Nevertheless, thank you.

To God. I cannot see You, because You are behind me, supporting me, giving me strength, and pushing me forward. Thank You for Your mercy.

Abstract

This work deals with the usage of miniaturized exchangers to cool down a compressed gas during the compression phase of reciprocating compressors. The aim is to obtain a polytropic compression with a low mean exponent. This work approach is mainly experimental. This work is also part of a long-term project on a small plant for electric power generation using volumetric machines. The goal of the entire project is the realization of a small plant, of an electric power output from 1 to 3 kW, that must exploit low temperature thermal sources (up to 250 °C / 523 K). To compete with more affirmed technologies, it is necessary to limit the engines costs and maintenance costs. Small reciprocating machines usually require more maintenance than other machines, but they are relatively cheap and the maintenance itself does not require highly specialized manpower (at least not for ordinary maintenance). For this reason, such machines have been chosen for this project.

An analysis on thermodynamic cycles at low maximum temperature has been performed and it is reported in paragraph 1.5. This analysis shows that the compression and the expansion must have low polytropic exponents, in order to achieve any work output from low temperature thermal sources. This work analyses in details the compressor and proposes a method to achieve a compression as close as possible to an isothermal: the use of a gas-liquid Micro Channel Heat Exchanger (MCHE) inside the compression chamber.

So, this thesis starts with a theoretical analysis on reciprocating machine principles, focusing on non-adiabatic cases. The analysis includes some paragraphs on the reciprocating expanders (that are far less studied and known than the compressors) and on ideal cycles.

The subsequent chapter (Chapter 2) focuses on the exchanger study. The exchanger was made in aluminium using the DMLS additive manufacturing technique. The preliminary calculations, design and experimental activities on the exchanger are all part of this work and are illustrated in chapter 2.

Chapter 3 is about the experimental activities on the compressor. First, the compressor was characterised without modifications. Then the exchanger was added to the compressor and tested. The test bench was built up in the department laboratory and the software for the data acquisition is also part of this three years' work. More details on these matters are shown in appendixes.

Chapter 4 shows a one-dimensional calculation using Siemens Amesim software. The model has not been perfectly calibrated yet; however, it follows the experimental data well enough to support some speculations on the instantaneous heat transfer rate in the exchanger.

Chapter 5 is about future activities. A new solution to overcome the limits highlighted in chapter 3 and 4 is illustrated.

List of figures

List of tables

Nomenclature

A	Transfer area [m^2]	p	Pressure
$\dot{C}$	Heat capacity rate [W/K]	p_n	Nominal pressure
$\dot{C}_{max}$	Maximum of the two fluids capacity rate	P	Power [W]
$\dot{C}_{min}$	Minimum of the two fluids capacity rate	q	Specific heat [kJ/kg]
c	Specific heat capacity [kJ/kgK]	R	Specific gas constant for ideal gas
c_p	Isobaric specific heat capacity [kJ/kgK]	R_{air}	Specific gas constant for dry air
D_h	Hydraulic diameter [m]	R^2	Coefficient of determination
h	Specific enthalpy [kJ/kg]	Re	Reynolds number
h_c	Convective conductance [W/m^2K]	T	Temperature
k	Adiabatic exponent (1.4)	U	Overall thermal conductance [W/m^2K]
k_e	Elastic rate [N/m]	V	Volume
M	Mass	v	Specific volume
m	Generic polytropic exponent	V_d	Dead volume
m_{equ}	Equivalent polytropic exponent	V_0	Expander cubic size
m'_{equ}	Equivalent polytropic exponent (imperfect intercoolers)	W	Work [kJ]
NTU	Normal Thermal Unit (UA/C_{min})	w	Specific work [kJ/kg]
Nu	Nusselt number (hD_h/k)	w_{ind}	Indicated specific work
n	Number of stages	X	Length of the gas passages [m]
P	Power [W]	x	Displacement [m]
Pr	Prandtl number	$\ddot{x}$	Acceleration [m/s^2]

β	Compressor nominal pressure ratio	ε_f	Heat exchanger efficiency ($q_{(actual)}/q_{(maximum)}$)
β_i	Internal compression ratio	η	Machine efficiency
γ	Expander a-dimensional compression volume	η_{cycle}	Cycle efficiency
δ	Expander a-dimensional intake volume	η_{rig}	Regeneration efficiency
ε	Ratio V_d/V_0	λ_f	Fluid thermal conductivity

BDC	Bottom Dead Centre
FPGA	Field Programmable Gate Array
MCHE	Micro/Mini Channel Heat Exchanger
RT	Real Time
TDC	Top Dead Centre

Index

1 Introduction and theoretical considerations

This work's aim is to explore a new technique to achieve isothermal compressions (or, at least, to achieve compressions as near as possible to an isothermal). The solution analysed in this work consists in a miniaturized heat exchanger placed between the crankcase and the valve plate. In this way, the gas side volume of the exchanger is part of the compression chamber (Figure 1.1).

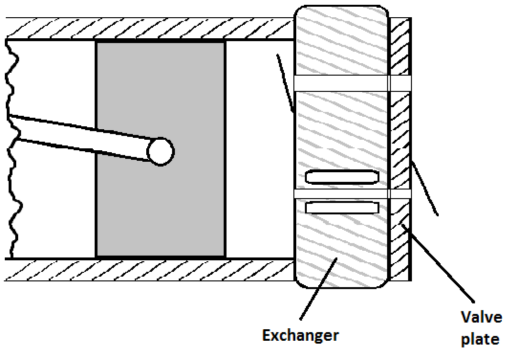

Figure 1.1 – Outline of a reciprocating compressor with internal MCHE

The advantages of an isothermal compression are well known, and this chapter does not focus on them. Instead, this chapter aim is to collect most of the volumetric machines principles that are used throughout next chapters. The volumetric machines are generally neglected, so that many minor details may be eluded. Paragraph 1.2 is about one of those details: how the polytropic curves are modified by the addition of dead volume (mass of gas), which is very important to bear in mind when comparing indicated diagrams of machines that differ from each other by the dead volume. Paragraph 1.3.2 is about volumetric rotary compressors (a scroll compressor has been used to test the exchanger as shown in chapter 2). Paragraphs 1.3.3, 1.4.3 and 1.4.4 are on the reciprocating expanders, that are far less studied and known than the compressors. Also, this chapter includes considerations about the multistage compressor, which is the only mature technology capable of achieving compressions with an average polytropic exponent less than 1.4. The last paragraph deals with thermodynamic cycles with low maximum temperature. The analysis clarifies what it is the maximum polytropic exponent allowable for such cycles and, thus, the goal of this thesis.

1.1 Literary survey

In the scientific literature, works on the performance of reciprocating machines follow two main approaches: the experimental one and the numerical one. Experimental studies are performed for various external conditions and for different type of compressors [1-4] or expanders [5]. The scientific community also developed many numerical models [6-13]. Among them, there are some that are particularly detailed: usually, their aim is to investigate on one (or few) of the various phenomena that occur during the reciprocating compressor working process (e.g. valves movements [6], noise effects [7], pressure waves and blow-by [3], etc). Other models are less detailed, and their purpose is the prediction of the global compressor performance to eventually use the model itself as part of a more complex model of an entire plant [12-13].

Nowadays, most of the effort is invested on studying new systems for reciprocating compressors failure prediction, leakages diagnosis and life estimation [14-18].

The study on cooled reciprocating compressions has never been popular, especially before the 2000. In 1980 S.W.Brok [19] diminished the practical advantages of cooled compressions, but in the conclusions of his work it was clarified that his findings were not conclusive. Throughout the successive decades, some works have studied different possibilities. As Heidari [20] stated, it is possible to classify those works into two groups:

1. The methods studied involve a liquid that is in contact with the compressed gas. Most of them study the liquid injection into the compression chamber [21-23]; other studies are on the so-called liquid piston [24]. Sometimes the two strategies are mixed [25-26]

2. The method studied does not involve liquids. One of the few studies in this group is Heidari's [27]. His strategy was to increase the heat exchanging surface inside the compression chamber.

The studies in the first group claim that compressions very close to isothermals are achieved. However, there are some drawbacks, as also stated by Heidari [27]: the liquid mixed to the gas through the spray must be separated afterward, so, the compressing system is complicated by additional equipment (the spray system itself and the separators). Moreover, in the case of liquid pistons, when gas high-pressures are involved, the gas can be solved in the liquid.

On the other hand, Heidari's system rely only on the compressor walls to exchange. Even though the surface is increased by several folds, in the long run the compressor walls will increase their temperature dulling the heat exchanging. On the other hand, that system was designed for CAES applications, so for a compressor intermittent usage. In fact, his study focuses on tests and calculations in unsteady conditions.

The solution proposed from this work is somewhere in the middle. It uses a liquid, but it keeps the liquid and the gas separated. It is based on Cozzolino's patent [28][1]

[1] Raffaele Cozzolino is a former professor of the Industrial Department at the University of Naples

1.2 Theorical considerations on the representation of thermodynamic transformations on pv and pV diagrams

The considerations expressed hereunder are simple facts that everyone knows and most easily forget. Someone said: “The devil is in the details”.

Figure 1.2 show a general transformation on the pv diagram. For the sake of simplicity, assume that it is an adiabatic transformation and its mathematical expression is shown in equation 1.1. Every point of the curve is thermodynamically determined, as both the pressure and the specific volume are state variables (i.e. the temperature is determined).

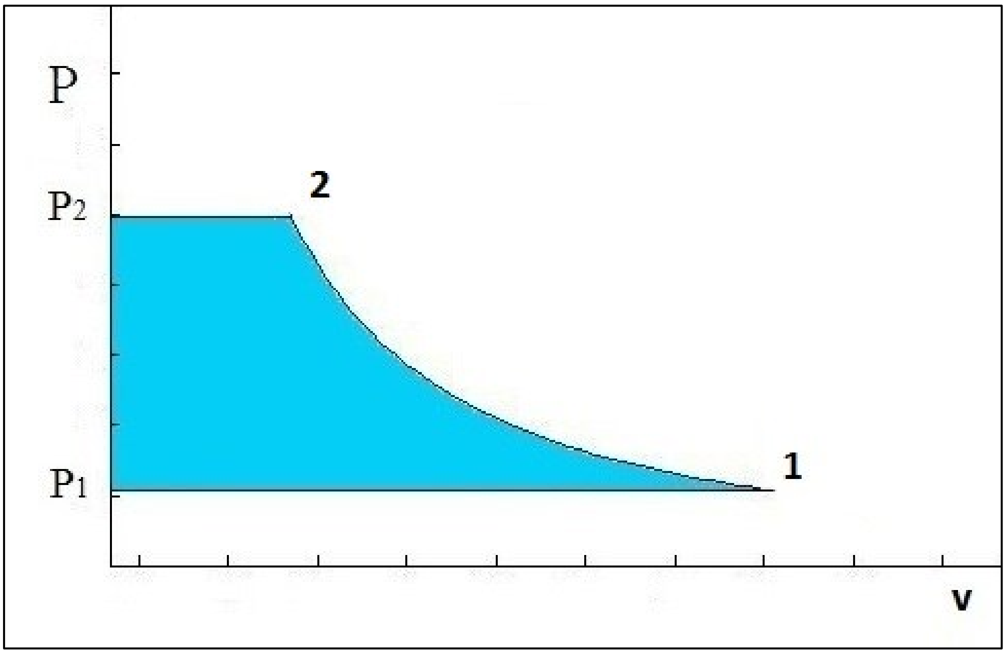

Figure 1.2 – Ideal compression on a pv plane

$$p^{\frac{1}{k}}v = p_1^{\frac{1}{k}}v_1 = p_2^{\frac{1}{k}}v_2 = constant \qquad [1.1]$$

It is possible to represent this transformation on the pV diagram, but the relationship is one to many (figure 1.2). Once the mass taken into consideration is fixed (M), the relationship between the representations is one to one.

$$M * p^{\frac{1}{k}}v = p^{\frac{1}{k}}V = M * constant = CONSTANT \qquad [1.2]$$

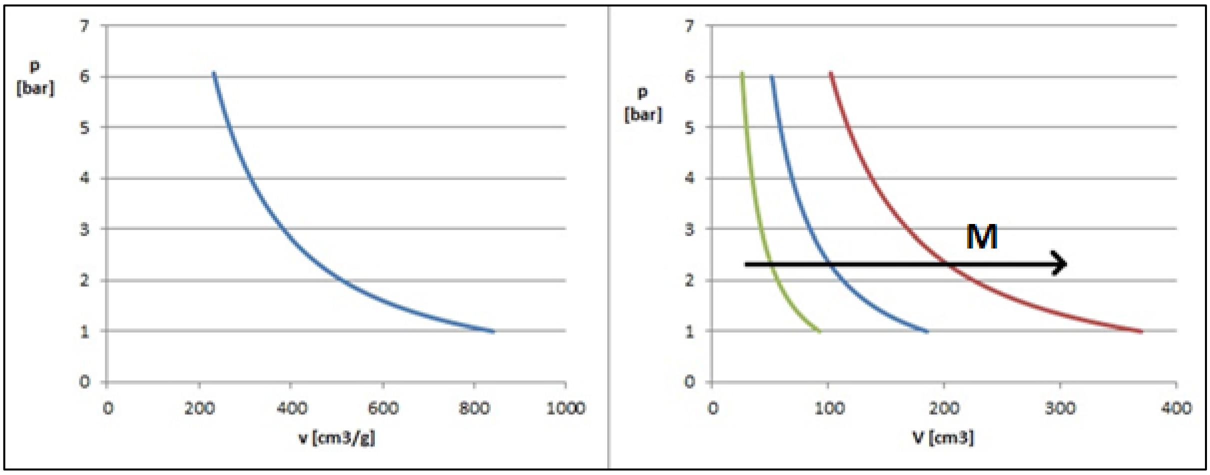

Figure 1.3 – An ideal compression on both pv and pV plane

The higher the mass, the further to the right the curve on the pV diagram will be (figure 1.3). These curves have different slopes, but they are all adiabatic curves. It is not possible to compare the slopes of transformations that refer to different masses, as in the case of reciprocating machines with different cubic capacity or different dead volume.

On the other hand, a pV curve can be represented with infinite curves on the pv diagram, unless the mass is fixed. In fact, without any further information, the mass of each point on pV diagrams is unknown as well as the temperature. If you know one of them you know the other via ideal gas law, but the temperature cannot be known by a pV diagram (otherwise the volume would be a state variable). This time, the higher the mass (the lower the temperature) the further on the left the curve will be (figure 1.4).

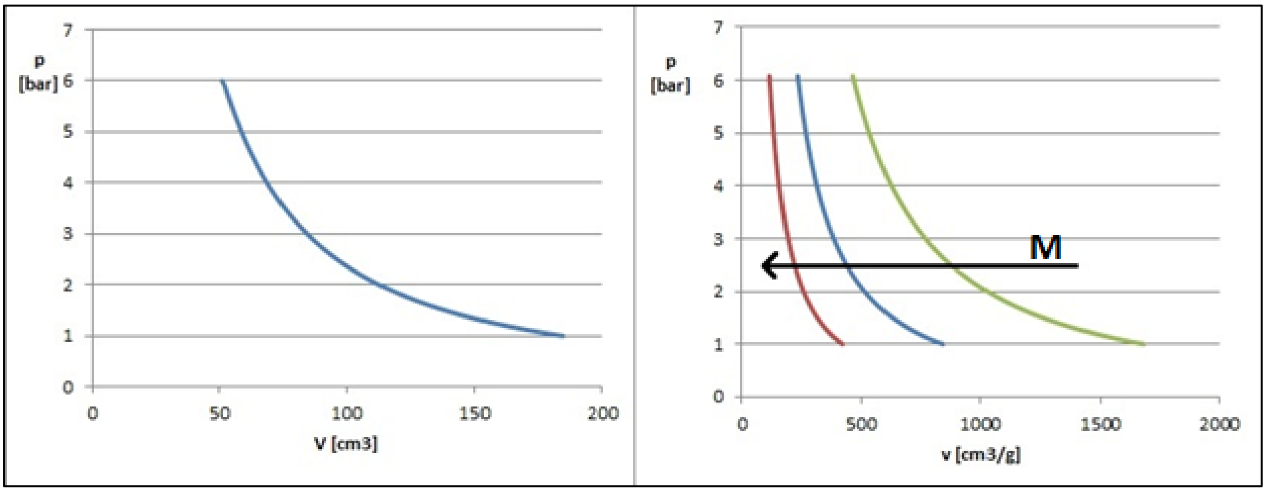

Figure 1.4 – Ideal compression on both pV and pv plane

Once the adiabatic intake and discharge hypothesis are removed, these considerations acquire importance. The transformation curves on pV diagrams (as well as the work related to that transformation) do not depend on the starting temperatures. On the other hand, their representation on pv diagram will change according to the temperatures, as well as the specific work related to the transformation.

If the polytropic exponent does not change, the pV curves of a reciprocating machine will not be influenced by a heat exchange on the mass variable phases. For example, if the polytropic exponent does not change, the volumetric efficiency (equation 1.3) does not change as well, even though in the dead volume there is a different air quantity according to the temperature (see figure 1.5).

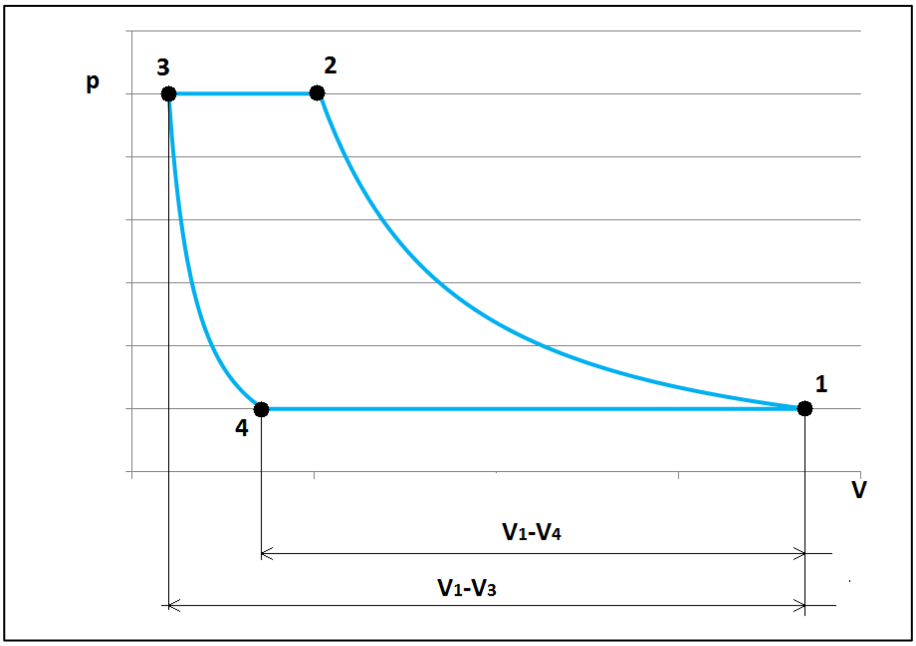

Figure 1.5 – PV diagram of an ideal reciprocating compressor with dead volume

$$\eta_V = \frac{V_1 - V_4}{V_1 - V_3} \quad volumetric\ efficiency \qquad [1.3]$$

Of course, in real cases the polytropic exponent could change as different temperatures lead to a different heat exchanged during the transformations. Nevertheless, it is important to remember that the pV compression curves changes are caused by the heat exchange during the transformation and not by the starting point temperature.

1.3 Volumetric machines

1.3.1 Reciprocating compressor: polytropic single stage versus inter stage refrigeration

A reciprocating compressor is a machine that uses a crankshaft to move a piston inside a (temporarily) closed cylinder. The volume variation causes the pressure raising. The discharge automatic valves allow the gas to exit the cylinder when compressed. The intake automatic valves allow the gas at low pressure to enter the cylinder before the compression phase. In real compressors, a portion of the cylinder volume cannot be swept by the piston, so the gas enclosed in this volume cannot exit. This volume is called dead volume and the gas trapped inside must expand before the intake valve can open. An ideal compressor diagram that consider the dead volume is shown in figure 1.6a. Thera are four phases: the compression phase (curve 1-2), the discharge phase (2-3), the expansion phase (3-4) and the intake phase (4-1). A real compressor diagram is shown in figure 1.6b.

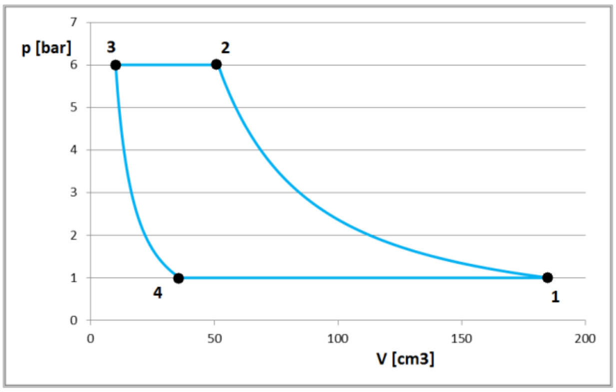

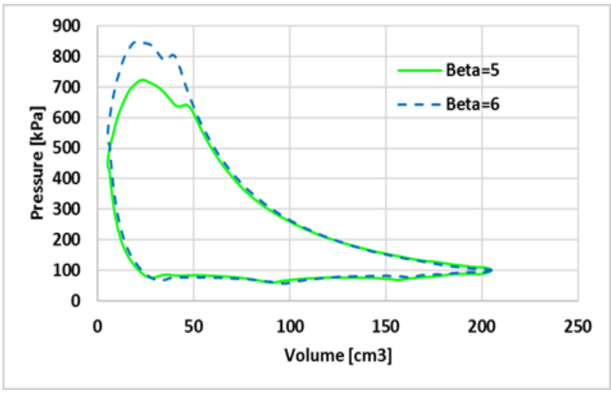

Figure 1.6a – pV diagram of an ideal reciprocating compressor with dead volume
Figure 1.6b – pV diagram of a real reciprocating compressor at two different compression

Reciprocating compressors are robust machines, so that their structures can bear high pressures. Moreover, their seals prevent most of the leakages. So, high pressures are easily tolerated, but there are strict limits to the pressure ratio: a too high-pressure ratio leads to too high temperatures that could damage the gasket or deteriorate the lubricating oil. High pressure ratios also lower the intake efficiency, as the mass trapped inside the dead volume is so high that, at suction pressure, it occupies too much suction volume. So, the most common way to achieve high pressure ratio is the multistage strategy, that is the usage of at least two compressors: the first compress the gas from the starting pressure to an intermediate pressure; then an intercooler cools down the gas to the intake temperature; the second compressor takes this cool compressed gas and compress it to an higher pressure. If needed more compressors in series can be used to achieve extremely high-pressure ratios.

So, an ideal multistage compression is made up by several adiabatic intercooled compression. If there are "n" number of compressors, the best efficiency is obtained if every compressor achieves the nth radix of the total compression ratio. The more the compressors, the more the compression is close to an ideal isothermal, leading to less theorical work consumption, as illustrated in figure 1.7, that shows the comparison between a single stage adiabatic ideal compression and a three stage intercooled ideal compression on the Ts diagram.

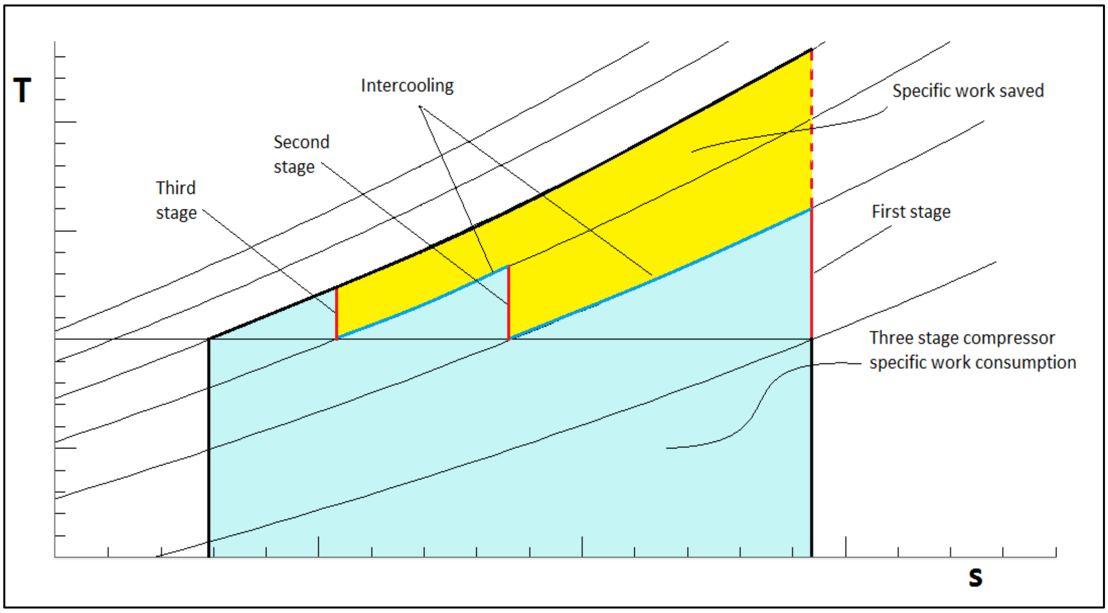

Figure 1.7 – Ideal multistage compressor with dead volumeon a Ts plane representation

However, the more the compressors, the higher the mechanical and pressure losses of real machines. So, the energy saving is not certain, as stated by Chlumsky [29] and shown in figure 1.8[2]: the overlap of the two diagrams is a work loss related to the pressure losses through the valves.

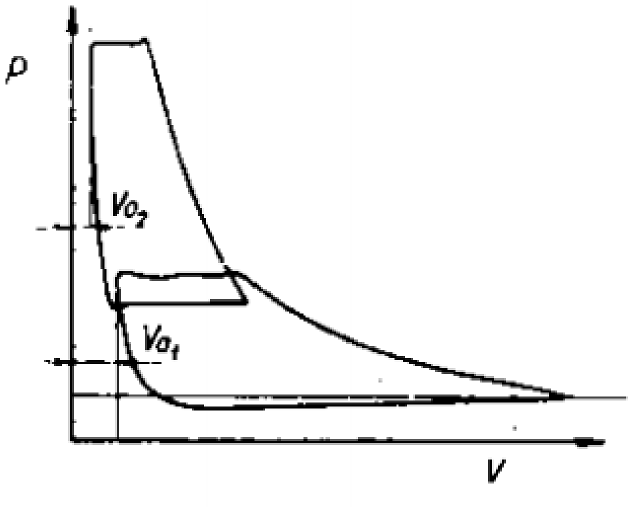

Figure 1.8 – Indicated diagram of a two-stage compressor

[2] Vladimir Chlumsky, op.cit. [29], pag. 77

Whenever every n number of compressors in series achieve the nth radix of the total compression ratio, an ideal multistage compression has the same work consumption of an ideal polytropic compression between the same extreme points. In this case, the polytropic exponent of this equivalent compression only depends from the number of stages (see equation 1.4 and figure 1.9). This means that polytropic compressions can achieve a lower ideal work consumption than the correspondent multistage ideal compressor, if they have lower exponent than the one calculated in equation 1.4.

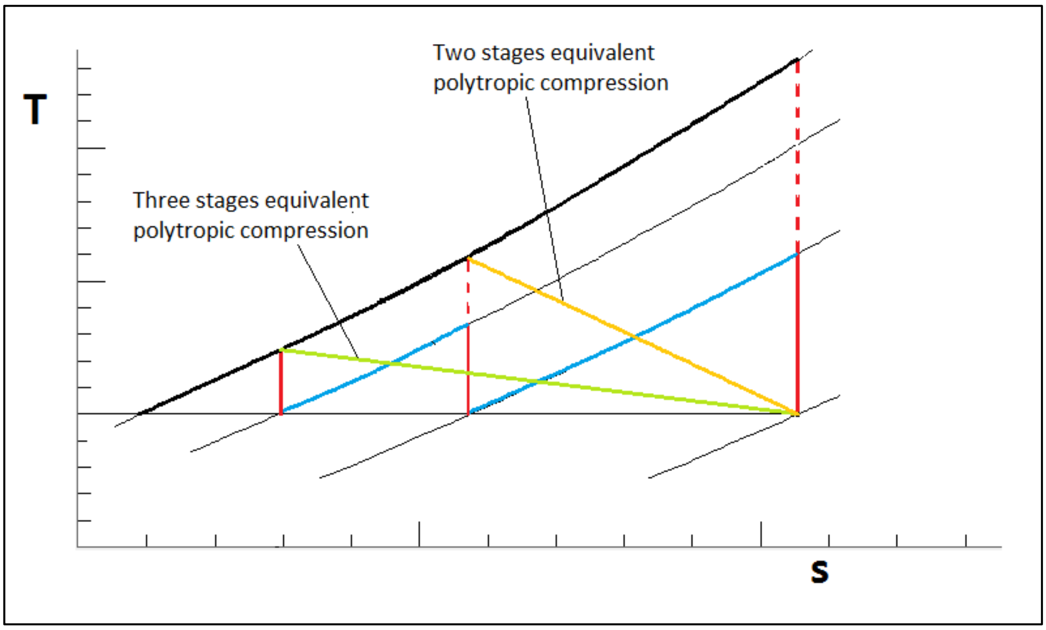

Figure 1.9 – Comparison between multistage and polytropic ideal compressions on a Ts plane

$$m_{equ} = \frac{nk}{(n-1)k+1} \qquad [1.4]$$

Where n is the number of stages and k is the adiabatic exponent. The more are the stages, the lower is the equivalent m exponent (see table 1)

Table 1- Equivalent polytropic exponent for every stages number

Number of stages	m_{equ}
2	1,166667
3	1,105263
4	1,076923
5	1,060606

On the other hand, the intercoolers cannot have perfect efficiency. There is always a difference between the initial temperature and the suction temperature of the compressors successive to the first. In these more realistic cases, the polytropic exponent (m'_{equ}) calculated between the extreme points depends also on the initial temperature, on the intercooler efficiency and on the total compression ratio (see figure 1.10 and equation 1.5).

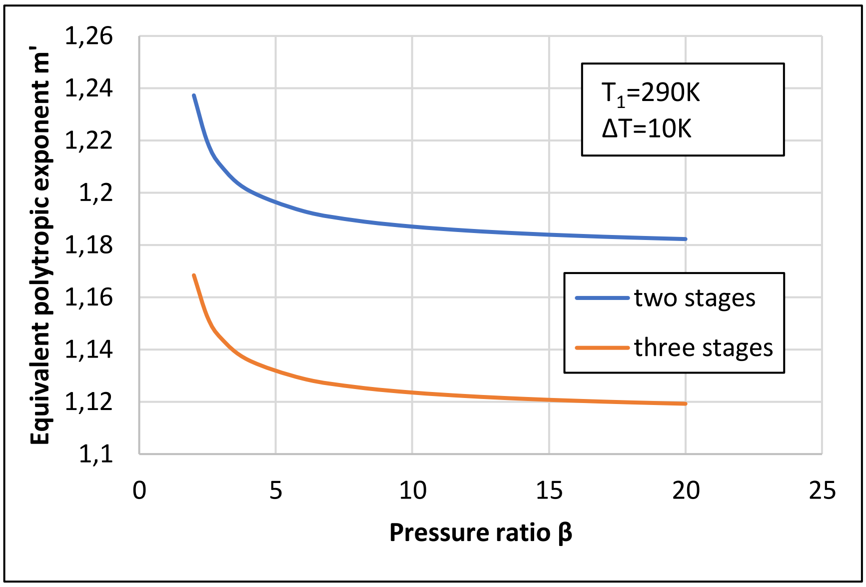

Figure 1.10 –Equivalent polytropic exponent in case of imperfect intercoolers

$$\frac{1}{m'_{equ}} = 1 - \frac{ln\left(\frac{T_{last}}{T_1}\right)}{ln(\beta)} \qquad [1.5]$$

Where T_{last} is the temperature of the last point of the multistage compression, ΔT is the difference between the inlet temperature T_1 and the starting temperature of each compression successive to the first, and β is the overall pressure ratio.

This polytropic compression work is slightly different from the intercooled one (figure 1.11): it is a little more in case of two stage compressors and a little less in case of more stages. Naming this difference $\Delta w_{multy-poly}$, equation 1.6 calculates it.

$$\Delta w_{multy-poly} = lowest\ multistage\ work - equivalent\ polytropic = \qquad [1.6]$$

$$= \frac{k}{k-1} R\left(\beta^{\frac{k-1}{nk}} - 1\right)[T_1 + (T_1 + \Delta T)(n-1)] - \frac{m'_{equ}}{m'_{equ} - 1} RT_1\left(\beta^{\frac{m'-1}{m'}} - 1\right)$$

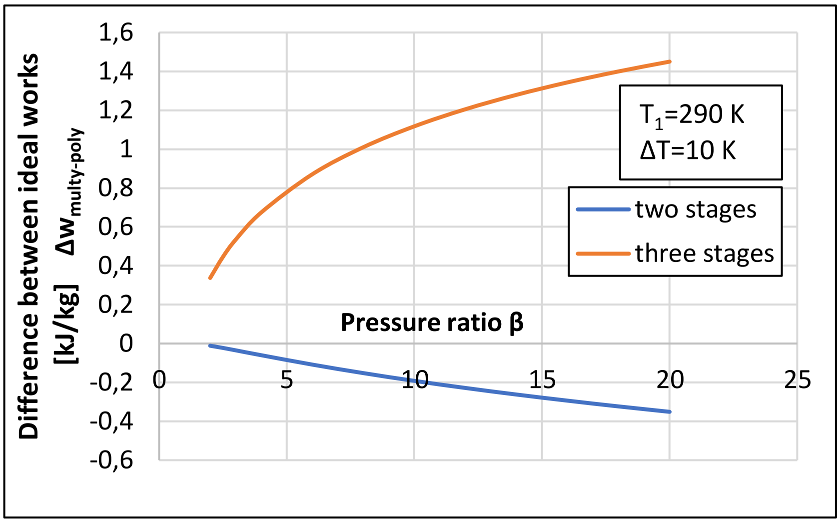

Figure 1.11 – Difference between ideal works in case of non-perfect intercoolers $\Delta w_{multy\text{-}poly}$

The difference $\Delta w_{multy-poly}$ is negligible. On the contrary, m'_{equ} is quite higher than m_{equ} In the hypothesis stated above (T_1=290K and ΔT=10K), every polytropic compression with an exponent lower than 1.17 has a lower ideal specific work consumption than an ideal two stage compressor, while the exponent must be lower than 1.11 to have a lower work consumption than an ideal three stage compressor (see figure 1.10).

So, a polytropic compression must have a quite a low polytropic exponent to be preferred to a multistage compression. However, it is not necessary to achieve an isothermal. Moreover, the present analysis is prudential as, in general, two or more machine in series should have more losses than a single machine.

1.3.2 Rotary compressors

All the different rotary machines are characterized by the same distribution system: the rotors discover the intake ports carved in the stator, and then bring the trapped gas towards the discharge ports, possibly compressing the gas reducing the volume. So, they all have a design pressure ratio β_i fixed by the internal volume reduction (for roots compressors β_i=1).

The compression ratio β, required by the application, may coincide or not with the compression ratio β_i, that the machine is able to build by itself due to volume change of the cells. Some authors [30] show the convenience to operate in the field β ≥ βi, because the compression efficiency decays more slowly than in the field below the nominal compression ratio. Figure 1.12 differs slightly from Stone's [30] elaboration, but the conclusion is the same.

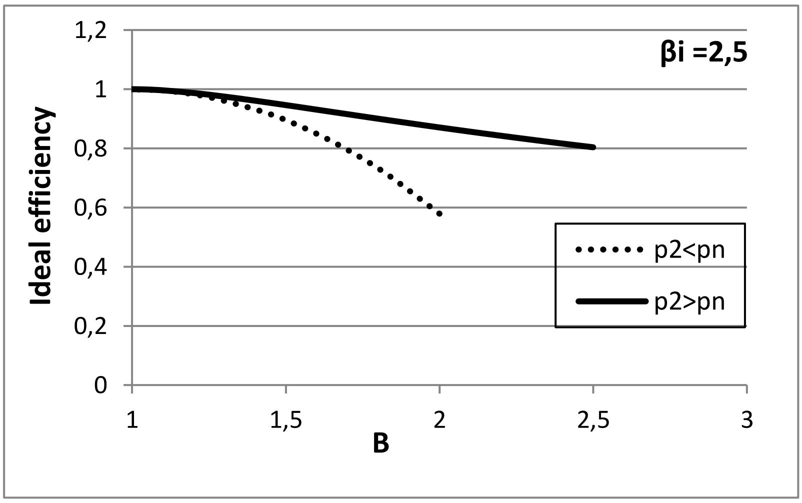

Figure 1.12 – Ideal efficiency of an ideal volumetric rotary compressor

Where B is

$$B = \begin{cases} \dfrac{\beta_i}{\beta} & (p_2 < p_n) \\ \dfrac{\beta}{\beta_i} & (p_2 > p_n) \end{cases} \qquad [1.7]$$

In equation 1.8a and 1.8b, the expression used to plot figure 1.12 are shown. The last compression (X-2) is neglected. These equations subscripts refer to figure 1.13. So, p_0 is the intake pressure and p_2 the delivery pressure; pressure p_1 is the pressure internally reached; β is the ratio between p_2 and p_0 and β_i is the ratio between p_1 and p_0; $W_{adiabatic\ 0\text{-}2}$ is the ideal work spent for a simple adiabatic compression from pressure p_0 to pressure p_2. All the transformations are considered adiabatic.[3]

$$(p_2 < p_1) \quad \eta_{ideal} = \frac{W_{0-2}}{W_{0-1}} = \frac{\dfrac{k}{k-1} p_0 V_c \left(\beta^{\frac{k-1}{k}} - 1\right)}{\dfrac{k}{k-1} p_0 V_c \left(\beta_i^{\frac{k-1}{k}} - 1\right)} \qquad [1.8a]$$

[3] Equations 1.7 and 1.8 refers to the "machines work", as every part of them are the result of the Vdp integral.

$$(p_2 > p_1)\ \ \eta_{ideal} = \frac{W_{adiabatic\ 0-2}}{W_{0-1} + W_{1-X}} = \frac{\frac{k}{k-1} p_0 V_c \left(\beta^{\frac{k-1}{k}} - 1 \right)}{\frac{k}{k-1} p_0 V_c \left(\beta_i^{\frac{k-1}{k}} - 1 \right) + [V_c'(p_X - p_1)]} \qquad [1.8b]$$

Therefore, the following discussion will refer only to the case $\beta > \beta_i$. In this case, there is a series of three compressions, as it is shown in figure 1.13. In these machines there is a first internal compression (0-1) due to volume reduction. Then, at the opening of the last internal contacts of the machine, two volumes are put into communication: the last cell with compressed gas at a pressure p_1 and the discharge volume V_{tank} of compressed gas at a pressure p_2. Then, an instantaneous mixing phase (1-X) at constant volume starts: the gas contained in the volume V_{tank}, which is located at the pressure p_2, flows back in the last cell (V'_c) and compresses it to an intermediate pressure p_X. Usually, the discharge volume is many times bigger than the last cell volume; so, the intermediate pressure is very close to the delivery pressure p_2. However, after the instantaneous compression, there is a third phase: the whole gas (contained in both the last cell and in the discharge volume) is compressed to the delivery pressure p_2. Often, the work spent in the third compression can be neglected. The volume V_{tank} must consider the dead volume (not swept by the rotor of the machine). In figure 1.13 the volume V_{tank} is not shown. It is recalled that in this type of machines the dead volume is not in communication with the suction. So, neglecting the losses for leakage, the whole volume V_c is filled by the fresh charge (figure 1.13).

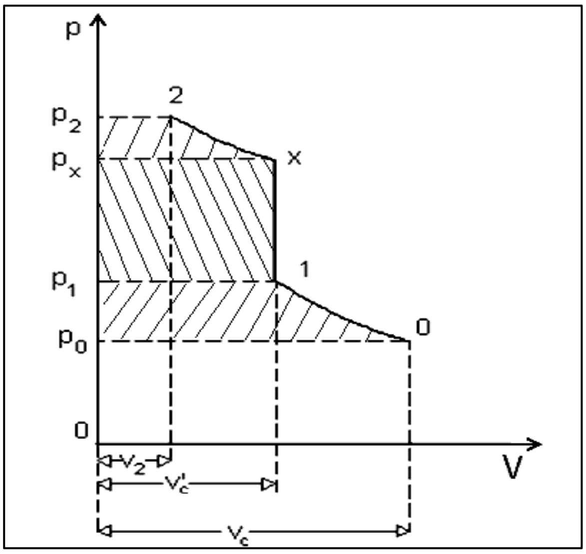

Figure 1.13 – Ideal pV diagram of an ideal volumetric rotary compressor

Every time the requested pressure ratio is not equal to the internal one, pressure waves are produced. If the discharge volume is many times bigger than the last cell volume and the delivery pressure is not far from the pressure internally reached, those waves can be neglected, as it will be shown in chapter 3.

1.3.3 The reciprocating expander: general overview and typical losses

The reciprocating expander is a positive displacement mechanical device that use the gas enthalpy to move its piston (more often more than one) obtaining mechanical energy. These machines were one of the most important of the industrial revolution as they were the core of the first trains and ferries. Their strong points are their simplicity, sturdiness and reliability. Also, their simple regulation across a wide operational field was one of the keys of their success. On the other hand, they cannot handle high gas flow rates, neither can bear high temperatures (especially due to the lubricating oil thermal limits), so their power density is limited. Moreover, their efficiency is generally low, especially in those operational condition near the maximum torque point. For these reasons, nowadays the reciprocating expanders are not widely used or, rather, they are mostly neglected. So, this paragraph contains some more details than the previous, hoping that these pages could be useful as brief summary on these machines.

This paragraph main source is George Brun [31]. The original book is written in French, and, as far as the candidate knows, it is not translated in any other language. The notation herein used is, as far as possible, the same of Brun's, in order to allow a simpler approach for those who, starting from this brief summary, needs to deepen their knowledge studying the original book. The figures are original, except when declared.

The main parts of a reciprocating expander are:

- A kinematic pair (piston – cylinder) that define the variable volume where the expansion take place.
- Two (or more) controlled valves that are needed for the right sequence of the phases.[4]

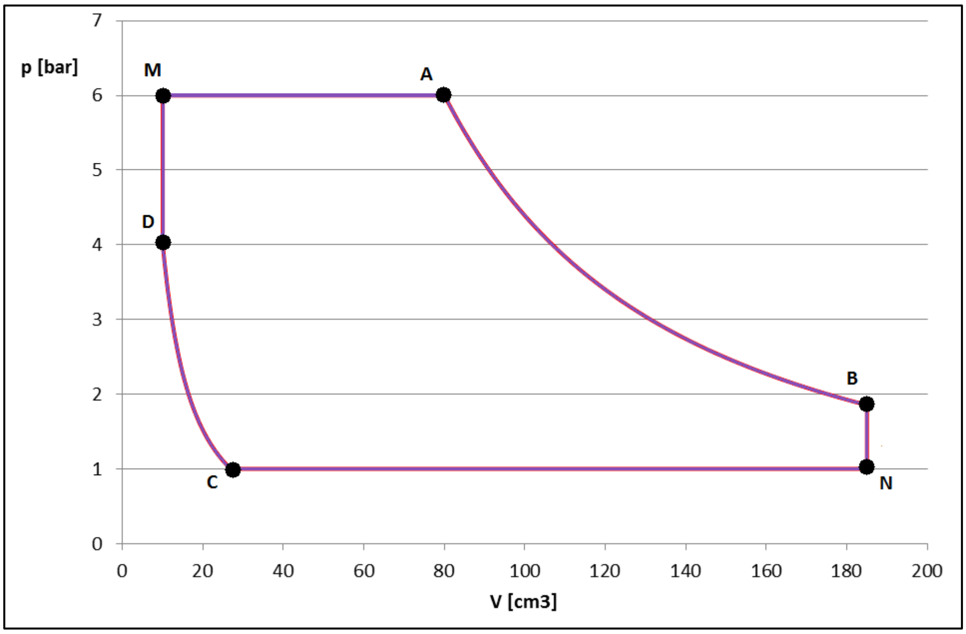

Figure 1.14 – Ideal pV diagram of an ideal volumetric reciprocating expander

[4] The valves must be controlled, because in the cylinder there is always a pression lower than the intake pressure and higher than the discharge pressure. In such a condition, the automatic valves would be always open

As for the reciprocating compressors, it is possible to divide the expander diagram into several phases. The compressor phases are four, while the expander phases are at least four and at most six. Refers to figure 1.14. Through the controlled intake valve, a certain gas quantity m_{intake} at high enthalpy goes into the cylinder (M-A) mixing itself with a smaller quantity m_{dead} of gas that was stored into the dead volume. Once the intake valve is closed, the gas starts the expanding phase (A-B), giving its energy to the piston. Once reached the bottom dead centre, the discharge valve is opened, and an instantaneous mixing (based on a pressure wave) takes place (B-N), unless the cylinder pressure is equal to the discharge pressure. Then the discharge phase begins (N-C). Before the top dead centre, the discharge valve is closed starting compression phase (C-D). This phase is not required, but it is highly recommended in order to increase the efficiency. Then, the intake valve is opened, and another instantaneous mixing takes place (D-M). This last phase is required if there is not compression, or if the compression is not enough to reach the inlet pressure. Otherwise, the second instantaneous mixing cannot take place, and the intake phase starts again (M-A). The most common case is a six phases diagram, with the B point pressure greater than the outlet pressure and the D point pressure smaller than the inlet pressure.

The description above refers to an ideal case, without valve losses and with infinite volume inlet and outlet tanks upstream the intake valve and downstream the discharge valve. In real cases, the upstream pressure (p_1) is greater than the intake mean pressure (p_{M-A}), while the downstream pressure (p_2) is smaller than the discharge mean pressure (p_{N-C}). In real cases, the transformations are not adiabatic, and the instantaneous mixings are not isochoric. The intake and discharge phases are not isobaric. In figure[5] 1.15 [31] a real expander indicated diagram is shown.

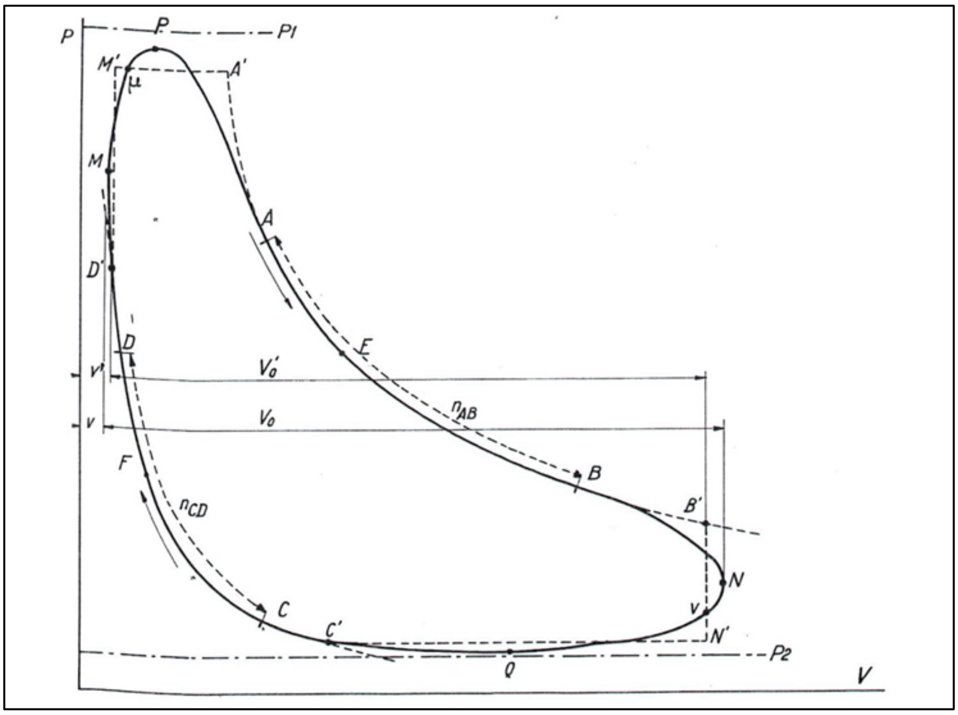

Figure 1.15 – Real pV diagram of a volumetric reciprocating expander

[5] Georges Brun, Thermodinamique des machines a fluide compressibile, Parigi, J.&R. Sennac, 1959, p. 108.

The real diagram is defined by the following parameters:

- The expander cubic size $V_0 = V_N - V_M$
- The ratio between the dead volume (V_d) and the cubic size $\varepsilon = \frac{V_d}{V_0}$
- The a-dimensional intake volume $\delta = \frac{V_A - V_D}{V_0}$
- The a-dimensional compression volume $\gamma = \frac{V_C - V_D}{V_0}$

The first two parameters are fixed for each expander. The third (δ) is set by the intake valve opening timing. It is possible to adjust the expander power varying δ: the higher the value of δ, the higher the gas flow rate for each round, thus the higher the power delivered. The fourth parameter (γ) is set by the discharge valve closing timing. The value of γ is a compromise between two losses: the work lost to compress the gas and the enthalpy lost by the intake gas (m_{intake}) mixing with the gas in the dead volume (m_{dead}). If m_{dead} has a too low pressure, the result of the instantaneous mixing is a rather low pressure (p_A) at the start of the expanding phase. On the other hand, the compression requires some work.

The expander losses can be classified into three groups[6] :

1. Compression loss
2. Intake losses
3. Expansion abrupt ending loss

The first type is already explained above: it is the work needed to compress the dead volume gas and thus limiting some of the intake losses.

The intake losses consist of three phenomena:

- The instantaneous mixing.
- The pressure drops across the valves.
- The gas cooling by the cylinder walls.

The first one is already described above, when explained the γ parameter. The pressure drops are the concentrated pressure losses given by the valves. The losses across the valves and the instantaneous mixing should increase the gas temperature, but cylinder walls are at a lower temperature: in general, the temperature at point A (T_A) is lower than the inlet tank temperature (T_1) and this lead to the third type of intake losses.
The gas cooling loss is decreasing with δ: the higher is the gas flow rate for each round, the lower is this loss because if the same walls must cool down a higher mass of gas, then the final temperature is higher.

[6] In this paragraph the difference between losses and energy degradation is not highlighted. Actually, the focus is on the phenomena that reduce the expander work output.

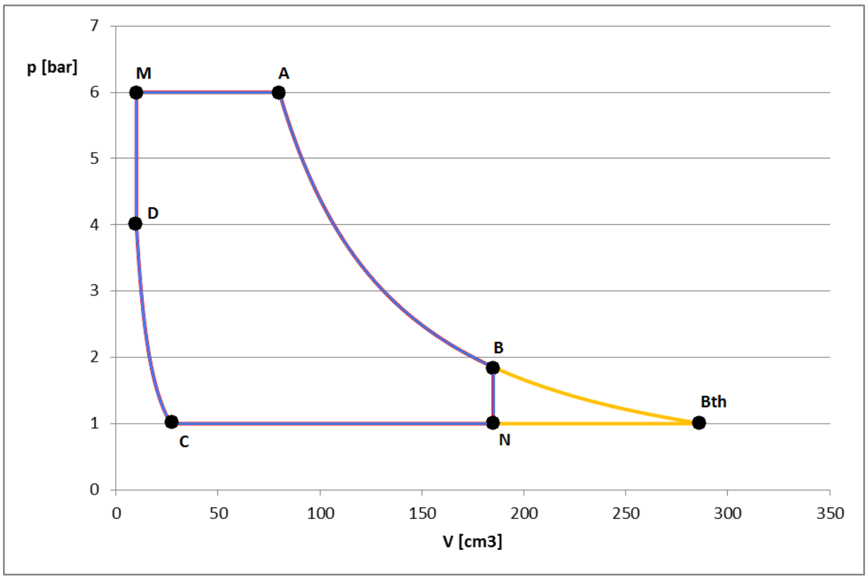

Figure 1.14 – Ideal pV diagram of an ideal volumetric reciprocating expander: expansion abrupt ending losses

The third type of losses are related to the instantaneous mixing that takes place at the discharge valve opening. In the most common case, the pressure at the end of the expansion phase (point B) is higher than the discharge pressure (figure 1.14). In this case, that pressure energy is lost. This loss is easily displayed on the pV diagram: extend the expansion curve from point B toward the discharge pressure. The point B_{th} is the last point of a theoretical complete expanding phase. The energy lost per round is the area B-Bth-N. Figure 1.15 shows that this loss is higher at high values of δ. However, low values of δ increase the cooling loss. On fixed point expander (i.e. expander for energy recover) the value of δ is the best compromise between these opposite tendencies. On regulated expander (such as on old ferries or trains) the value of δ depends on the request of power (e.g. the extra torque requested at the departure of the train). Figure 1.15 shows pV diagrams for the same expander at different values of δ and γ.

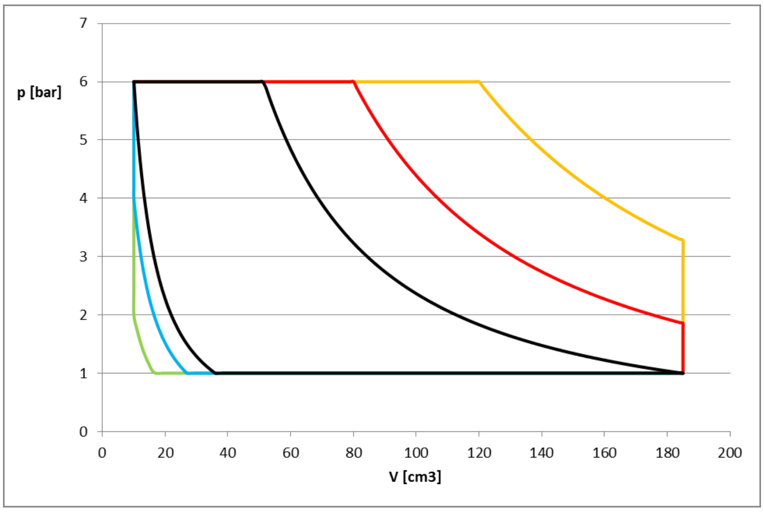

Figure 1.15 – pV diagrams for the same expander at different values of δ and γ

1.4 The polytropic transformations applied to reciprocating machines

1.4.1 Reciprocating compressor with internal cooling

In real cases all the compressor phases are characterized by heat exchange, especially the delivery phase due to the high speed and temperature of the gas [20]. In general, the thermodynamic state in point 1 is different from that in point 4, and the thermodynamic states of point 2 and 3 are different as well. Even if the two transformations (compression ad expansion) have the same polytropic exponent (and this is false in general), their representations on the pv diagram are not coincident (see paragraph 1.2). In figure 1.16 there is a pV representation of a generic ideal reciprocating compressor.

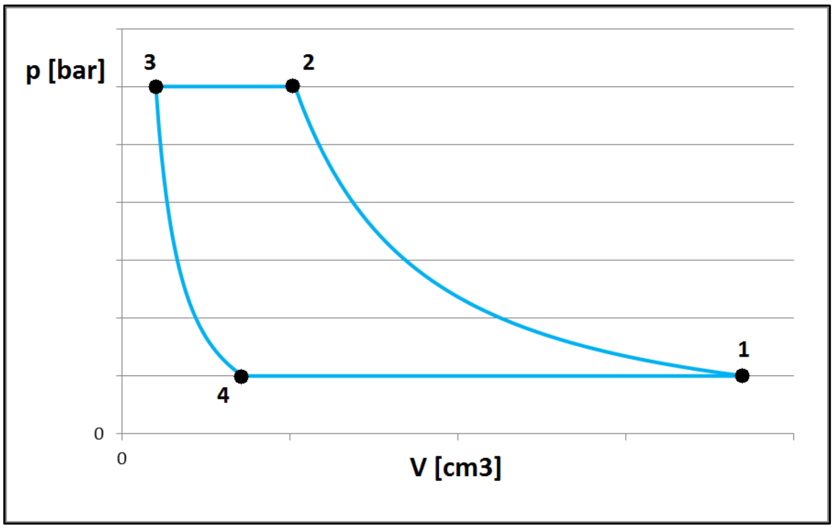

Figure 1.16 – PV diagram of an ideal reciprocating compressor with dead

Equation 1.9 and 1.10 are the mathematical representation of the two polytropic transformations, expressed as V=f(p). The first refers to the compression and the second to the expansion.

$$V' = \frac{CONSTANT'}{p^{\frac{1}{m'}}} \tag{1.9}$$

$$V'' = \frac{CONSTANT''}{p^{\frac{1}{m''}}} \tag{1.10}$$

The compressor indicated work (in this sub-paragraph the work will be assumed as positive when it is delivered to the gas) is calculated as in equation 1.11

$$W_{ind} = \int_{p_1}^{p_2} V' dp - \int_{p_1}^{p_2} V'' dp \qquad [1.11]$$

Due to the thermodynamic difference between the points of the two transformations, the two integrals of equation 1.12 are different.

$$W_{ind} = M_{comp} * \int_{p_1}^{p_2} v'\, dp - M_{exp} * \int_{p_1}^{p_2} v''\, dp \qquad [1.12]$$

In this equation, M_{comp} is the whole mass of gas compressed by the piston from point 1 to 2, while M_{exp} is the mass expanded from point 3 to 4. The specific volumes v' and v'' refers to the compression and the expansion respectively. In equation 1.13, M_{intake} is the difference between M_{comp} and M_{exp}, that is the mass of gas delivered by the compressor each revolution.

$$W_{ind} = M_{intake} * \int_{p_1}^{p_2} v'\, dp + M_{exp} * \left(\int_{p_1}^{p_2} v'\, dp - \int_{p_1}^{p_2} v''\, dp \right) \qquad [1.13]$$

Equation 1.13 shows the indicated work of an ideal compressor with dead volume as the sum of two works: the first is the indicated work of a compressor without dead volume that delivers a quantity of gas equal to M; the latter is the work paid for a reverse Bryton-Joule cycle with a mass of gas equal to M_{exp} as working fluid. It is a positive number, as points 1 and 2 have higher temperatures than points 3 and 4 respectively. The indicated specific work of the compressor is expressed in equation 1.14.

$$w_{ind} = \int_{p_1}^{p_2} v'\, dp + \frac{M_{exp}}{M_{intake}} \left(\int_{p_1}^{p_2} v'\, dp - \int_{p_1}^{p_2} v''\, dp \right) \qquad [1.14]$$

The first addend is the specific work of the thermodynamic transformation 1-2, and it is the algebraic sum of the enthalpic difference between the point 1 and 2 and the heat exchanged during the transformation (herein, Δq_{2-1} is the heat given to the gas). The second addend is named Δw, and it is a positive number (as the indicated compression work is considered positive).

$$w_{ind} = \Delta h_{2-1} - \Delta q_{2-1} + \Delta w \qquad [1.15]$$

So, it is not simple to use the Ts plane to fully describe these cases because of Δw. At least, it is not simple to represent everything in one Ts plane. The higher the temperature difference between points 2 and 3, the higher Δw. However, the ratio $\frac{\mathrm{M_{exp}}}{\mathrm{M}_{intake}}$ is low except in case of an extremely high-pressure ratio. On the other hand, if the transformations are close to an isothermal one, the thermal differences are negligible. The worst case is when the exchanger does not work during the transformations, but only during the discharge phase. In this last case the thermal differences would be the highest.

1.4.2 Considerations on real reciprocating compressors

Friction losses and pressure losses are real phenomena that may modify this analysis conclusions. The friction losses could be divided into two subcategories: piston friction losses and other friction losses. The difference is that part of the heat generated by the piston friction is delivered to the compressing gas, while the heat generated by the others is not, as it is generated too far from the gas.

So, both the heat generated by the losses and the thermodynamic increase of the gas temperature heat up the whole machine. For hermetic compressor, the electric losses contribute to heat up the entire system. Even the inlet collector may be hot, or at least hotter than the ambient. So, depending on the length of the collector and on the cooling system, the inlet gas could be hotter than expected, resulting in a lower density inlet gas and so in a lower mass compressed per revolution. Without other effects, this leads to a higher specific work consumption and overall higher temperatures. However, higher temperatures may cause higher heat released to the ambient, and possibly lower the mean polytropic exponent, countering the increase in the specific work consumption.

Pressure losses are mainly caused by the valves and modifies the indicated diagram increasing the indicated work. As the maximum pressure in the cylinder is higher than the ideal case, there is also more gas trapped into the dead volume, so the machine delivers a lower quantity of gas than expected. The temperatures are also higher, leading to similar considerations to those illustrated above.

The whole thesis is about the effects of an exchanger placed inside a machine cylinder. The exchanger causes an increase of the dead volume, further lowering the delivered mass of gas. Lower temperatures further increase the mass trapped into the dead volume. On the other hand, lower temperatures increase the inlet air density, increasing the mass delivered or, at least, countering the effects illustrated above.

The results of all these effects cannot be generalised. Each of these phenomena is strictly related to the actual real machine studied.

1.4.3 Internal heated expander

This sub-paragraph describes an ideal expander with a heated expansion caused by an internal heat exchanger (figure 1.17).

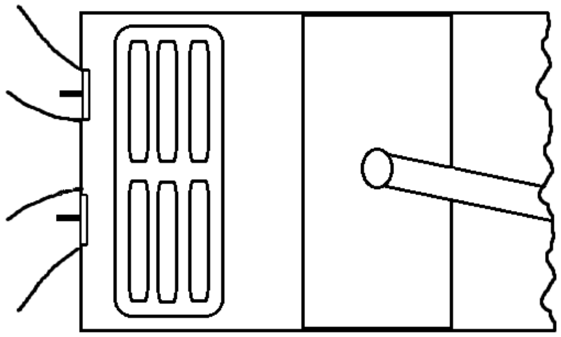

Figure 1.17 – Outline of a volumetric reciprocating expander with internal MCHE

The exchanger increases the dead volume, while the cubic size of the expander is the same. In the next figures the dead volume is not displayed, and the axis origin is the coincident with the top dead centre. In figure 1.18 two ideal machines are compared: an expander with a heat exchanger and another without it. Their regulation parameters (δ and γ, see sub-paragraph 1.3.3) are the same. Both their top dead centres are coincident with the axis origin. The points of the heated expander are highlighted with an "*" whenever they are not coincident with the points of the "standard" machine.

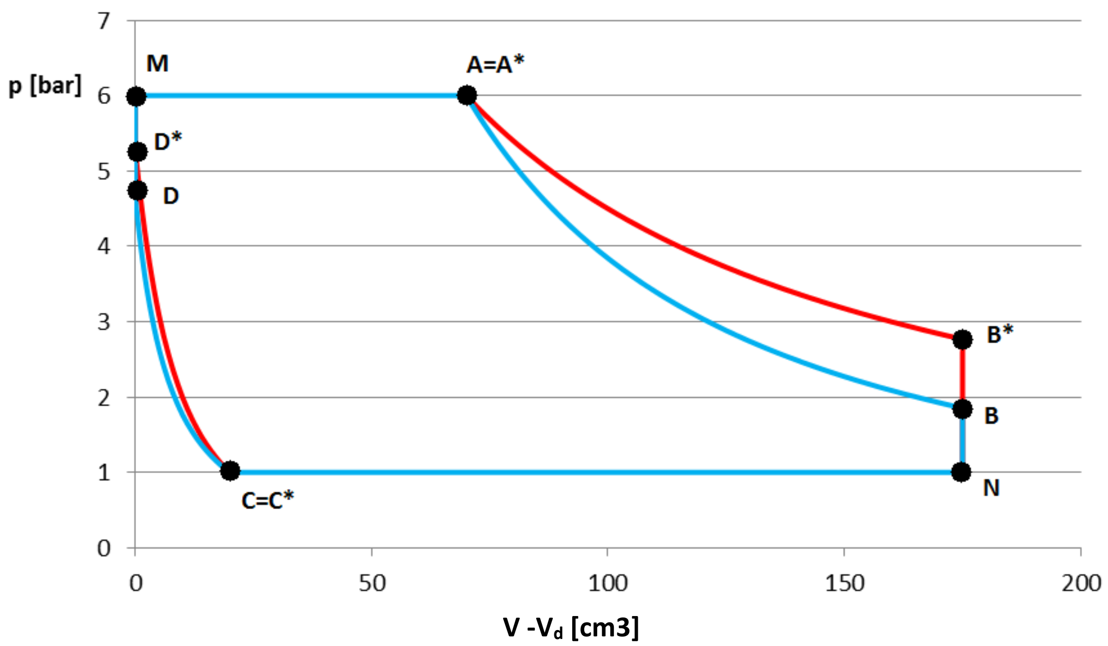

Figure 1.18 – pV diagram of an ideal reciprocating expander with dead volume
Blue curves: standard expander. Red curves: heated expander. Dead volume not displayed

The heated expander diagram area is increases due to the higher pressure of B*. The expansion curve has a lower slope because of both the higher dead volume and the lower polytropic exponent (see paragraph 1.2). The compression phase curve slope should be lower due to the highest dead volume, but the heating could rise it above the standard one. However, the curves are close to each other. The gas trapped into the dead volume should be more with a higher volume, but the heating lowers the gas density, so, in general, the tendency is uncertain. The exchanger greatly reduces the cooling losses that were decreasing with δ (see sub-paragraph 1.3.3). With no reason to reach high values of δ, it can be fixed to the value that lead to a complete expansion (figure 1.19). The indicated work is greatly reduced, but the mass flow rate is reduced as well: the efficiency is increased.

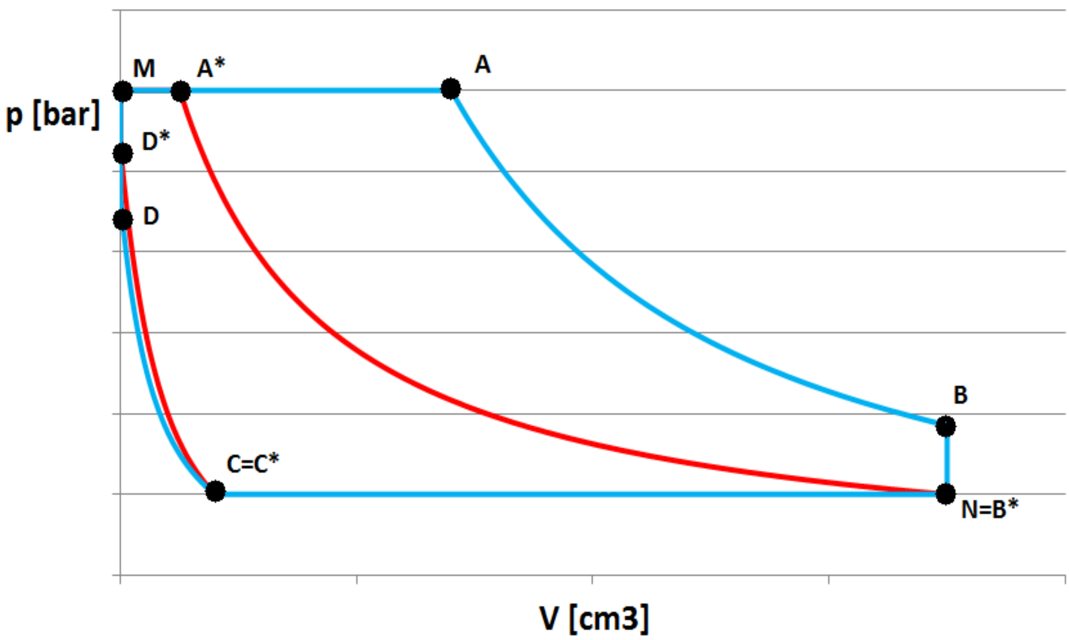

Figure 1.19 – pV diagram of an ideal reciprocating expander with dead volume
Red curves: heated expander with complete expansion. Dead volume not displayed

1.4.4 The heated expander: representation on a Ts plane

As the compressor, the expander cannot be easily represented on the Ts plane when the heat exchange is important. Figure 20 shows the pV diagram of an ideal expander without isochoric phases.

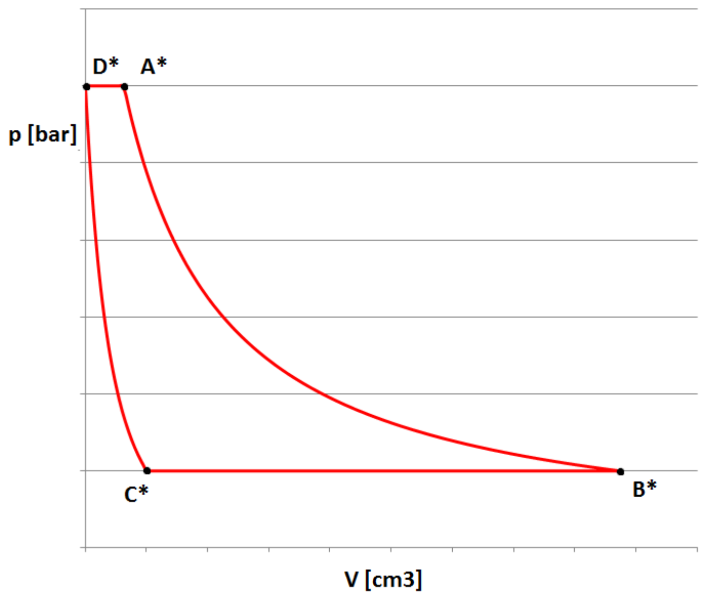

Figure 1.20 – pV diagram of an ideal reciprocating expander with dead volume (not displayed), complete expansion and complete compression

In these hypotheses the expander is similar to the compressor. So, the indicated specific work has a similar expression. Referring to figure 1.20 the expressions are shown in equation 1.16 and 1.17, where M_{intake} is the gas admitted into the machine per revolution and v' refers to the expansion and v'' to the compression phase.

$$w_{ind} = \int_{p_{B^*}}^{p_{A^*}} v'\, dp + \frac{M_{comp}}{M_{intake}} \left(\int_{p_{B^*}}^{p_{A^*}} v'\, dp - \int_{p_{B^*}}^{p_{A^*}} v''\, dp \right) \qquad [1.16]$$

$$w_{ind} = \Delta h_{B^*-A^*} + \Delta q_{2-1} + \Delta w \qquad [1.17]$$

In equation 1.14, Δq_{2-1} is the heat given to the gas, and Δw is the specific work (referred to the mass of gas used by the machine that is "M") obtained from the dead volume direct Bryton-Joule cycle. Δw is positive, and the higher the mass trapped into the dead volume and the thermal differences between points B^* and C, the higher Δw is. In this case, the exchanger increases the dead volume while decreasing the gas density and the thermal differences. So, Δw should not be significant, unless the discharge phase is affected by the exchanger, but the transformations are not. Moreover, if the isochoric phases are present, the extremes of integrations would not be the same for all the integrals and the equation would have more addends than in equation 1.16.

On the contrary, if the expander is adiabatic except for the transformations, there are no isochoric phases, and the two transformations have the same polytropic exponent, then the Ts plane is consistent and simple to use. Referring to figure 1.21, the green area is the specific work of an adiabatic expander. The sum of the yellow and red area is the specific heat given to a heated expander through the exchanger. The sum of the green and yellow area is the specific work of a heated expander. The red area is the energy wasted in the discharge gasses.

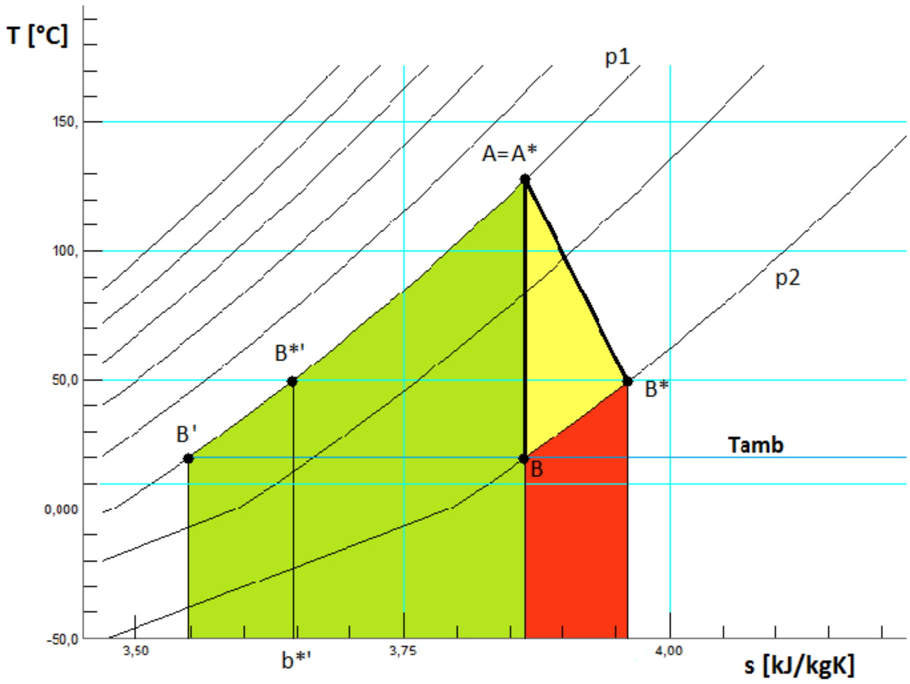

Figure 1.21 – Ts diagram of an ideal reciprocating expander with complete expansion and compression, adiabatic intake and discharge, expansion and compression with the same polytropic exponent

So,

- without isochoric phases
- when the two transformation phases have the same polytropic exponent
- and the other two phases are adiabatic

an ideal heated expander has a higher output work than a completely adiabatic one under the same conditions (same inlet pressure and same cubic capacity). However, this gain is given thanks to the heat supplied. The two cases (machines with and without heating) have different output but also different input.

On the other hand, a real heated expander is more complex than a traditional expander, due to the heating system. An economic analysis would be worthwhile, but it is beyond the scopes of this thesis. So, referring to figure 1.21, in table 2 are summed up the confrontations, on thermodynamic basis, between the two machines in these simplified hypotheses. The adiabatic, polytropic, first and second principle efficiencies are used. The equations shown below (1.18 and 1.19) clarify the terminology used.

Table 2 – Efficiencies definitions

	Traditional ideal	Heated ideal
Adiabatic efficiency	$\frac{Adiabatic\ work}{Adiabatic\ work} = 1$	$\frac{green\ + yellow\ areas}{green\ area} > 1$
Polytropic efficiency	$\frac{Adiabatic\ work}{Adiabatic\ work} = 1$	$\frac{green\ + yellow\ areas}{green\ + yellow\ areas} = 1$
I principle efficiency	$\frac{Actual\ work}{\Delta h_{A-B}} = 1$	$\frac{green\ area + yellow\ area}{green + yellow + red\ area} < 1$
II principle efficiency	$\frac{Actual\ work}{\Delta h_{A-B}} = 1$	$\frac{green\ area + yellow\ area}{green + yellow + red\ area - T_{amb}(s_{B^*} - s_{A^*})} < 1$

$$\eta_{adiabatic} = \frac{Actual\ work}{Adiabatic\ work} \quad ; \quad \eta_{polytropic} = \frac{Actual\ work}{Polytropic\ work} \qquad [1.18]$$

$$\eta_I = \frac{Actual\ work}{\Delta h_{A^*-B} + \Delta q_{A^*-B}} \quad ; \quad \eta_{II} = \frac{Actual\ work}{Exergetic\ inputs} \qquad [1.19]$$

It is quite difficult to determine a priori how to confront the two cases, as the heated machine transforms heat into mechanical energy more alike a plant than a machine. The heated expander gives more work with a lower efficiency (some heat must be wasted), but a lower efficiency is obvious whenever the heat is involved. Much depends on the purpose of the expander (being part of a plant or being used for heat recovery), on the actual conditions (e.g. type and number of types of hot fluids involved), and the actual performance of the real machines.

In the next paragraph, the application of polytropic transformation to thermodynamic cycles are shown. Starting from ideal cases, it is shown that the machines real performance overthrows the ideal considerations.

1.5 Thermodynamic cycles with polytropic transformations

1.5.1 Literary survey

There are three main families of thermodynamic small plants suitable to exploit renewable sources (solar, geothermal) or waste heat, each referring to a different ideal thermodynamic model: plants based on ORC cycles, plants based on Stirling's cycle, plants based on Ericsson's cycle.

The first type (ORC cycles) usually uses microturbines or rotary compressors (e.g. scroll) [1,12,13,15]. Their power output is from few kilowatts to 3 MW [32]. Many working fluids have been used in ORC cycles, such as R113, R123, isobutane, R134, propane, toluene, R600 and many others [33, 34]. Some of them have been banished for their harmful effects on the environmental or human health. Huge efforts are carried to explore new fluids to have better performances, less environmental and safety issues, and better compatibility with the materials and lower costs [33]. Of course, the plants must be in closed loop configuration as the working fluid cannot be air. ORC based plants are widely studied: according to Pereira et al. [35] over 600 projects are installed with a mean electric power of 5 MW. As for small plants, there are some systems at ready-to-market level of development, even though the costs are still high (from 1700 €/kWe to 4500 €/kWe) [35]. The plants are designed to fulfil both electric and thermal demand. According to Maghanki et al. [36] the electric efficiencies of the domestic ORC plants range from 10% to 20% while the thermal efficiencies range from 80% to 90% .

On the other hand, the Stirling and Ericsson based plants usually use reciprocating machines and can use air as working fluid.

Stirling based plants have profited from many research and efforts in the last 50 years [37,38]. Its applications power ranges from few kilowatts [39] to hundreds of kilowatts [40] and more [37]. Its main characteristic is the lack of valves, so that the compression and the expansion cylinders are not separated during the transformations. This leads to a real cycle very distant from the ideal one [41] and then to lower efficiency compared to the thermal level achieved. Moreover, pressure waves have a great influence on the Stirling engine performances, to the point that piston-less Stirling engines that exploits them are widely studied [42]. It is a closed loop configuration plant, so other fluids could be used instead of air [42]. Wang et al. [42] collected data from several previous studies on small existing Stirling engines of different types: classical (kinetic), thermoacoustic, free piston and liquid piston. Wang et al. findings are briefly summarized in the table below. One of the best among those with a domestic size is the kinetic Stirling engine studied by Gheith et al. [43] that combined a maximum power of 222W with a maximum efficiency of 10,3%.

Table 3- Stirling studies considered by Wang et al. [41]

Stirling typology	Number of studies considered	Power range [W]	Efficiency range
Kinetic	19	0,0003 to 740	0,1% to 15%
Thermoacoustic	9	0,049 to 1640 (acoustic power)	1,8% to 8% (before conversion to electric)
Free piston	8	0,02 to 19000	5,6% to 19,1%
Liquid piston	19	0,004 to 14	0,1% to 10,3%

Conversely Ericsson based plants are much more uncommon both in practical application and in scientific works. The main difference of the Ericsson's engines from the Stirling's ones are related to its valves, as the Ericsson's engine has two (or more) valves for every cylinder. So, the Ericsson engines may be more complicated, but, on the other end, the compressor and the expander are isolated during the thermodynamic transformations: this way the two machines main transformations are not influenced by each other. Moreover, the Ericsson's engine can operate in open cycle and low-pressure ratio, so it is suitable to operate in countries with low technological development [38]. The Ericsson's ideal cycle is made up by two isobaric and two isothermal transformation. The realization of an isothermal transformation is so difficult that some studies propose to position the exchangers before the machines' valves [38,44,45], even though it is not an appropriate solution to exchange any heat during the transformations [38]. Some others [46,47] consider isothermal transformations but not any heat regenerator, so that they valuate the isothermal transformations detrimental to the engine performances. All this studies on the Ericsson's engines [44,45,46,47] are numerical studies on ideal cycles with no friction losses and no valve losses. Their findings are collected in table 4.

Table 4 - Studies on the Ericsson's Engine

Authors	**IT**[7]	**Reg**[8]	**Max T [K]**[9]	**η**[10]	**Notes**
Touré et al. [43]	No	Yes	900 K	47%	Consider the machines dead volume and a regenerator efficiency (85%)
Ngangué et al. [44]	No	Yes	633 K	Max 35%	Consider the machines dead volume, a regenerator efficiency (85%) and friction losses. No pressure losses considered.
Creyx et al. [45]	Yes	No	923 K	Max 37,6%	Do not consider frictional, valve and pressure losses.
Hachem et al. [46]	No	No	1000 K	28,6 %	Ideal case

The analysis shown in paragraph 1.5.2 consider an ideal Ericsson engine, with regenerator, but without frictional, valve and pressure losses. However, the machines global efficiencies are considered as a whole. The machines are supposed to obtain ideal polytropic transformations at whatever polytropic exponent (so, even isothermal transformations are considered). Finally, the regenerator efficiency is considered. Figure ?? shows the engine scheme adopted.

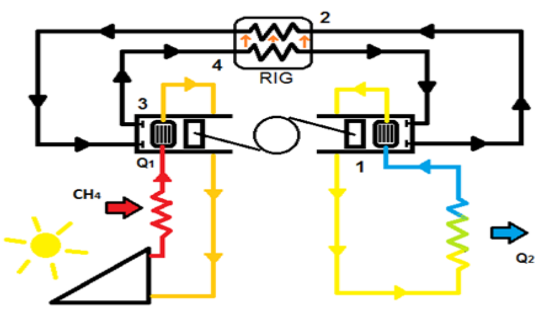

Figure 1.22 – Scheme of an Ericsson's engine

[7] They consider isothermal transformations
[8] They consider a regenerator
[9] Maximum temperature of the cycle
[10] First principle efficiency

1.5.2 Theoretical analysis on the Ericsson's cycle

The ideal cycle chosen as ideal model for this project plant is the Ericsson's cycle. The Ericson's cycle is made up by four transformations: two isobaric transformations and two isothermals. Refer to figure 1.22. If the heat discharged during the transformation 4-1 is used to heat up the fluid during the transformation 2-3, and the efficiency of this heat exchange process (regeneration) is 100%, then the efficiency of the cycle is equal to that of the Carnout cycle between the same isothermals.

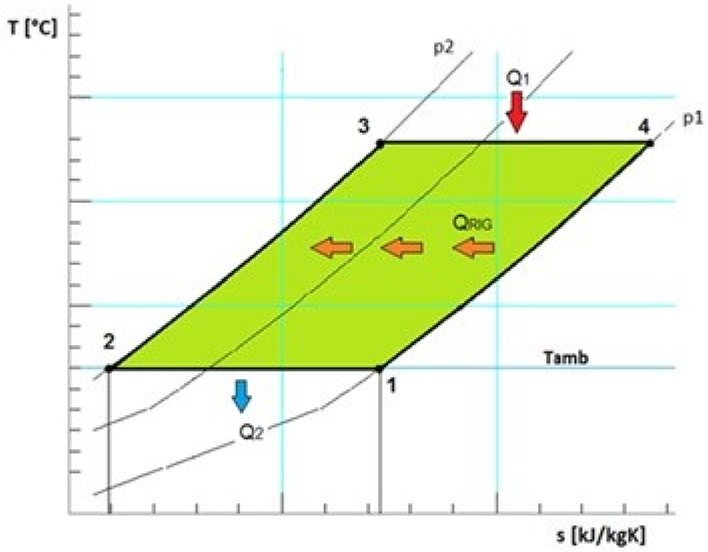

Figure 1.23 – Ts diagram of an ideal Ericson's cycle

The main issue of the Ericson's cycle is the isothermal transformations. Nowadays, it is not possible to produce a real prefect isothermal machine. First, the real transformation is not even a polytropic, but it is just near to a polytropic with an exponent greater than 1. Secondly, each machine has its losses. Moreover, the regeneration process has an efficiency lower than 100%, and the supposed isobaric transformations are not isobaric due to the pressure drops.

This analysis aim is to point out how much these issues affect the cycle efficiency. Step by step, every issue will be considered. Starting from an ideal cycle, the first considered issue is the actual polytropic exponent. In this hypothesis, the cycle efficiency expression is shown in equation 1.20. The exponent m_I and m_{III} refers to the compression and expansion respectively, and β is the ratio between p_2 and p_1. Every cycle maximum temperature is set at 523 K and the minimum temperature is set at 293 K.

$$\eta_{cycle} = \frac{w_{3-4} - w_{1-2}}{q_{2-3} + q_{3-4} - q_{reg}} \qquad [1.20]$$

Where

$$w_{1-2} = \frac{m_I}{m_I - 1} RT_1 \left(\beta^{\frac{m_I - 1}{m_I}} - 1\right) \qquad [1.21]$$

$$w_{3-4} = \frac{m_{III}}{m_{III}-1} R T_3 \left(\beta^{\frac{m_{III}-1}{m_{III}}} - 1\right) \quad [1.22]$$

$$a)\ q_{2-3} = c_p(T_3 - T_2);\ b)\ \ q_{3-4} = c_{III}(T_3 - T_4) \quad [1.23]$$

$$c_{III} = \frac{(m_{III} - k)\left(c_p - R\right)}{m_{III} - 1} \quad [1.24]$$

$$a)\ IF\ (T_4 < T_2) => q_{reg} = 0\ ;\quad b)\ \ IF\ (T_4 \geq T_2)\ => q_{reg} = c_p(T_4 - T_2) \quad [1.25]$$

This set of equations are consistent for every value of the polytropic exponent except for 1. The isothermal was computed using a polytropic coefficient of 1,001. According to equation 1.21, for a pressure ratio of 6, the cycle efficiency plot is shown in figure 1.23.

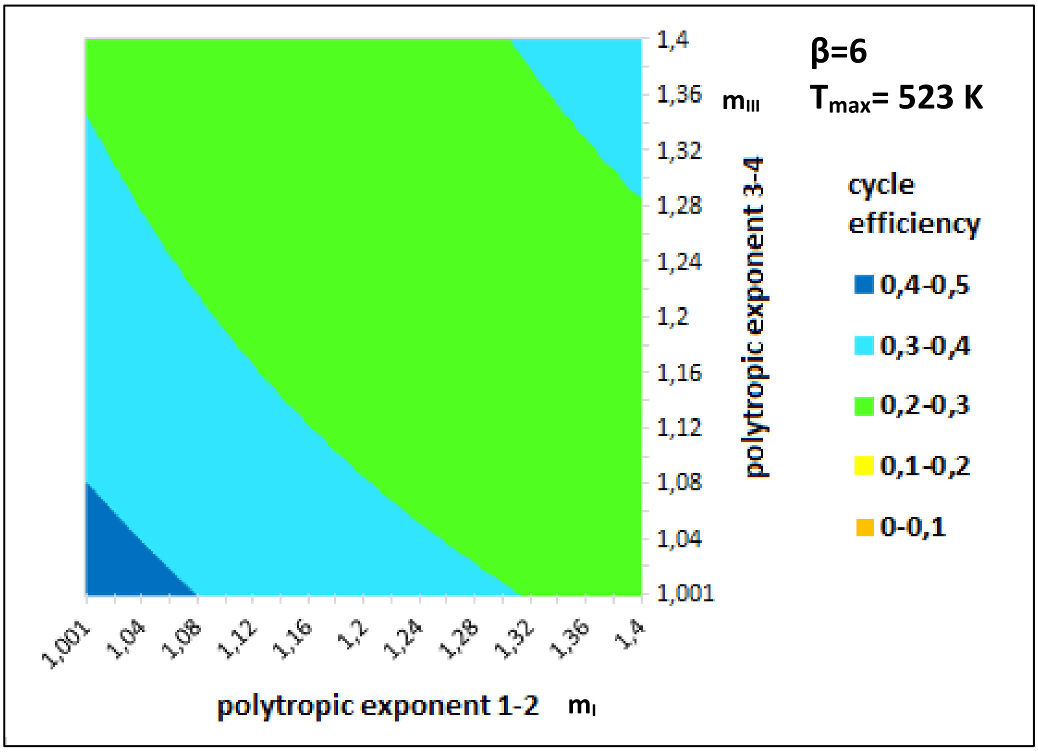

Figure 1.24 – Ericson's cycle efficiency replacing isothermals with polytropics for a pressure ratio of 6

There is an absolute maximum with compression and expansion both isothermal. However, the minimum is not the Joule cycle (both adiabatic), but somewhere in the middle. So, to improve an ideal Joule cycle, the compression and the expansion must be close to the isothermal. Figure 1.24 plots equation 1.21 when the two exponents to have the same value. For the β = 6 case, the minimum is for exponents values near to 1,2. For values smaller than the minimum point, the efficiency rises as the pressure ratio drops.

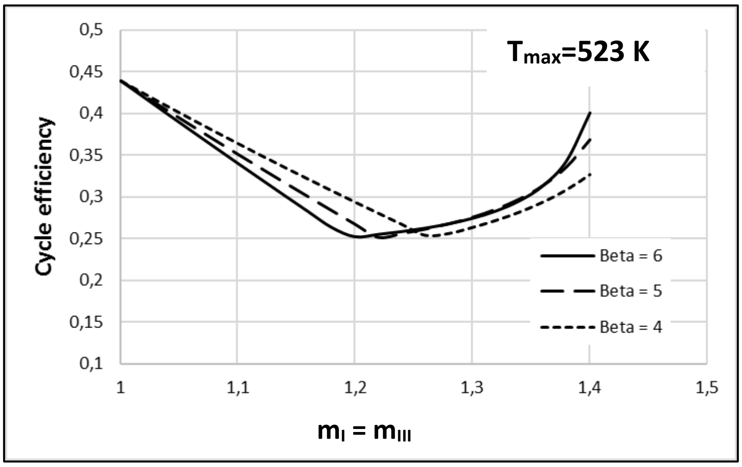

Figure 1.25 – Ericson's cycle efficiency replacing isothermals with polytropics for different pressure ratios

The next figures (figure 1.25 , 1.26 and 1.27) show the cycle efficiency when the machines have their efficiency smaller than 100%. The expression is shown in equation 1.26. For the sake of simplicity, the compressor efficiency is supposed to be the same as the expander one.

$$\eta_{cycle} = \frac{\eta w_{3-4} - \frac{w_{1-2}}{\eta}}{q_{2-3} + q_{3-4} - q_{reg}} \qquad [1.26]$$

Where the notation is the same as before and η is the machines efficiency measured towards the polytropic work.

$$\eta = \frac{real\ expander\ work}{w_{3-4}} = \frac{w_{1-2}}{real\ compressor\ work} \qquad [1.27]$$

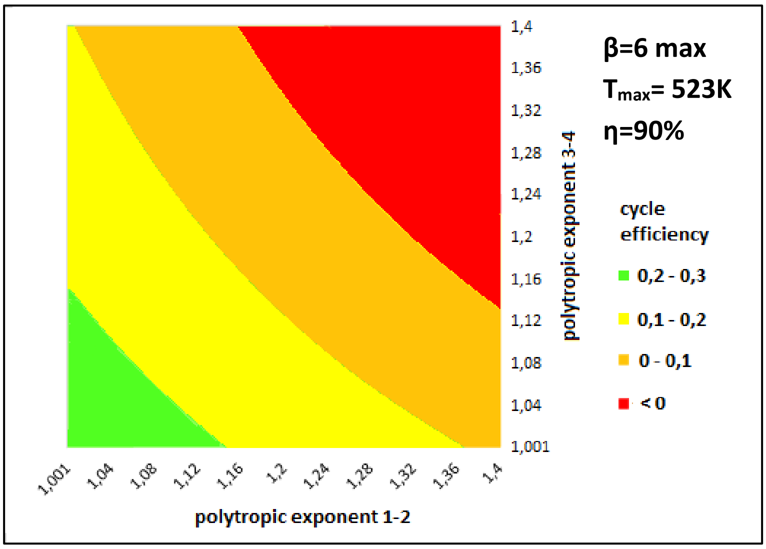

Figure 1.26 – Ericson's cycle efficiency with real machines for a pressure ratio of 6

In this case the function is monotonic. In every condition the efficiency is worse than in the “perfect” case (of course), so, with too high polytropic exponents, the cycle does not give work anymore (figures 1.25 and 1.26).

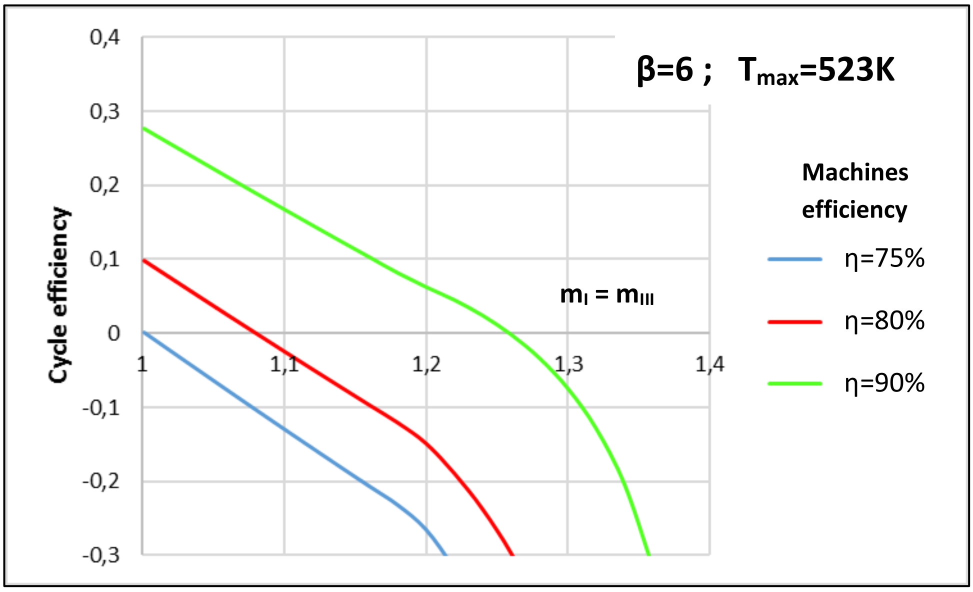

Figure 1.27 – Ericson’s cycle efficiency with real machines for different machines efficiency

Once again, the results are better for lower compression ratio (figure 1.27), but this time it is true for every polytropic exponent.

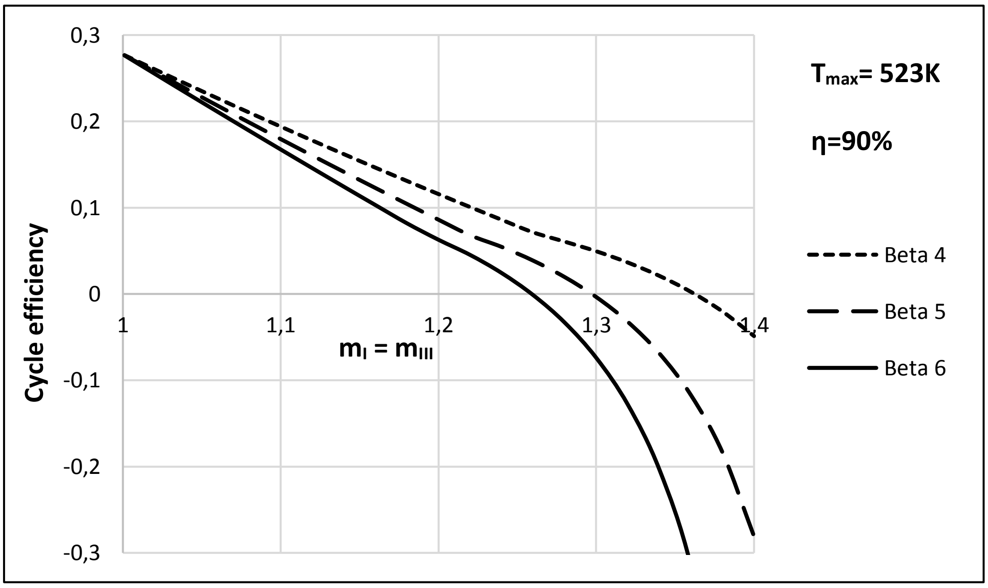

Figure 1.28 – Ericson’s cycle efficiency with real machines for different compression ratios

Lastly, the effect of the efficiency of the heat regeneration is considered. Figure 1.28 shows is similar to figure 1.27, except for the heat regeneration efficiency η_{reg}, that is set to 80%. The cycle efficiency expression is shown in equation 1.28. The notation is the same explained above (see equation 1.20).

$$\eta_{cycle} = \frac{\eta w_{3-4} - \frac{w_{1-2}}{\eta}}{q_{2-3} + q_{3-4} - \eta_{rig} q_{reg}} \qquad ; \qquad \eta_{reg} = \frac{q_{reg,real}}{q_{reg}} \qquad [1.28]$$

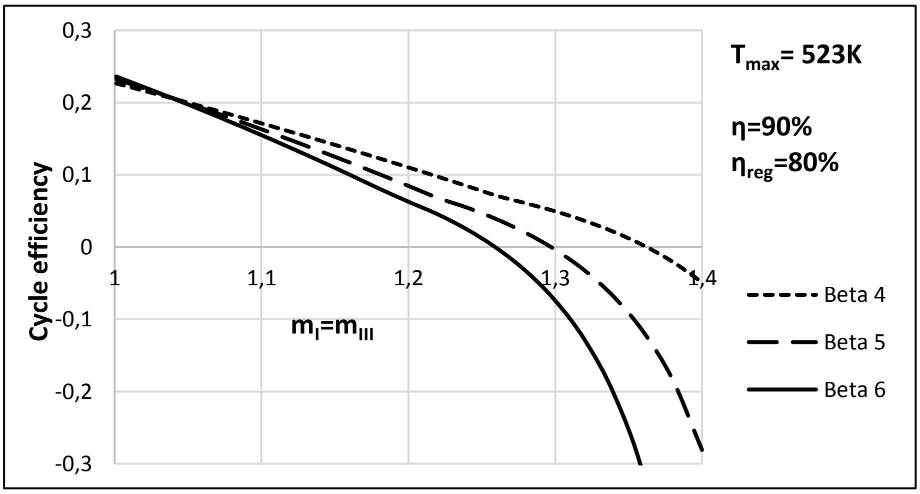

Figure 1.29 – Ericson's cycle efficiency with real machines and regenerator for different compression

The cycle efficiency lowers again, but the tendencies are similar. Except, for polytropic exponents close to 1, a higher compression ratio seems to be better. In figure 1.29 the regeneration efficiency is set to 50%. In case of very low regeneration efficiency, for polytropic transformations close to the isothermal, higher pressure ratios lead to higher efficiency. Usually, having a high regeneration efficiency is not a problem as the efficiency is related to the size of the exchanger, but, in some applications, the size or the weight of the exchanger must be limited.

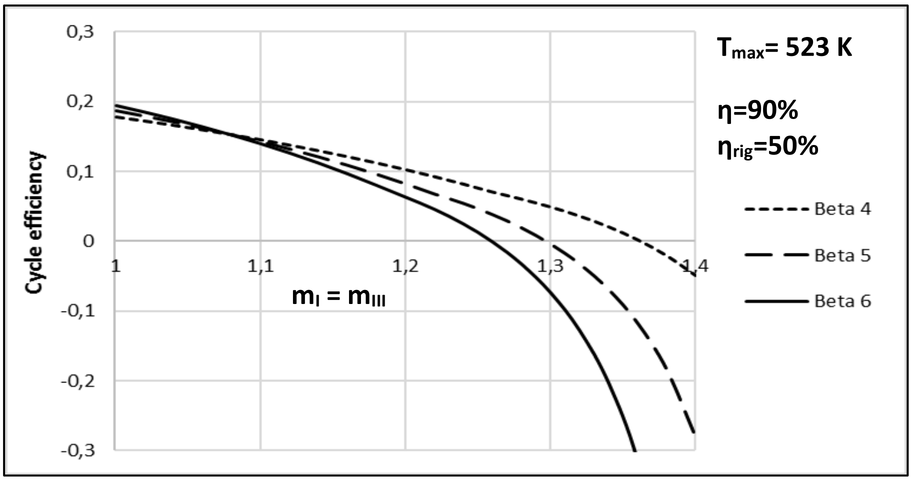

Figure 1.30 – Ericson's cycle efficiency with wasteful regenerator

The last two figures (figures 1.30 and 1.30) show the case with the machine and rigerenration efficeicncies equal to 90%. Figure 1.30 shows the work outpt, and figure 1.31 shows the efficiency. For transformations close to isothermals, the work output is increasing as the comression ratio increase. Moreover, for low values of the exponent, the difference in efficiency is negligible.

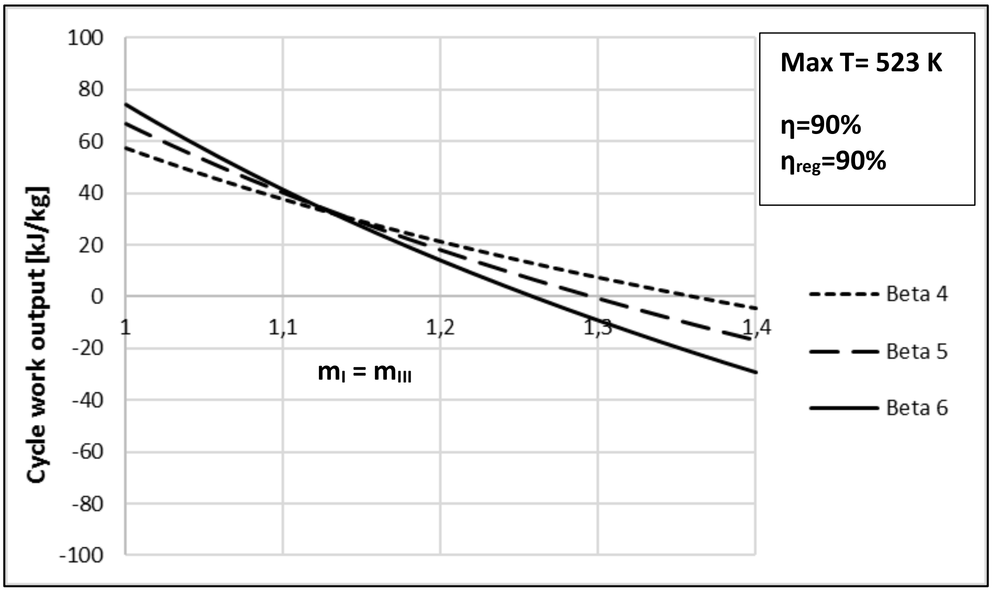

Figure 1.31 – Ericson's cycle work output with regenerator efficiency equal to 90%

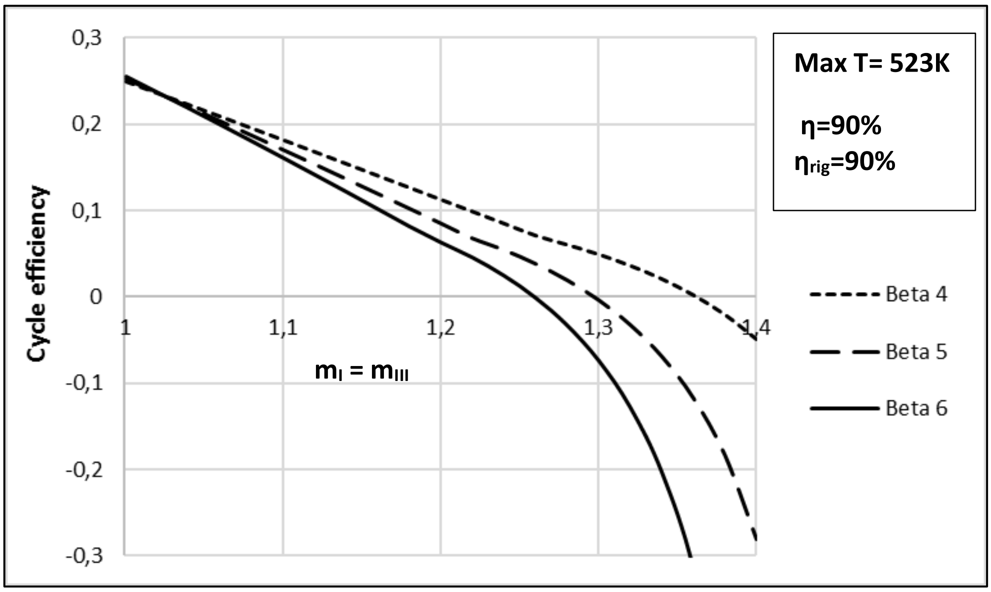

Figure 1.32 – Ericson's cycle efficiency with regenerator efficiency equal to 90%

This analysis shows that very low polytropic exponents are required to exploit low temperatures sources.

1.6 Bibliography

[1] Kang, Seok Hun. "Design and experimental study of ORC (organic Rankine cycle) and radial turbine using R245fa working fluid." Energy 41.1 (2012): 514-524.

[2] Blunier, B., et al. "A new analytical and dynamical model of a scroll compressor with experimental validation." International Journal of Refrigeration 32.5 (2009): 874-891.

[3] Gimelli, A., et al. "Reciprocating compressor 1D thermofluid dynamic simulation: problems and comparison with experimental data." International Journal of Rotating Machinery 2012 (2012).

[4] Elhaj, M., et al. "Numerical simulation and experimental study of a two-stage reciprocating compressor for condition monitoring." Mechanical Systems and Signal Processing 22.2 (2008): 374-389.

[5] Galindo, José, et al. "Modeling and experimental validation of a volumetric expander suitable for waste heat recovery from an automotive internal combustion engine using an organic rankine cycle with ethanol." Energies 9.4 (2016): 279.

[6] Nagy, Daniel, et al. "Valve lift measurement for the validation of a compressor simulation model." International Compressor Engineering Conference (2008).

[7] Stiaccini, Isacco, et al. "A reciprocating compressor hybrid model with acoustic FEM characterization." International Journal of Refrigeration 63 (2016): 171-183.

[8] Stouffs, Pascal, Mohand Tazerout, and Pierre Wauters. "Thermodynamic analysis of reciprocating compressors." International journal of thermal sciences 40.1 (2001): 52-66.

[9] Winandy, Eric, Claudio Saavedra, and Jean Lebrun. "Simplified modelling of an open-type reciprocating compressor." International journal of thermal sciences 41.2 (2002): 183-192.

[10] Longo, Giovanni A., and Andrea Gasparella. "Unsteady state analysis of the compression cycle of a hermetic reciprocating compressor." International journal of refrigeration 26.6 (2003): 681-689.

[11] Pereira, Evandro LL, Cesar J. Deschamps, and Fernando A. Ribas. "A comparative analysis of numerical simulation approaches for reciprocating Compressors." (2008).

[12] Dai, Yiping, Jiangfeng Wang, and Lin Gao. "Parametric optimization and comparative study of organic Rankine cycle (ORC) for low grade waste heat recovery." Energy Conversion and Management 50.3 (2009): 576-582.

[13] Gnutek, Z., and A. Bryszewska-Mazurek. "The thermodynamic analysis of multicycle ORC engine." Energy 26.12 (2001): 1075-1082.

[14] Loukopoulos, Panagiotis, et al. "Abrupt fault remaining useful life estimation using measurements from a reciprocating compressor valve failure." Mechanical Systems and Signal Processing 121 (2019): 359-372.

[15] Sharma, Vikas, and Anand Parey. "Performance evaluation of decomposition methods to diagnose leakage in a reciprocating compressor under limited speed variation." Mechanical Systems and Signal Processing 125 (2019): 275-287.

[16] Loukopoulos, Panagiotis, et al. "Reciprocating Compressor Valve Leakage Detection Under Varying Load Conditions." Asset Intelligence through Integration and Interoperability and Contemporary Vibration Engineering Technologies. Springer, Cham, 2019. 405-414.

[17] Xiao, Shungen, et al. "Nonlinear dynamic response of reciprocating compressor system with rub-impact fault caused by subsidence." Journal of Vibration and Control 25.11 (2019): 1737-1751.

[18] Tran, Van Tung, et al. "Single and combined fault diagnosis of reciprocating compressor valves using a hybrid deep belief network." Proceedings of the Institution of Mechanical Engineers, Part C: Journal of Mechanical Engineering Science 232.20 (2018): 3767-3780.

[19] Brok, S. W.; Touber, S.; and der Meer, J. S. Van, "Modeling of Cylinder Heat Transfer - Large Effort, Little Effect?" (1980). International Compressor Engineering Conference. Paper 305.

[20] Heidari, Mahbod; Lemofouet, Sylvain; and Rufer, Alfred, "On The Strategies Towards Isothermal Gas Compression And Expansion" (2014). International Compressor Engineering Conference. Paper 2285.

[21] Coney, M. W.; Stephenson, P.; Malmgren, A.; Linnemann, C.; Morgan, R. E.; Richards, R. A.; Huxley, R.; and Abdallah, H., " Development Of A Reciprocating Compressor Using Water Injection To Achieve Quasi-Isothermal Compression " (2002). International Compressor Engineering Conference. Paper 1508.

[22] Kremer, Rodrigo; Deschamps, Cesar J.; and Barbosa, Jader R., "Theoretical Analysis of the Effect of Oil Atomization in the Cylinder of a Reciprocating Ammonia Compressor" (2008). International Compressor Engineering Conference. Paper 1909.

[23] Guanwei, Jia, et al. "Micron-sized water spray-cooled quasi-isothermal compression for compressed air energy storage." Experimental Thermal and Fluid Science 96 (2018): 470-481

[24] Van de Ven, James D., and Perry Y. Li. "Liquid piston gas compression." Applied Energy 86.10 (2009): 2183-2191.

[25] Qin, Chao, and Eric Loth. "Liquid piston compression efficiency with droplet heat transfer." Applied Energy 114 (2014): 539-550.

[26] Acharya, Pinaki, Vikram C. Patil, and Paul Ro. "Experimental Investigation of Water Spray Cooling for Temperature Reduction in Liquid Piston Compressor." 24th International Compressor Engineering Conference at Purdue. 2018.

[27] Heidari, Mahbod, and Alfred Rufer. "Fluid Flow Analysis of a New Finned Piston Reciprocating Compressor Using Pneumatic Analogy." FDTT2014, Antalya, Turkey (2014).

[28] COZZOLINO, Raffaele. Surface heat exchanger for compressible fluid alternative volumetric machines. U.S. Patent Application No 13/584,202, 2013.

[29] Chlumski Vladimir, "Reciprocating and Rotary Compressors", E & F N Spon, London, 1966

[30] Stone C. "The efficiency of Roots compressors and compressors with fixed internal compression", Proceedings of the Institution of Mechanical Engineers, Part A: Power and Process Engineering (1988), 202(3), 199-205

[31] G.Brun, Thermodynamique des machine a fluide compressible, Paris, J.&R. Sennac, 1959

[32] Murugan, Sivalingam, and Bohumil Horák. "A review of micro combined heat and power systems for residential applications." Renewable and Sustainable Energy Reviews 64 (2016): 144-162.

[33] Rettig, A., Lagler, M., Lamare, T., Li, S., Mahadea, V., McCallion, S., & Chernushevich, J. (2011, September). "Application of organic Rankine cycles (ORC)". In World Engineers' Convention (pp. 1-10).

[34] Darvish, Kamyar, et al. "Selection of optimum working fluid for organic Rankine cycles by exergy and exergy-economic analyses." Sustainability 7.11 (2015): 15362-15383.

[35] Pereira, João S., et al. "ORC based micro-cogeneration systems for residential application–A state of the art review and current challenges." Renewable and Sustainable Energy Reviews 92 (2018): 728-743.

[36] Maghanki, Maryam Mohammadi, et al. "Micro combined heat and power (MCHP) technologies and applications." Renewable and Sustainable Energy Reviews 28 (2013): 510-524.

[37] Kongtragool, B., & Wongwises, S. (2003). "A review of solar-powered Stirling engines and low temperature differential Stirling engines". Renewable and Sustainable energy reviews, 7(2), 131-154.

[38] Fula, A., Stouffs, P., & Sierra, F. (2013, March). "In-cylinder heat transfer in an Ericsson engine prototype". In International Conference on Renewable Energies and Power Quality (ICREPQ'13) Bilbao (Spain), 20th to (No. 11, p. 6).

[39] Aksoy, F., Solmaz, H., Çinar, C., & Karabulut, H. (2017). "1.2 kW beta type Stirling engine with rhombic drive mechanism". International Journal of Energy Research.

[40] Kong, X. Q., Wang, R. Z., & Huang, X. H. (2004). Energy efficiency and economic feasibility of CCHP driven by stirling engine. Energy Conversion and Management, 45(9), 1433-1442.

[41] Naso, V. (1991). La macchina di Stirling. Editoriale ESA, Masson, Milano.

[42] Wang, Kai, et al. "Stirling cycle engines for recovering low and moderate temperature heat: A review." Renewable and Sustainable Energy Reviews 62 (2016): 89-108.

[43] Gheith, Ramla, Fethi Aloui, and Sassi Ben Nasrallah. "Determination of adequate regenerator for a Gamma-type Stirling engine." Applied Energy 139 (2015): 272-280.

[44] Touré, A., & Stouffs, P. (2014). Modeling of the Ericsson engine. Energy, 76, 445-452.

[45] Ngangué, Max Ndamé, and Pascal Stouffs. "Dynamic simulation of an original Joule cycle liquid pistons hot air Ericsson engine." Energy 190 (2020): 116293.

[46] Creyx, M., et al. "Energetic optimization of the performances of a hot air engine for micro-CHP systems working with a Joule or an Ericsson cycle." Energy 49 (2013): 229-239.

[47] Hachem, Houda, et al. "Comparison based on exergetic analyses of two hot air engines: A Gamma type Stirling engine and an open joule cycle Ericsson engine." Entropy 17.11 (2015): 7331-7348.

2 Activities on the exchanger

2.1 Literary survey

This chapter concerns the study of the heat exchanger used in the compressor prototype. As stated before, in this work, the way chosen to achieve a near isothermal compression is placing a miniaturized heat exchanger into the compressor cylinder. However, our first attempt to make an exchanger with additive manufacturing was one designed for another application: a bi-cylindrical expander. The two prototypes exchanging cores are similar, so the test on the expander exchanger gave reliable hints on the other exchanger characteristics. Part of the activities on the exchangers are collected in a paper already written by the candidate and his tutor and published in 2018 [48]. The overlapping parts are those that concerns an expander prototype.

This was our first attempt to obtain an exchanger through additive manufacturing. In past years, in this department, an exchanger made by glued aluminium layers was used. However, the glue had not enough strength to bear the pressure, so the experimental activities were limited to low compression ratio. The result was that the gains in terms of work consumption were negligible.

Literature on Micro and mini channel heat exchangers (MCHE) is wide, but most of the works are focused on heat sink for electronical devices [49-50]. Moreover, as stated by Arie et al. [51], there are few studies on metal exchangers made by additive manufacturing. However, those exchangers are valued in several fields [52], such as ORC cycles [53] and mobile applications [54], as they have high heat transfer coefficient, low volume, and low weight. The production of micro or mini exchangers involved many manufacturing techniques [55]. Actually, MCHE have been studied with significant effort since the 90s and even earlier [56-57] and metals are the best choice as regards heat conductivity, maximum temperature allowed and mechanical resistance; on the other hand, metals are more difficult and expensive to work with. So, at first, silicon wafers and plastic exchangers made up by additive manufacturing methods were used, despite the maximum temperature were limited by the materials.

2.2 First exchanger prototype

The first step was determining the narrowest duct and the narrowest wall that the printer can produce. Of course, the narrowest the duct walls, the more the ducts could be printed. A test campaign was performed. A series of sixteen (fig. 2.1) print tests were prepared to find out the printer limits and the best printer setting. They were all different for the width of the walls between fluids and the width of the fluid channels. At last the best combination was a width of 0.6 mm for both the walls and the channels.

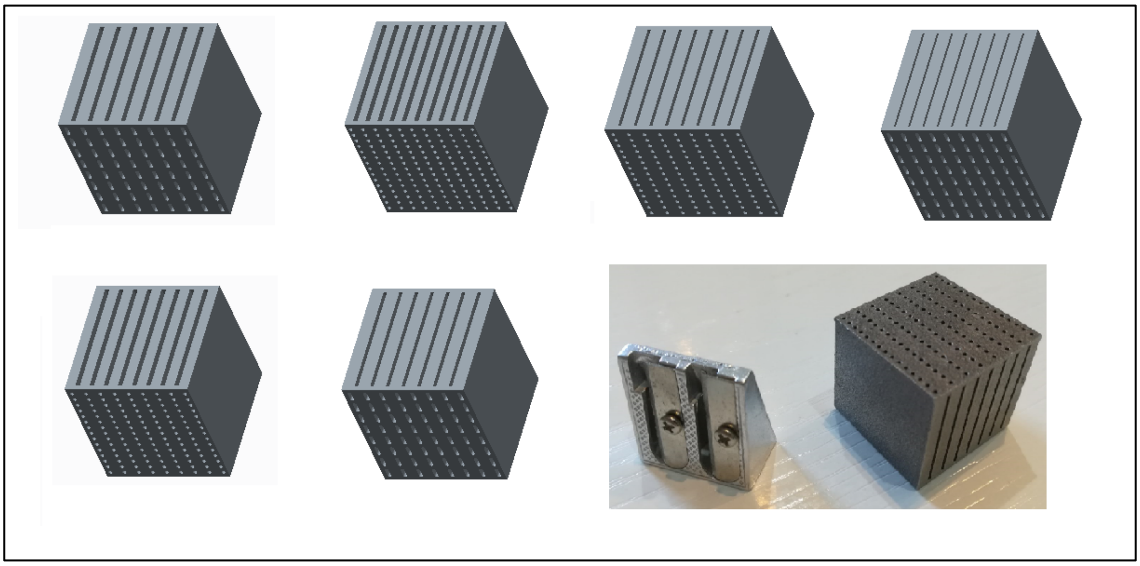

Figure 2.1 – Print test 3D sketch and photo of one of the tests

After this campaign, the first prototype was designed (figure 2.2) and then printed (figure 2.3).

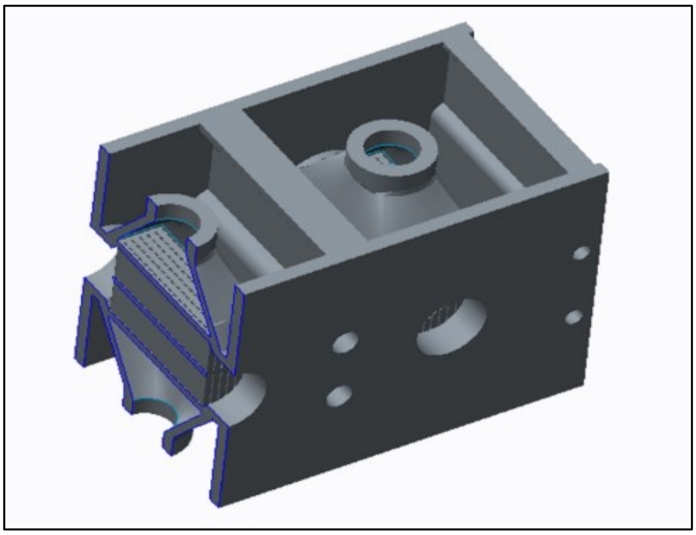

Figure 2.2 – First prototype 3D section

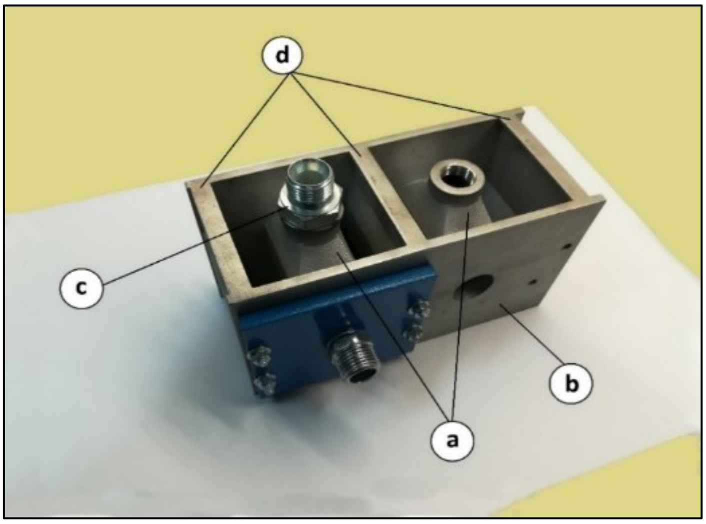

Figure 2.3 – First prototype photo

The investigated exchanger is designed to be installed on an expander prototype, that consist of two reciprocating machines of two cylinders each. Referring to figure 2.3, there are two independent cross flow exchanging cores (a), connected one to the other by the air side flanges (b). On the liquid side, there are threaded fasteners (c): the exchanger was built without thread, and then manually tapped. Three structural elements (d) are placed between the air side flanges, so that they could bear the contact forces on the flanges. The minimum exchanger length in the air flow direction, the maximum length in the water flow direction and the distance between the two cores are determined by the expander shape. Therefore, the air side channels are 51 mm long and has a narrow rectangular shape, 600 µm wide and 14 mm high. The liquid side channels are 35 mm long, 700 µm wide and 1.85 mm high. There are 22 air channels and 216 liquid channels for each exchanging element. The air side minimum section of the single element is about 1.8 cm^2 while the water side minimum section is about 2.8 cm^2. Not considering the collectors, the cores' volume is 62 cm^3 each (see also table 3).

Table 5- First exchanger prototype features

Air channel length	51 mm	Liquid channel length	35 mm
Air channel width	600 µm	Liquid channel width	700 µm
Air channel height	14 mm	Liquid channel height	1.85 mm
Air side minimum total section	1.8 cm^2	Liquid channel cross-section	1.295 mm^2
Air channels number	22	Liquid side minimum total section	2.8 cm^2
Air total exchanging surface	327.6 cm^2	Liquid channels number	216
Exchanger internal core air volume	9.4 cm^3	Liquid total exchanging surface	385.6 cm^2
Exchanger core total volume (air volume +liquid volume +aluminium volume)			62 cm^3

The exchanger design was performed considering the printer capabilities. Special attention was paid on the hanging surfaces. Hanging surfaces with a slope lower than 45 degrees can not be printed without additional supports. So, slopes higher than 45 degrees were designed wherever possible. Nevertheless, there were orizontal hanging surfaces, so extra supports were added and removed after the printing.

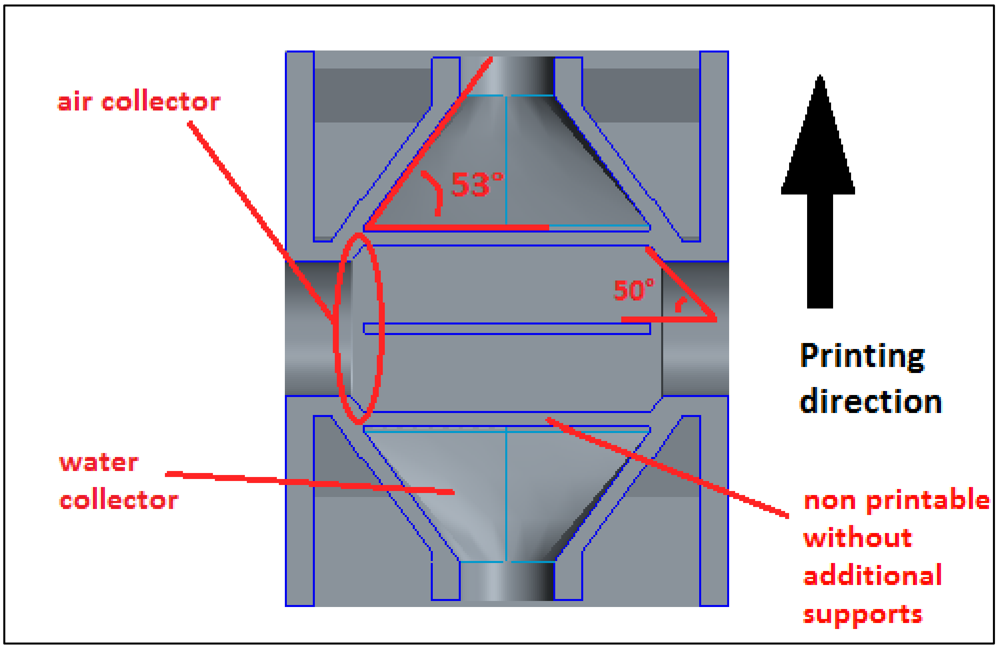

Figure 2.4 – First prototype section (plane of both fluids)

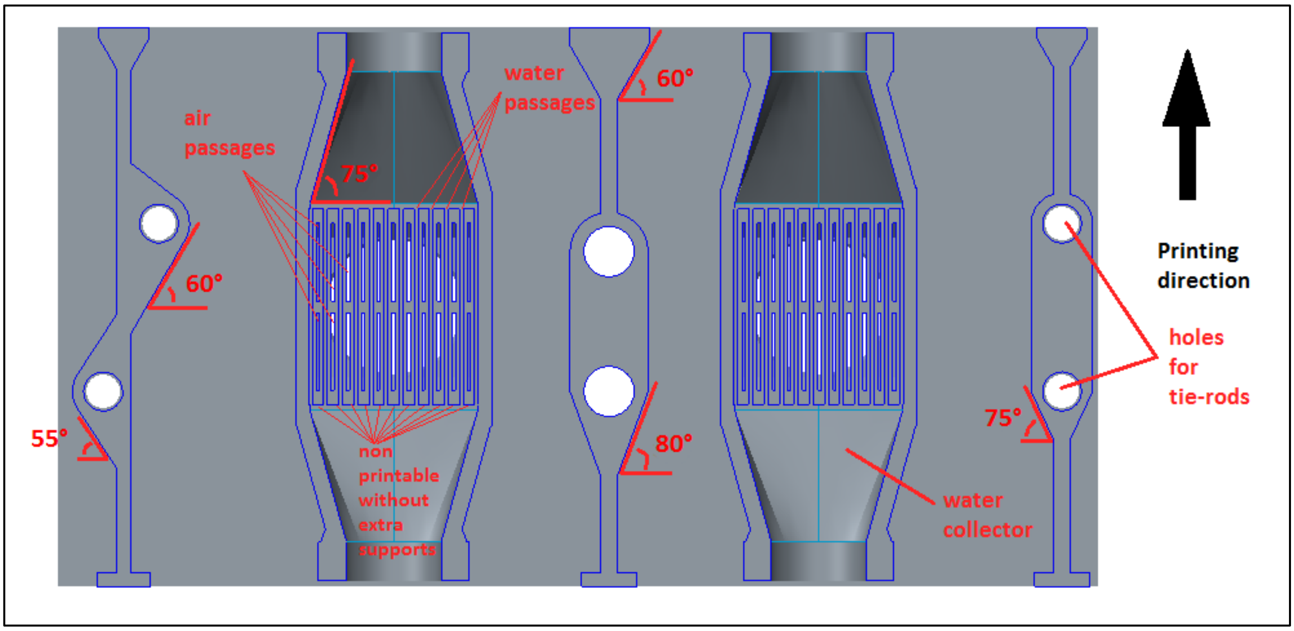

Figure 2.5 – First prototype section (plane orthogonal to the air direction)

2.3 Efficiency simplified calculation

The calculation is based on the iterative method illustrated in Keys and London [58]. Starting from the inlet conditions of both fluids, and guessing the outlet conditions, a first attempt calculus of the main non-dimensional parameters is possible using analytical expressions or experimental correlations. At last, the first attempt efficiency and outlet conditions are calculated. If needed, the process is repeated.

In the NTU method, the efficiency of the exchanger is a function of the NTU, of the fluids heat capacity rate $\dot{C}$, and of the type of exchanger (counter flow, cross flow, parallel flow, fluids mixed or not). This case efficiency is showed in equation 2.1 (cross flow with one fluid mixed).

$$\varepsilon_f = \frac{heat\ exchanged}{\max heat\ available} = \frac{T_{air\_in} - T_{air\_out}}{T_{air\_in} - T_{water\_in}} = 1 - e^{-B} \qquad [2.1]$$

$$B = \left(1 - e^{-NTU(\dot{C}_{min}/\dot{C}_{max})}\right)(\dot{C}_{max}/\dot{C}_{min}) \qquad [2.2]$$

The NTU parameter is a non-dimensional, its formulation is showed in equation 2.3a. U is the overall heat conductance [W/m^{2}K], A_{air} is the heat transfer surface on the air side [m^2], $\dot{C}_{air}$ is the air heat capacity rate [W/K]. In the U calculation, the aluminium walls conductivity was omitted as they give a small contribution due to their low thickness. So, U depends from the Nusselt number, the fluid conductivity, and the hydraulic diameter of the ducts. The Nusselt number in laminar flows is a function of the duct shape, while it is also function of the Reynolds number in the turbulent flows.

$$a)\ NTU = \frac{UA_{air}}{\dot{C}_{air}} \qquad b)\ U = \left(h_{c,air}^{-1} + \left(h_{c,water}A_{air}^{-1}A_{water}\right)^{-1}\right)^{-1} \qquad c)\ h_c = \frac{Nu\ \lambda_f}{D_h} \qquad [2.3]$$

In this case, both flows (the air flow and the water flow) could be considered laminar as the Reynolds number is always under 1200, so the Nusselt numbers of both fluids are function of the channels shape [59]. Key and London [58] gives its values for several geometries. The Nusselt values are taken from Key and London (Third edition, 1984 – Reprinted with correction in 1998, p. 121, figure 6.3), reported in figure 2.5.

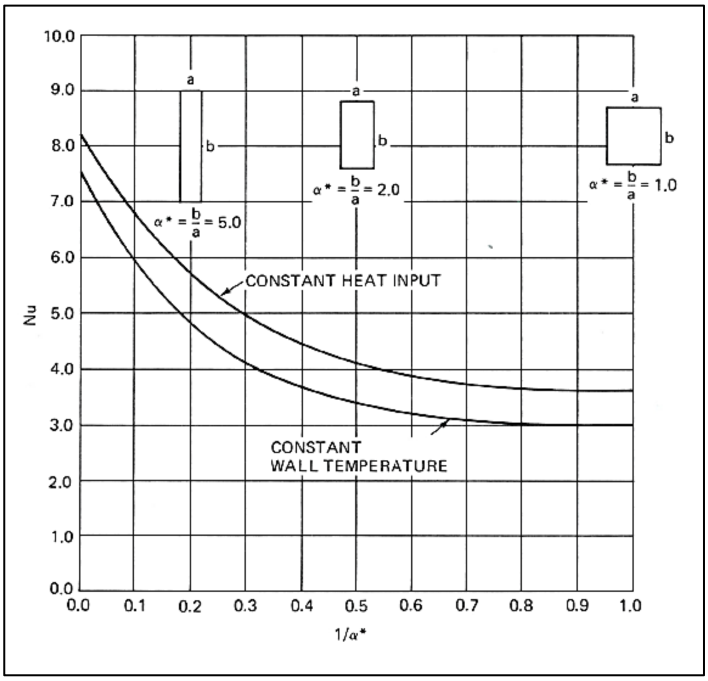

Figure 2.6 – Key and London's diagram: Nusselt as function of the duct geometry

Given that:

- The aluminium thermal conductivity is very high (237 W/m K)
- The wall thickness is low (6*10^-4 m)
- The convection coefficient on water side is from 10 to 20 times the one on the air side

the calculations were performed in the constant wall temperature hypothesis on the air side. In this case air side, a* (as defined in figure 2.5) is around 0.04 (exactly, 6/140).

Therefore, the following hypotheses are set:

- Steady flow
- Both fluids are in laminar flow
- The pressure drop is neglected
- The aluminum thermal resistance is neglected
- The roughness is neglected

The calculations were performed considering three air flow rate levels at the same inlet pressure and inlet temperature. The calculation initial and boundary conditions are collected in table 4. This set was chosen to predict the exchanger behaviour at the test operational condition, herein collected in table 5.

Table 6 - Exchanger calculation boundary conditions

Air inlet temperature range	360 K	Water inlet temperature	290 K
Air inlet pressure	2.5 bar	Water flow rate range	From 5 to 80 g/s
Air flow rate levels	2.2; 3; 3.7 g/s	Constant wall heat transfer hypothesis	
Constant wall temperature hypothesis			

Table 7 - Exchanger experimental boundary conditions

Air inlet temperature range	336 to 386 K	Water inlet temperature	290 K
Air inlet pressure	2.2 to 3 bar	Water flow rate range	5 to 70 g/s
Air flow rate range	2 to 3.7 g/s		

The calculation results are collected in figure 2.6a and 2.6b. In these figures it is shown that both the efficiency and the heat rate have a shallow correlation with the water flow rate, especially for water flow rates greater than 20 g/s. The heat transfer rate has the obvious upper limitation set by the air inlet heat rate.

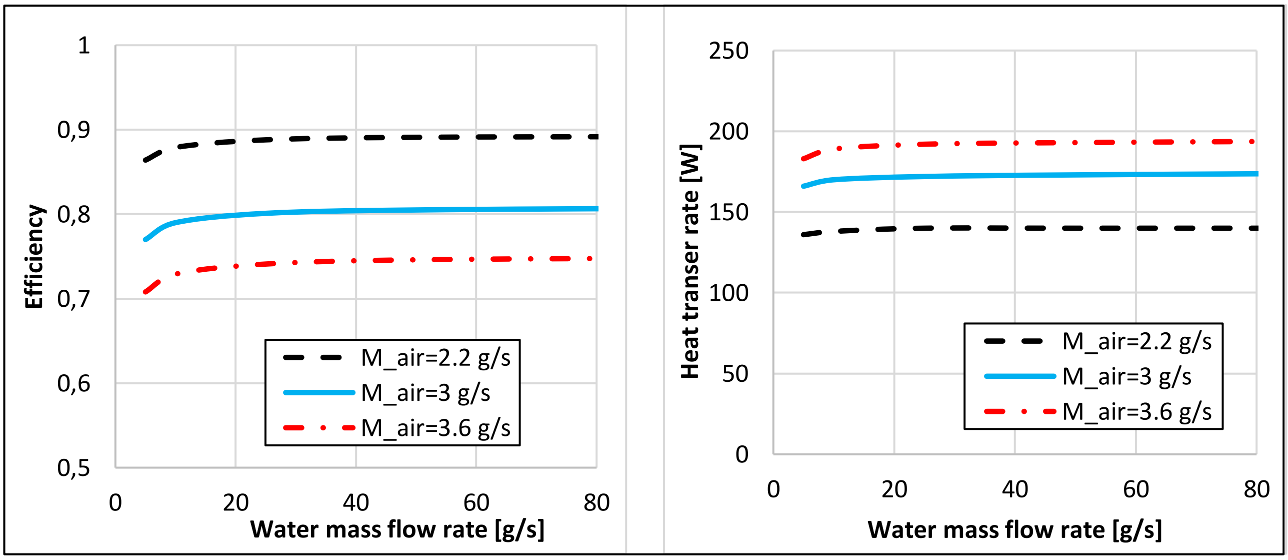

Figure 2.7a –Calculation results: exchanger efficiency depending on mass flow rates
Figure 2.7b – Calculation results: exchanger heat transfer rate depending on mass flow rates

2.4 The exchanger test bench

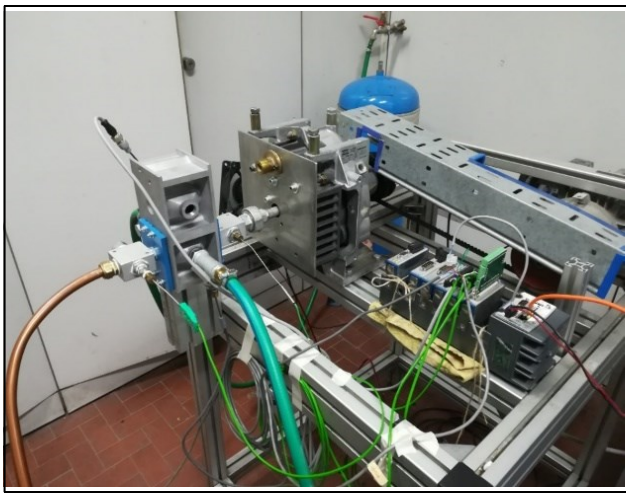

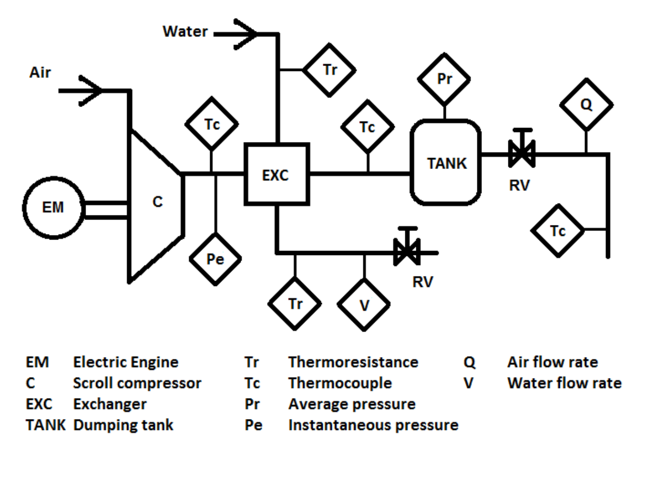

Figure 2.8a –Exchanger test bench: photo
Figure 2.8b – Exchanger test bench: Outline

Figure 2.8a shows the test bench and figure 2.8b illustrate its Outline. The hot air is provided by a scroll compressor, connected to the exchanger by a 30 cm long tube. The actual length of the tube is a trade-off between having too many heat losses and having too high-pressure waves. However, the compressor is expected to work not far from its nominal pressure ratio (β=2.5), as clarified below (see also table 5). The cold liquid is running water. The key features of the bench are collected in table 6. The temperatures are measured by k-thermocouples on air side and 4 wires thermoresistances on water side. A pulse quantometer measures the air volumetric flow rate, while a magnetic flow meter measures the water flow rate. A piezo-resistive sensor measures the average delivery pressure in the dumping tank and a piezo-electric one measures the instantaneous pressure upstream the exchanger. In appendix A are collected the sensors data sheet and a brief description of each of them. All the signals are collected by a National Instrument Compact Rio, and then sent to a PC via Ethernet (see also appendix B). The data acquisition code is written in LabVIEW. The Compact Rio worked in hybrid mode, using the FPGA for the high-speed signals, and the internal processor (C-Rio Real Time) for the low-speed ones.

Table 8 - Exchanger test bench features

Abbreviations	Name	Details	Accuracy
EM	Electric engine		
EXC	Exchanger	Cross flow aluminium MCHE	
C	Compressor	2.1 kW scroll compressor	
P	Average pressure sensor	Piezo-resistive sensor	±4%
I	Instantaneous pressure sensor	Piezo-electric sensor	±3%
Q	Volumetric flow meter	Turbine meter	±3%
RV	Regulation valve		
Tc	Temperature sensor	K type thermocouple	±1.5 K
Tr	Temperature sensor	4 wires thermoresistance	±0.4 K
V	Volumetric flow meter	Magnetic flow meter	±5%
TANK	Dumping tank		

2.5 The scroll compressor

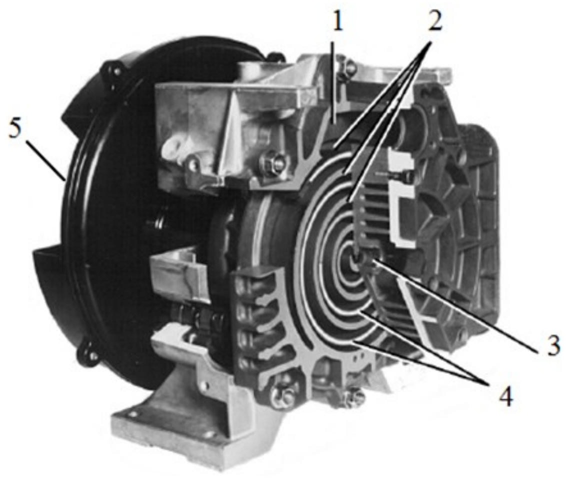

1 Inlet collector
2 Fixed spiral
3 Outlet port
4 Moving spiral
5 Cooling fan

Figure 2.9 – Scroll section

In figure 2.9 [11] the compressor used to test the exchanger is shown. The compressor was an oil less scroll compressor. Its known data are collected in table 7.

Table 9- Scroll compressor features

Maximum pressure	bar(a)	8
Nominal working pressure	bar(a)	7
Shaft nominal speed	RPM	2880
Maximum power consumption	kW	2.1
Sound pressure level	dB(A)	67
Minimum inlet air temperature	°C	0
Maximum inlet air temperature	°C	40

There are no indications about its internal volumetric compression ratio, nor about its ideal air flow rate. To calculate them, disassembling the compressor is needed, and then measuring the spiral characteristics. A test was performed to evaluate the compressor displacement engine size: the compressor air flow rate was measured running it at its nominal speed without any valve or tank at the compressor outlet (of course air was used as working fluid). So, with the minimum of pressure drops, the compressor air flow rate was 13.1 m^3/h, that is roughly 90 cm^3 per round. This is an underestimated evaluation, because the leakages are severe on this type of compressor (especially for oil-less ones).

[11] Figure taken from https://www.compressorworld.com/atlas-copco-1-5-hp-oilless-scroll-air-compressor-with-air-dryer-sf-1-116-aff-mono-230-1-volt-8153611614.html

Experimental data

The experimental runs were performed in steady flow. The scroll compressor suction pressure was 1 bar. The delivery pressure was varying from 2.2 to 3 bar in order to achieve different air temperatures. The maximum air temperature is 386 K. The tests were performed at three different scroll rotational speed levels: 1800 RPM, 2400 RPM and 2700 RPM to achieve different air flow rates. However, the actual air flow rate depends also by the delivery pressure, at it has influence on the scroll leakages. Also, the temperature has an influence, as the higher the whole scroll temperature the lower the inlet air density. So, it could not be possible to strictly control the air flow rate, but only achieve three wide levels: from 2 to 2.2 g/s; from 2.8 to 3.2 g/s; from 3.64 to 3.68 g/s. The water flow rate varied from 5 g/s to 70 g/s. Roughly, six water flow rate levels were considered, even though the water regulation valve did not allow a fine adjustment. These levels distribution is uneven: they are denser at low flow rate. It is so because the water flow Reynolds number is well beneath the transition threshold (at most the water Reynolds number is 350), so the flow is always laminar. The only effect of a change in the water flow rate is the change in the $\dot{C}_{min}/\dot{C}_{max}$ ratio (see equation 2), and the effect on the efficiency is monotonic and asymptotic at high water flow rates, as the calculations confirmed. The experimental condition are collected in table 5, already shown in paragraph 2.3.

First, the steady flow hypothesis was tested. The scroll compressor does not deliver a continuous air flow, as there is always an almost instantaneous volumetric compression/expansion phase that lead to a pressure wave in the discharge duct. This effect could be neglected in most applications, but in this case the pipe between the compressor and the exchanger was about thirty centimetres. So, an instantaneous pressure sensor was installed to measure the amplitude of the pressure waves. In figure 2.10a and 2.10b, the Fast Fourier Transformation of the pressure signal taken by the piezo-electric sensor is shown. The values refer to the three speed levels (1800 RPM, 2400 RPM, 2700 RPM) and two pressure levels (2.5 bar, 3 bar).

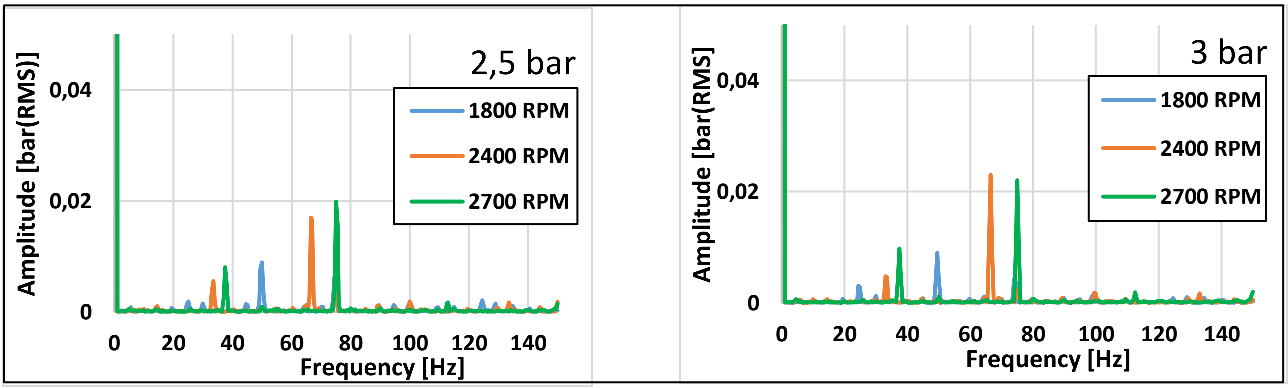

Figure 2.10a –Instantaneous pressure signal FFT. Delivery pressure at 2.5 bar
Figure 2.10b – Instantaneous pressure signal FFT. Delivery pressure at 3 bar

It can be seen that the amplitudes were absolutely less than 0.05 bar. As a first approach , these kind of pulsation were judged negligible. Moreover, both Chattopadhyay et al. [60] and Hemida et al. [61] stated that the heat transfer is poorly affected by pulsations.

Figure 2.11 shows the comparison between the calculation results (see figure 2.7a) and the experimental data. The experimental points on the graph are the mean values between repetitions at different inlet temperatures. As already explained above, the repetitions water flow rate is affected by high variance due to physical limits, and different temperatures means different pressures. A multivariate model could better explain the efficiency variance. However, at the moment, this is beyond the purpose of this work, even though it seems that the above explained calculation method is not consistent with the data. In fact, the differences between calculated and measured efficiency are too big, sometimes more than fifteen percentage points. This is true especially at high water and air flow rates (figure 2.11).

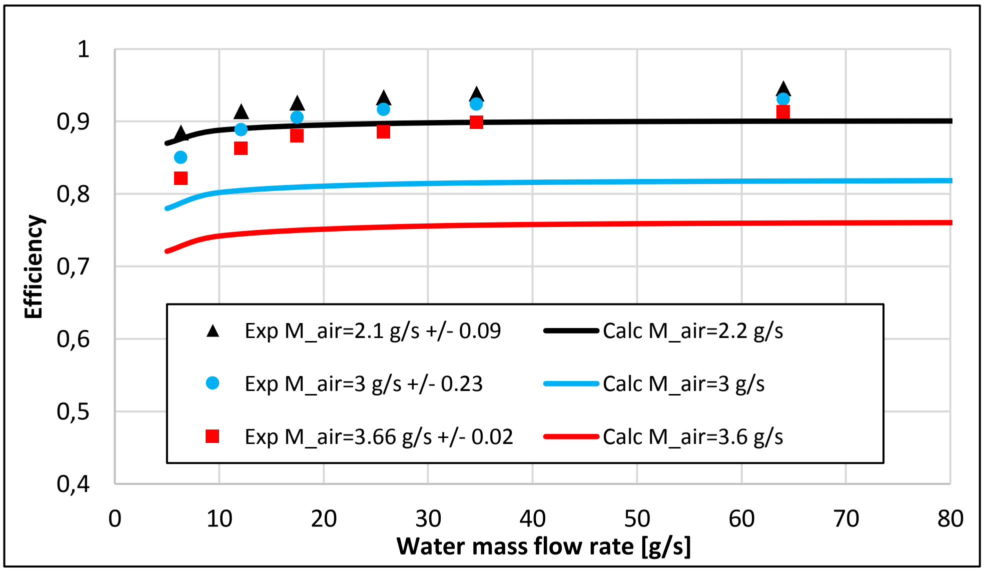

Figure 2.11 – Comparison between experimental data and first calculation

In figure 2.12, the experimental data are compared with a new calculation.

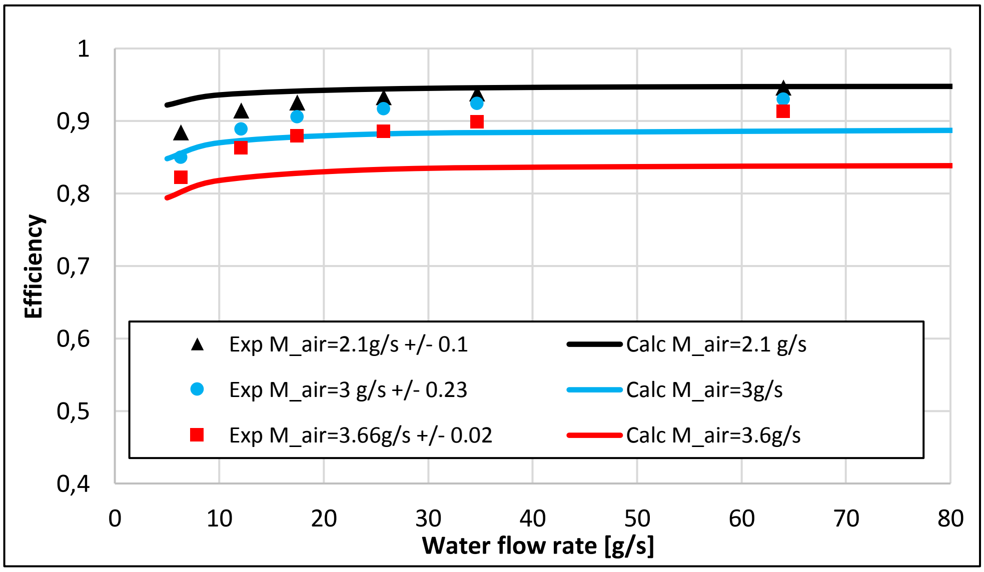

Figure 2.12 – Comparison between experimental data and second calculation

In the new calculation, the air side exchanging surface was risen. This was an attempt to consider the surface roughness. It was not possible to measure the walls roughness. Frazier [62] states that surfaces made with DLMS technique have a roughness of about 300 Ra. However, knowing the Ra is not enough to calculate the actual surface exposed to the fluid. After some trials, the surface was set to 423 cm^2, that is 100 cm^2 more than before (roughly 30% more than before). Figure 2.12 shows that the new calculation fit better with the experimental data. The maximum difference is now less than ten percentage point.

Figure 2.13 shows that the heat transfer rate is correlated to both the air Reynolds number and the inlet temperature. The linear regressions shown (dotted lines) are acceptable as their R^2 varies from 0.8 to 0.95. Overall, the maximum measured power density is 4 W/cm^3 This value is quite low, especially in comparison with other exchanger in literature [55]. However, this work test bench is not able to deliver more power[12], setting up an upper limit, that is about 270 W or 4.35 W/cm^3. Higher inlet temperature or higher air speed may lead to higher heat transfer rate. On the other hand, other works had their exchangers tested in high Reynolds number flow. For example, Kwon et al. [55] had their exchanger tested with the air Reynolds number varying from 10000 to 20000, and the available power was several times higher. For instance, their calculation for a Reynolds number of 1000 imply about 840 W/cm^3 available[13]. The extrapolation on this work data set (Re between 1000 and 1100) gives 13.8 W/cm^3 for an air inlet temperature of 523K. These values are comparable with Kwon et al. [55] calculated results (about 10 W/cm^3) for similar air inlet Reynolds number (Re =1000).

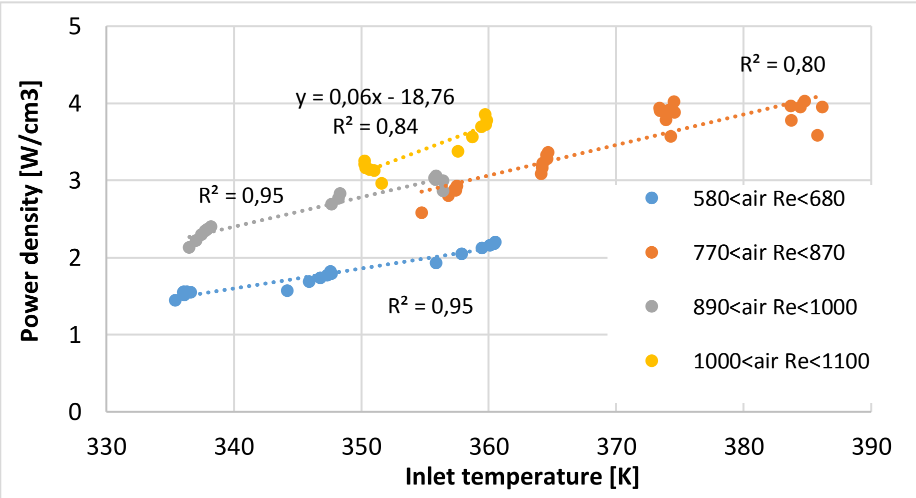

Figure 2.13 – Experimental power density

[12] The speed was already near the compressor limits and increasing the temperature means increasing the compressor delivery pressure, and this may lead to significant pressure waves in the exchanger. See also the beginning of this paragraph

[13] The available power is not provided by Kwon et al. [55], but it is possible to calculate based on the data available, presuming that the used air pressure is 1 bar. If not the case, the available power would be even higher

2.6 Compressor’s exchanger prototype

The exchanger was designed to be placed between the valves plate and the basement (figure 2.14a and 2.14b). In this way, the exchanger is part of the compression chamber, as it is between the piston and the valves. When the exchanger is placed, the discharge valves are to be placed on the valves plate; the intake valves are to be placed under the exchanger to avoid unnecessary dead volume (i.e. the intake ducts through the exchanger).

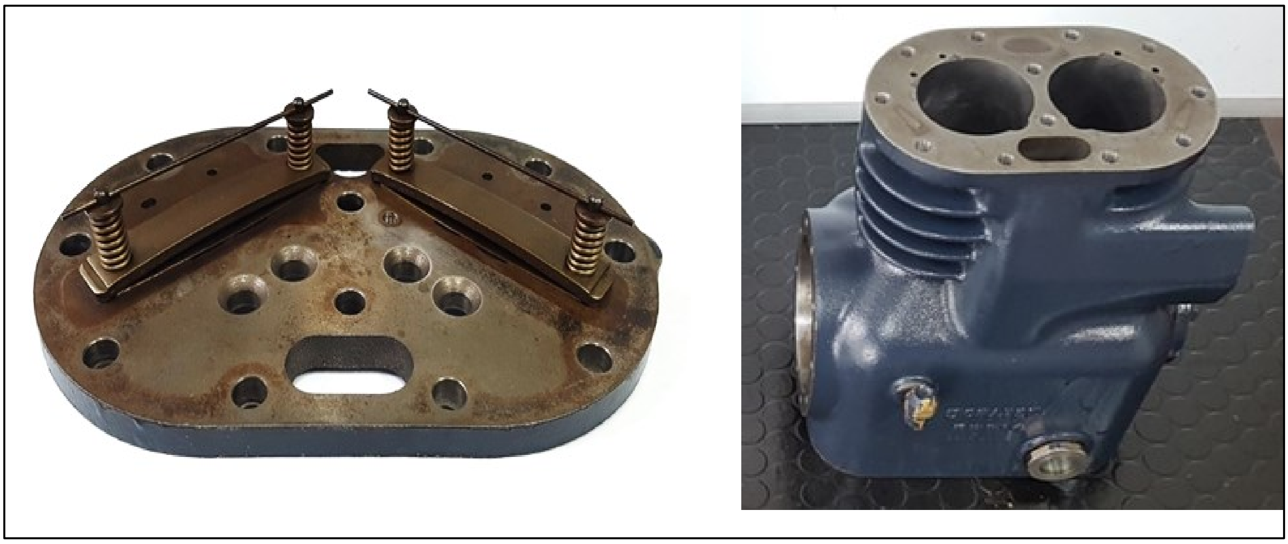

Figure 2.14a – Compressor valve plate
Figure 2.14b – Compressor basement

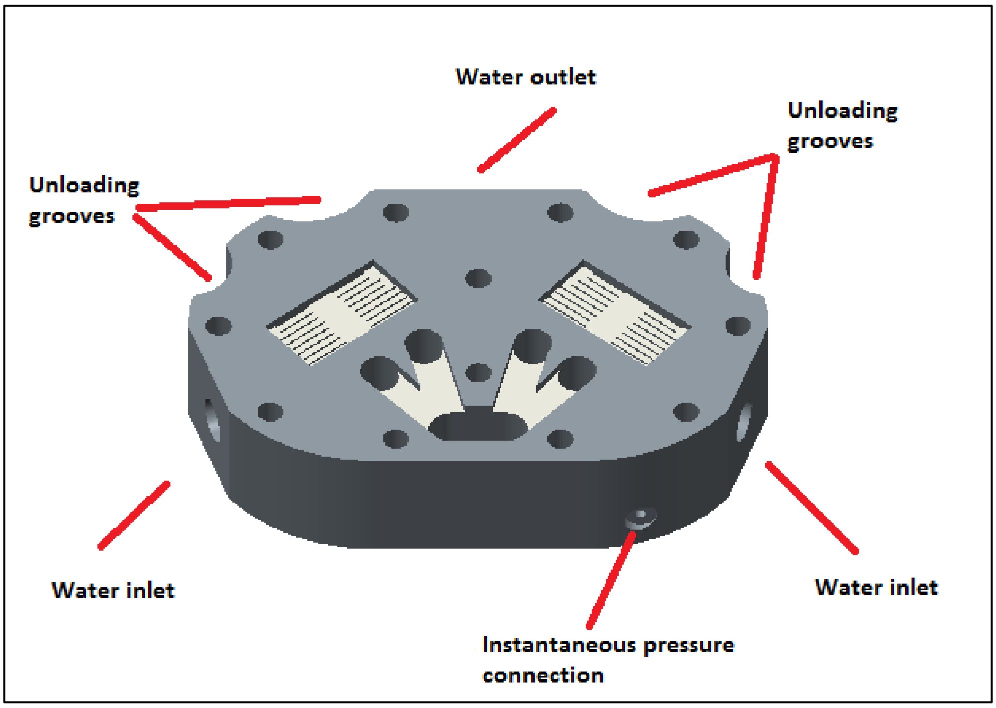

Figure 2.15 – Second exchanger prototype 3D sketch

So, it has a form similar to the valve plate, except for four unloading grooves (figure 2.15). It is difficult to print massive pieces with LMS techniques because of the residual stresses, that is why those groves were added. The exchanger cores were placed directly under the discharge valves, away from the intake valves. The reason is that placing a core above the discharge valves means placing it outside the compression chamber. These outside cores could have an enhancing effect on the performance, raising the intake air density (actually, it seems the case looking at the compressor experimental data in paragraph 3.3.1). However, the aim is to analyse the effect of an internal cooling, so it was preferred not to add another effect.

Figure 2.16a shows the instantaneous pressure connection in section. The vertical duct is circular with a diameter of 1 mm. The horizontal duct is divided into three zones. The first (from left to right) is circular with a diameter of 10 mm. Its function is to give a planar surface to seal the duct with a gasket. The second zone is a pre-drill hole for the threading needed by the sensor. The last zone has a square section with a vertical diagonal; its side is 1.2 mm long. Figure 2.16b shows the water ducts and collectors. The collectors could not be printed without additional supports. The ducts have rectangular section. They have much more cross-sectional area than in the previous exchanger in order to avoid potential occlusions while the exchanger is printed or during the normal working.

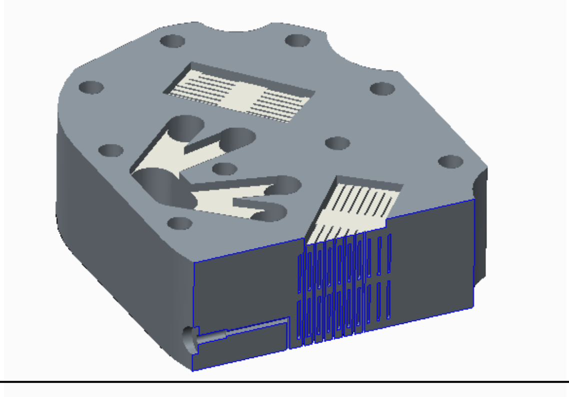

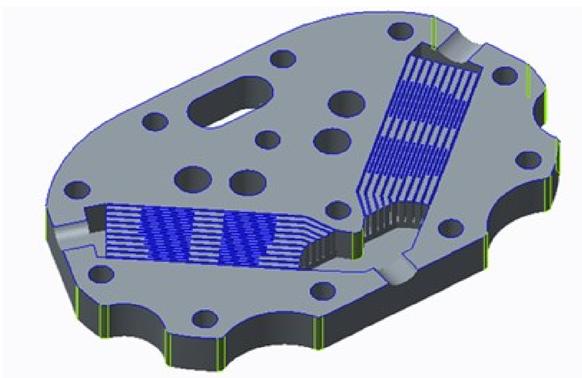

Figure 2.16a – Second exchanger prototype 3D section
Figure 2.16b – Second exchanger prototype 3D section

In table 8 the exchanger main data are collected. These data are taken from the CAD drowning and refer to one core.

Table 10- Exchanger second prototype features

Air channel length	37 mm	Liquid channel length	64 mm
Air channel width	600 µm	Liquid channel width	910 µm
Air channel height	13-17 mm	Liquid channel height	14 mm
Air side minimum total section	1.69 cm^2	Liquid channel cross section	12.74 mm^2
Air channels number	18	Liquid side minimum total section	127.4 mm^2
Air total exchanging surface	208.7 cm^2	Liquid channels number	10
Exchanger internal core air volume	6.3 cm^3	Liquid total exchanging surface	161.3 cm^2
Exchanger core total volume (air volume +liquid volume +aluminium volume)			52 cm^3

The compressor experimental data were used to size the exchanger. There are two possible heat transfer rate targets: the power required to decrease the temperature from the actual outlet temperature to the inlet temperature; the power required to achieve an isothermal compression. The latter is stricter, as it means that all the thermal power must be exchanged through the exchanger, while the heat is dissipated also through the cylinders and the lubricating oil.

Considering the first target, the worse available case was at outlet pressure of 5 bar at 1000 RPM. The inlet air was at ambient pressure. The table below (table 9) collect the data of interest for this aim.

Table 11- Reciprocating compressor experimental data used for the exchanger design

Speed	Outlet pressure p_{out}	Air flow rate $\dot{m}_{air}$	Air inlet temperature T_{in_air}	Air outlet temperature T_{out_air}
1000.9 RPM	4.98 bar	4.24 g/s	295.3 K	399.2 K
998,8 RPM	8.99 bar	3.31 g/s	295.9 K	417.3 K

The air flow rate refers to the entire machine, so every core must deal with half this rate. The heat transfer rate target is:

$$Heat\ transfer\ rate\ 1 = \left[\frac{\dot{m}_{air}}{2} c_{p\_air}\left(T_{out\_air} - T_{in\_air}\right)\right]_{5\ bar} = 224\ W$$

Where c_{p_air} is the air specific heat at constant pressure measured in kJ/kgK.

Considering the second target, the isothermal equation can be used, referring to the worst case that is the maximum pressure reached (9 bar). The test on the compressor without the exchanger shows that the maximum pressure in the cylinder reach 11 bar (see paragraph 4.3.3).

$$Heat\ transfer\ rate\ 2 = \left[\frac{\dot{m}_{air}}{2} R_{air} T_{in\_air} ln\left(\frac{p_{out}}{p_{in}}\right)\right]_{9\ bar} = 309\ W$$

Where R_{air} is the specific gas constant for dry air, that is 287.1 J/kgK.

The same calculations showed in paragraph 2.3 were used to estimate the new exchanger efficiency thus its thermal heat rate. In the calculation, the air total exchanging surface was increased by 30% to consider the surface roughness (see paragraph 2.6). The calculated efficiency is 72.9 % and the calculated heat transfer rate is 312 W.

2.7 Bibliography

[48] Cardone, M., and Gargiulo, B. “Design and experimental testing of a Mini Channel Heat Exchanger made in Additive Manufacturing”. Energy Procedia, 148 (2018), 932-939.

[49] Esarte, J., et al. "Optimizing the design of a two-phase cooling system loop heat pipe: Wick manufacturing with the 3D selective laser melting printing technique and prototype testing." Applied Thermal Engineering 111 (2017): 407-419.

[50] Thompson, Scott M., et al. "Additive manufacturing of heat exchangers: A case study on a multi-layered Ti–6Al–4V oscillating heat pipe." Additive Manufacturing 8 (2015): 163-174.

[51] Arie, Martinus A., Amir H. Shooshtari, and Michael M. Ohadi. "Experimental characterization of an additively manufactured heat exchanger for dry cooling of power plants." Applied Thermal Engineering 129 (2018): 187-198.

[52] Khan, Mesbah G., and Amir Fartaj. "A review on microchannel heat exchangers and potential applications." International journal of energy research 35.7 (2011): 553-582.

[53] Wang, Hailei, and Richard B. Peterson. "Performance enhancement of a thermally activated cooling system using microchannel heat exchangers." Applied Thermal Engineering31.14-15 (2011): 2951-2962.

[54] Qi, Zhaogang, Yu Zhao, and Jiangping Chen. "Performance enhancement study of mobile air conditioning system using microchannel heat exchangers." International Journal of refrigeration 33.2 (2010): 301-312.

[55] Kwon, Beomjin, et al. "High power density air-cooled microchannel heat exchanger." International Journal of Heat and Mass Transfer 118 (2018): 1276-1283.

[56] Mundinger, D., et al. "Demonstration of high-performance silicon microchannel heat exchangers for laser diode array cooling." Applied physics letters 53.12 (1988): 1030-1032.

[57] Wu, Peiyi, and W. A. Little. "Measurement of the heat transfer characteristics of gas flow in fine channel heat exchangers used for microminiature refrigerators." Cryogenics 24.8 (1984): 415-420.

[58] W.M. Kays, A.L. London, “Compact Heat Exchangers”, Third Edition, Krieger Pub, Co, Malabar,FL, 1998.

[59] Shah, Ramesh K., and Alexander Louis London. “Laminar flow forced convection in ducts: a source book for compact heat exchanger analytical data”. Academic press, 2014.

[60] Chattopadhyay, Himadri, Franz Durst, and Subhashis Ray. "Analysis of heat transfer in simultaneously developing pulsating laminar flow in a pipe with constant wall temperature." International communications in heat and mass transfer 33.4 (2006): 475-481.

[61] Hemida, H. N., et al. "Theoretical analysis of heat transfer in laminar pulsating flow." International Journal of Heat and Mass Transfer 45.8 (2002): 1767-1780.

[62] Frazier, William E. "Metal additive manufacturing: a review." Journal of Materials Engineering and Performance 23.6 (2014): 1917-1928.

3 Experimental activities on the compressor

The experimental work is made up by several parts. The first one is the designing of the test bench and the test routine. Then there is the choice (or the designing and production) of the test bench components and their possible modification. Then there is the actual experimental activity and the data analysis. These steps are not meant to be in a strict order, but the relationship between them is so close that even an analysis on preliminary data (one of the "last" steps) could bring to little or radical changes on the test bench design (the "first" step). Moreover, some of the activities were carried out in parallel. Actually, this was the case. However, the following paragraphs are presenting in a strict order for the sake of clarity. The data analysis is placed on a distinct chapter.

3.1 The test bench design

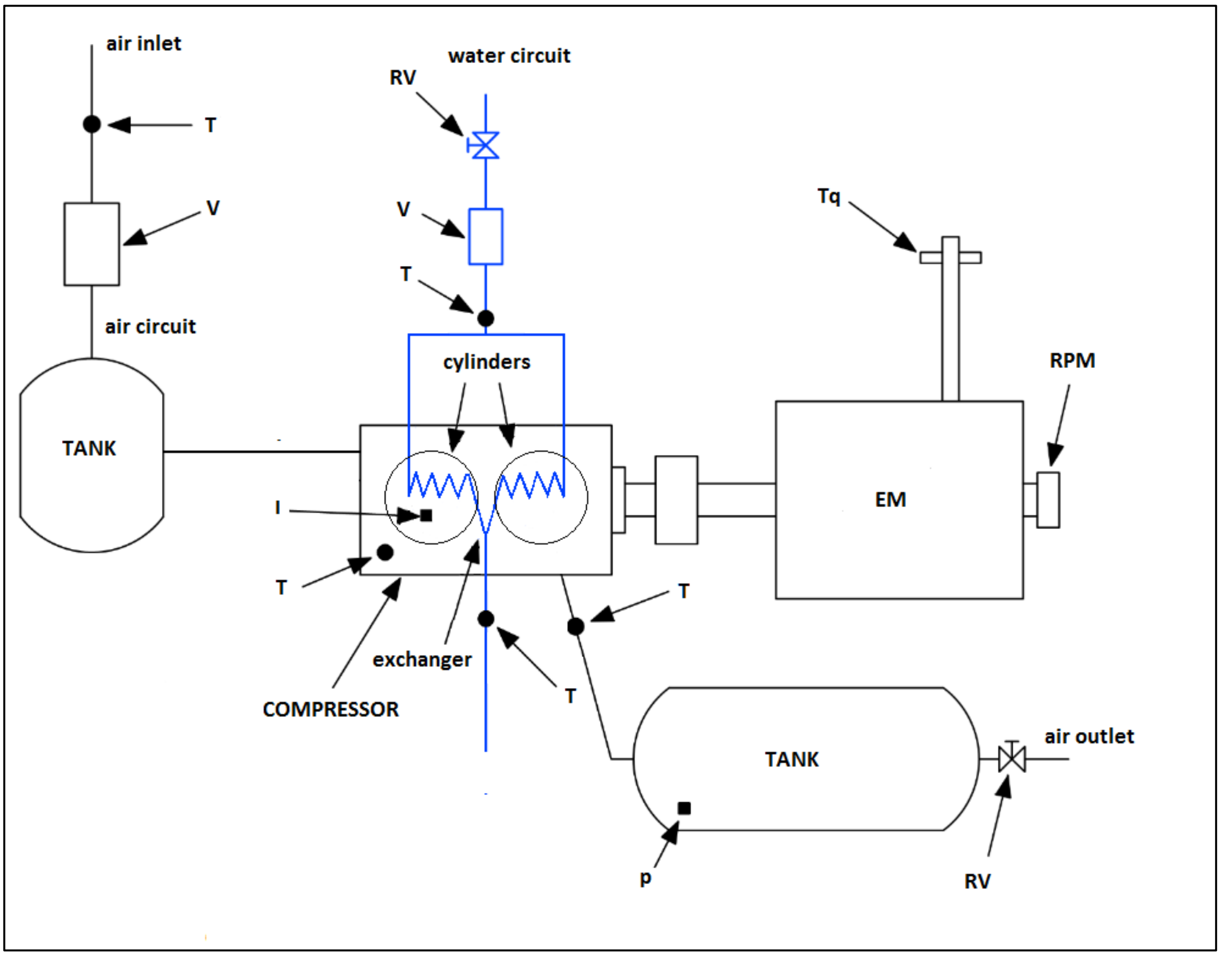

Figure 3.1 – Compressor test bench Outline

Table 12 - Compressor test bench features

EM	Electric motor	**RV**	Regulation Valve
C	Compressor	**p**	Discharge pressure
TANK	Dumping tank	**T**	Temperature sensor
I	Indicated pressure	**V**	Volumetric flow meter
Tq	Torque measure	**RPM**	Encoder

Figure 1 illustrate the test bench Outline and table 1 collects its main component. The test bench core consists of a two- cylinder compressor, driven by a 5.5 kW three-phase oscillating casing motor. A rigid coupling connects the compressor to the motor. The compressor is provided with a removable internal heat exchanger (see paragraph 2.7 and 3.2.2). The compressor fan, keyed on its axis, is replaced by electric external fans. A load cell (torque measure) and an encoder (velocity measure) are used to measure the compressor mechanical power consumption. A piezo electric sensor placed in the compression chamber measures the internal pressure and, together with the encoder, gives the indicated diagram.

There are also two tanks, one placed before the compressor intake and the other after the compressor supply manifold. A pulse quantometer measures the intake volumetric flow rate. The air temperature is measured by two k-type thermocouples both at suction and supply pipe. Another thermocouple measures the oil temperature in the compressor crankcase (which is also the sump of this compressor). The average pressure is measured by a piezo resistive sensor placed into the delivery tank.

Finally, there is the water circuit for the heat exchanger refrigeration. It consists of a regulation valve, two thermoresistances (they measure the temperature before and after the exchanger) and a flow rate electromagnetic sensor.

Although not present in figure, there are two other components. The electric motor is provided with an inverter so that its rotary speed can be changed. All the sensors electric signals are collected by an electronic board and then sent to a computer.

3.2 The test bench main components

3.2.1 The reciprocating compressor

The chosen machine is an open type, two-cylinder, reciprocating compressor. It is an open type compressor made for refrigeration facilities from 1 kW to 25 kW of refrigerating capacity. It has two cylinders in line with bore 60.5 mm and stroke 60 mm. This type of compressor was chosen because it can withstand high pressures, as its maximum operative pressure could be over 20 bar (when using R404A with a condenser at 50°C, the maximum operative pressure is around 23 bar). Its robustness allows to overcome a pressure ratio of 10, which is one of this work aims.

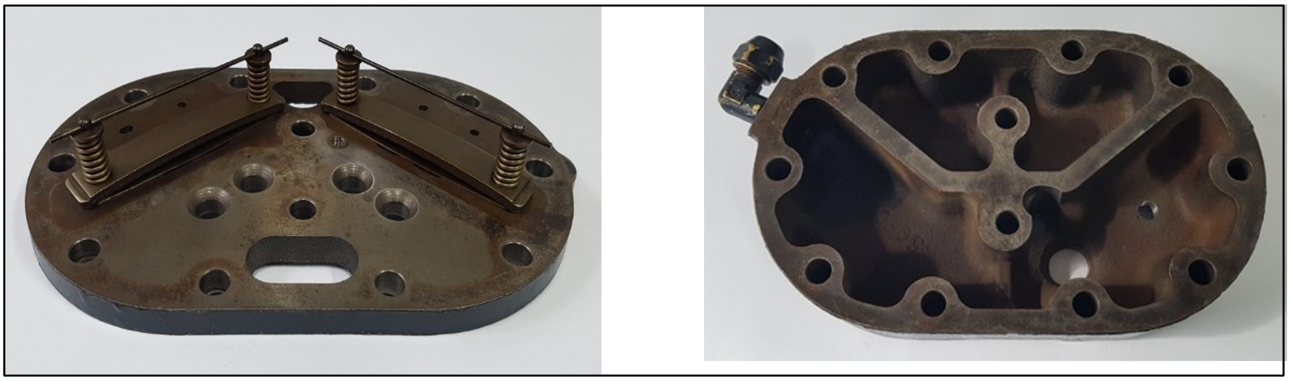

Figure 3.2a – Compressor valve plate
Figure 3.2b – Compressor head

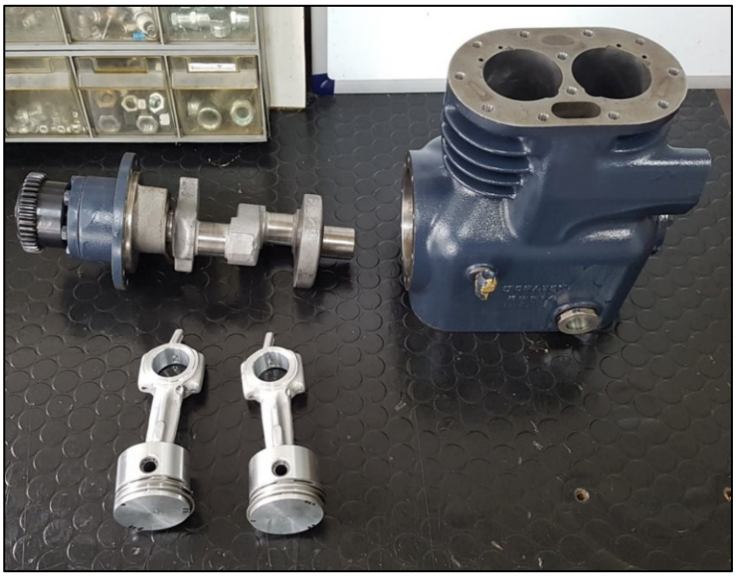

Figure 3.3 – Compressor basement, crankshaft and pistons

The lubricating is a splash type lubrication. In figure 3, the connecting rod big ends are visible: there are two palettes (one for each connecting rod) that enhance the lubrication.

The original fan (keyed on the compressor shaft) is removed because it absorbs some work. Three electric external fans were added to replace it.

3.2.2 The heat exchanger

The heat exchanger is the core component of this work. It should be as more efficient as possible while being as smaller as possible, and those targets are opposing ones. The first target importance is obvious, while the latter needs an explanation. As explained before (see chapter 1), the exchanger must be part of the compression chamber, thus its air ducts are part of the compressor clearance volume. Of course, the total cross section of the air ducts must be enough to avoid pressure drops. So, these air ducts should be as narrow as possible and enough numerous to obtain an adequate total cross section. Moreover, the exchanger should have an as high as possible exchanging surface.

The simplest method to build such an exchanger is the additive manufacturing technique. In particular, the Direct Metal Laser Sintering technique was used.

It is designed as a platform which is as large as the valve plate. The platform must be placed between the basement and the valve plate. Two crossflow heat exchangers, one for every cylinder, are placed under the discharge valves. The suction valves must be placed under the exchanger, in correspondence of the exchanger suction holes.

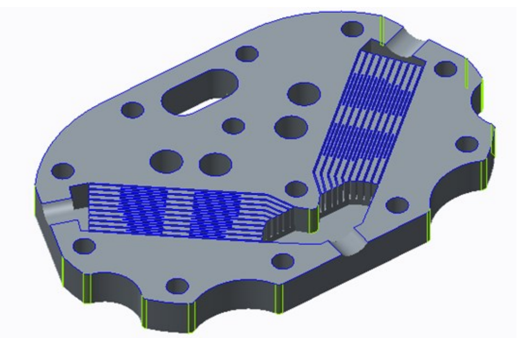


Figure 3.4a – Exchanger 3D section
Figure 3.4b – Exchanger photo

3.2.3 Sensors

The table below collects the several sensors used in the current activity.

Table 13 - List of sensors

Sensor	Details	Place	Accuracy
Average pressure sensor	Piezo-resistive sensor	Delivery tank	±4%
Encoder	500 pulse per round	Motor shaft	
Instantaneous pressure sensor	Piezo-electric sensor	Compression chamber	±3%
Temperature sensor	K type thermocouple	Compressor inlet and outlet, crankcase (sump)	±1.5 K
Temperature sensor	4 wires thermoresistance	Exchanger water inlet and outlet	±0.4 K
Volumetric air flow meter	Turbine meter	Compressor inlet	±3%
Volumetric water flow meter	Magnetic flow meter	Exchanger inlet	±5%
Force transducer	S type strain gauge	At one end of the motor moment arm	

In appendix A are collected the sensors data sheet and a brief description of each of them.

3.2.4 The data acquisition system

All the sensors signals are collected by a National Instrument (NI) board and then sent to a computer. The board is a C-Rio type (C-Rio 9022), that is "a combination of real-time controller, reconfigurable IO Modules (RIO), FPGA module and an Ethernet expansion chassis" [wiki https://en.wikipedia.org/wiki/CompactRIO].

An FPGA board is an integrated circuit which functionalities are programmable by the user using a specific language, so that it is as flexible as a software program and as reliable as a hardware circuit. The real time controller is a standalone processor that allow the user to implement some logic or data acquisition rate and triggers. Nowadays, NI Real Time system is based on a Linux based OS, but once it was based on PharLap OS or VxWorks OS. The real time controller is slower and less reliable than the FPGA. On the other hand, the FPGA circuit is very strict on resources, must be programmed at a lower level, and does not allow data logging. The signals are collected by replaceable IO modules, each designed for a certain task (for instance: thermocouples module, fast analog signals IO module, digital signal IO module and so on). Each module can be read from the FPGA board or the Real Time system (RT) with a limitation: each module cannot be read from both FPGA and RT in the same activity. Even though the C-Rio board could be used standalone, the Ethernet connection allow to connect it to a computer for data monitoring, logging and post processing.

LabVIEW is the development environment from National Instrument by which the user can interact with National Instrument hardware such as C-Rio boards. Thanks to LabVIEW, the same language is used to program the FPGA board, the RT system and the PC monitoring and logging interface. Being three hardware components (FPGA, RT, computer), three interconnected programs are needed. In appendix 2 the three programs are briefly analysed.

3.2.5 The test routine

The test activity consisted of two different phases, as, after a first campaign, the obtained data gave some hints on how to perform another campaign. In the first one, the compressor was tested in three different configuration: the original compressor (without his original fan, but adding external electric fans as already said in paragraph 3.2.1); the compressor with the exchanger but without water in it; the compressor with the exchanger and water flow rate of 40 kg/h. Those configurations are respectively named STD, EXC_0, EXC_40 (table 12). For every configuration, three different speed levels were considered: 600 RPM, 800 RPM, 1000 RPM. For every speed level, four different pressure levels were performed: 3 barA, 5 barA, 7 barA, 9 barA. These pressures are measured in the outlet tank. So, in the first campaign there are 36 treatments, and each one of them has two repetitions. Each treatment is performed in thermal steady state: while staying at constant speed, for each configuration, the compressor backpressure is kept increasing until the desired pressure level. Once reached, it is kept constant until all the monitored temperatures had become constant; then all the measures were saved. After reached 9 barA, the procedure is repeated while decreasing the pressure.

The second campaign considered one speed level (1000 RPM) and one new configuration (EXC_200): the compressor is installed with the exchanger and water flow rate is set at 200 kg/h. The pressure levels were the same, except that there was one more level: 13 barA.

Table 14- Configurations

STD	Standard compressor
EXC_0	Compressor with the exchanger, but no water inside the exchanger
EXC_40	Compressor with the exchanger, water flow rate set at 40 kg/h (≈ 10g/s)
EXC_200	Compressor with the exchanger, water flow rate set at 200 kg/h (≈ 60g/s)

3.3 Compressor experimental data

In this paragraph the experimental data are shown and analysed. There are three sub-paragraphs. The first two are concerned with global physical quantities data (such as temperature, power, air flow rate and so on). In the first one, the first campaign data are shown, while the latter focuses on the second campaign data. Data on the indicated pressure measurements are presented in the third sub-paragraph.

3.3.1 The first test campaign: global quantities analysis

As explained in paragraph 1.4.2, there are two conflicting phenomena: the exchanger cooling and the exchanger air volume. The first one lowers the specific work consumption; the latter raises it.

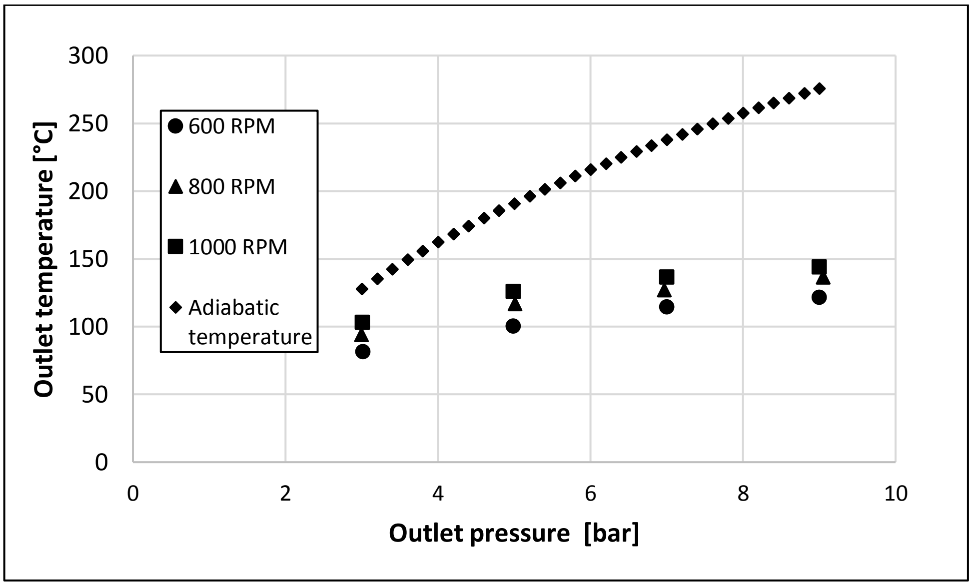

Figure 3.5 – Measured outlet temperature in standard configuration

The first experimental evidence is that the standard compressor is already "cooled". Its structure and lubrification system facilitate heat dissipation. Figure 3.5 shows the acquired outlet temperature in standard configuration. As can be seen, the heat dissipation increases towards higher delivery pressures. It is of course reasonable. Higher pressure means higher temperatures, thus higher temperature differences towards the ambient. On the other hand, higher speed implies higher temperatures, because of a shorter available time for heat exchange. So, the exchanger cooling effect is limited, especially at a lower speed.

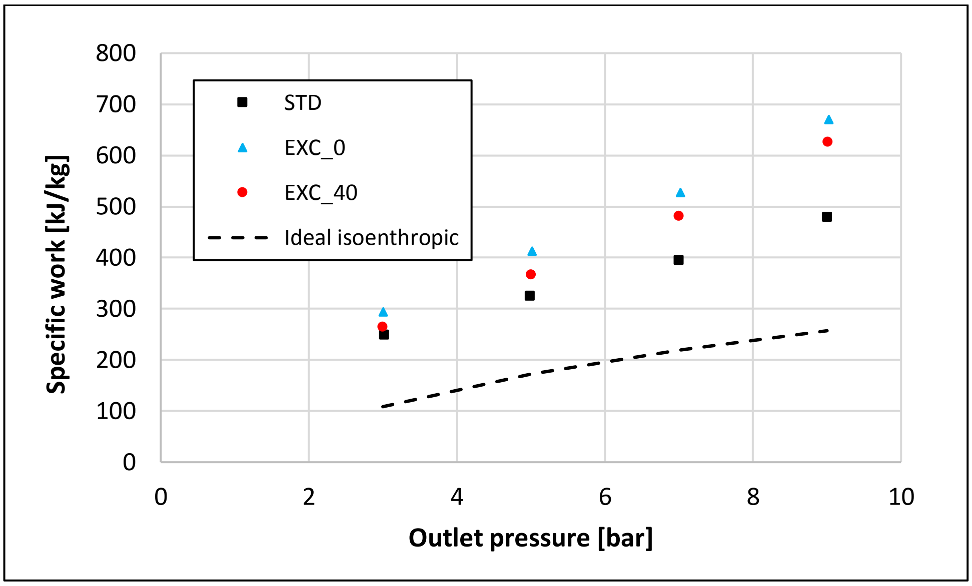

Figure 3.6 – Experimental specific work at 600 RPM

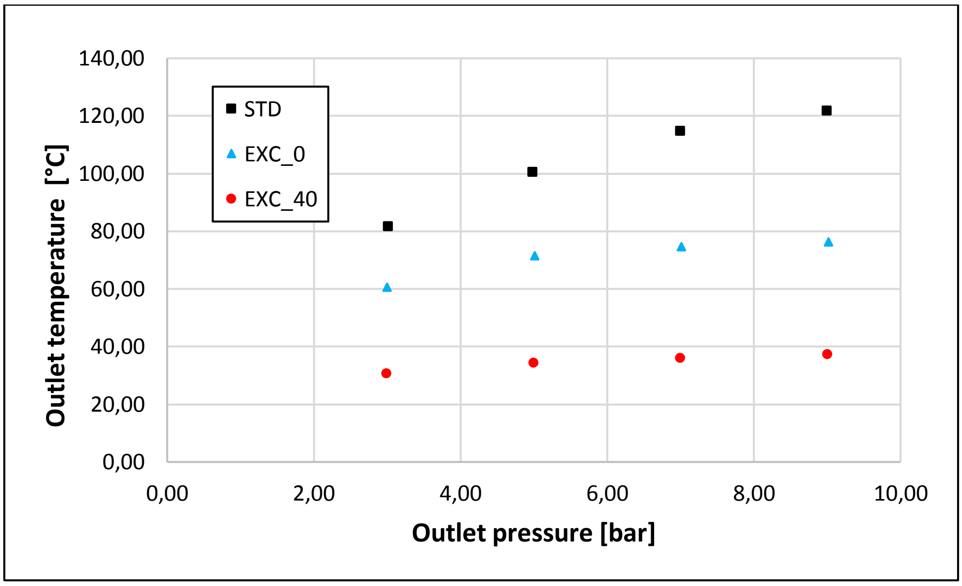

Figure 3.7 – Experimental outlet temperature at 600 RPM

Figure 3.6 shows the specific work consumption for every configuration at 600 RPM. This is the worst case of the campaign. The negative effect of the exchanger air volume is prevalent on the cooling effect. The first effect is roughly shown by the difference between the STD configuration (standard compressor) and the EXC_0 one (compressor with exchanger and without water). It is said "roughly" because the exchanger has a significant cooling effect even without water, as it can be seen in figure 3.7. The difference between the EXC_0 and EXC_40 configuration is the effect of the water cooling. The result is not satisfying, as the EXC_40 specific work is higher than in the STD configuration. However, as already stated, the test at 600 RPM is the worst case.

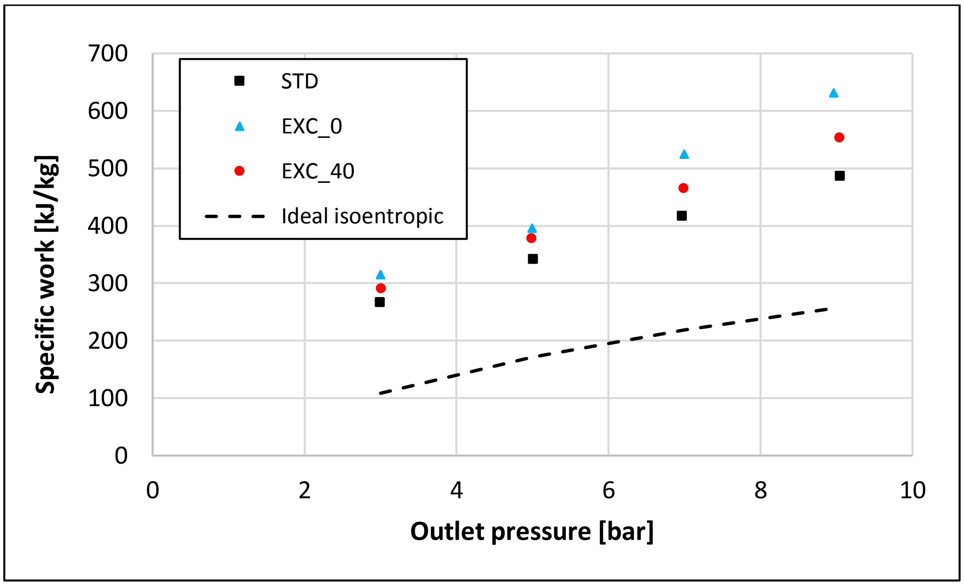

Figure 3.8 – Experimental specific work at 800 RPM

Figures 3.8 and 3.9 shows the specific work consumption and the outlet temperature for every configuration at 800 RPM. The performance of the EXC_40 configuration is not satisfying yet. Nevertheless, it is slightly better than the one at 600 RPM. In fact, the cooling effect is stronger than in the 600 RPM case, as the maximum temperature in the refrigerated configuration (EXC_40) goes from about 30 °C (303 K) to 40 °C (313 K) for both speeds, while the standard (STD) configuration maximum temperature goes from about 82 °C (355 K) to 120 °C (393 K) at 600 RPM and from 94 °C (367 K) to 135 °C (408 K) at 800 RPM.

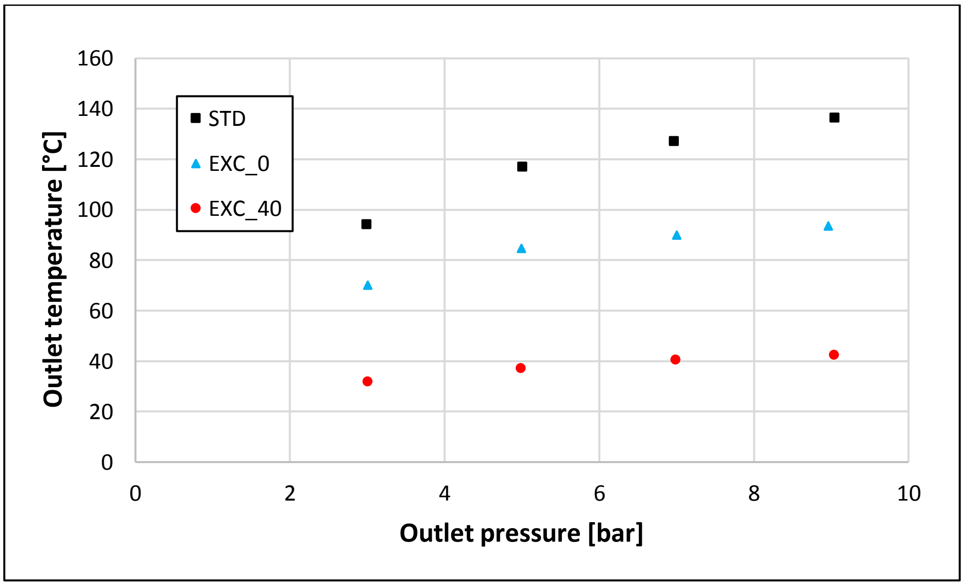

Figure 3.9 – Experimental outlet temperature at 800 RPM

Finally, at 1000 RPM, the cooling effect is strong enough to balance the volume effect (see figure 3.10) as the EXC_40 configuration specific work consumptions are almost the same of those in STD configuration. In figure 3.11 shows the outlet temperatures in these cases.

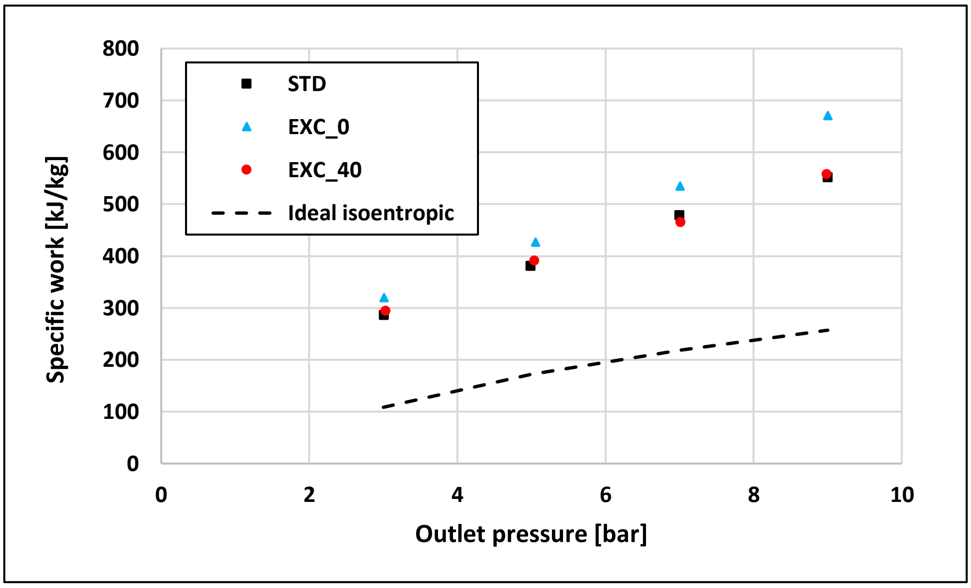

Figure 3.10 – Experimental specific work at 1000 RPM

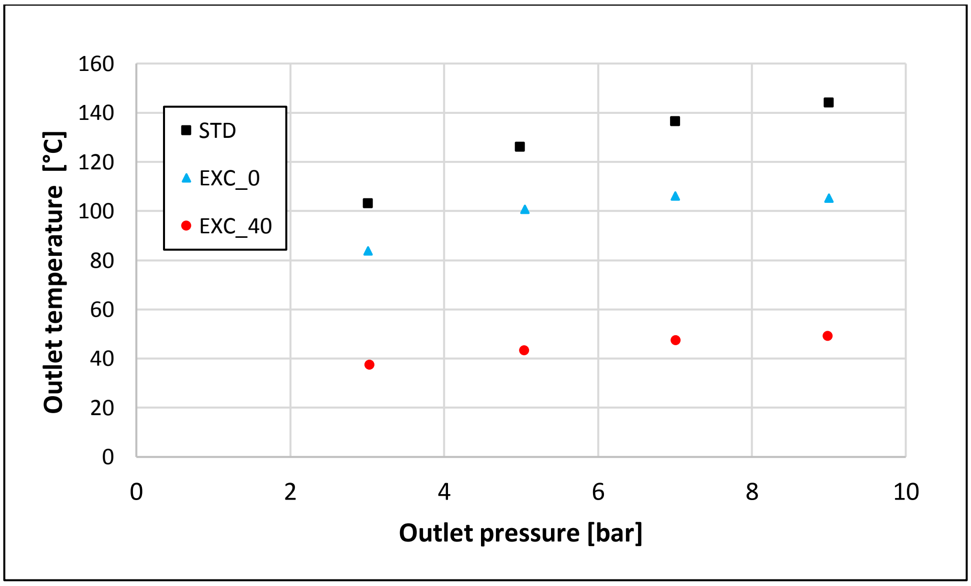

Figure 3.11 – Experimental outlet temperature at 1000 RPM

Focus on case at 1000 RPM and split the specific work into its factors: power consumption and air flow rate.

$$Specific\ work\ \left[\frac{kJ}{kg}\right] = \frac{Power\ consumption\ [W]}{Air\ flow\ rate\ \left[\frac{g}{s}\right]} \quad [3.1]$$

There are two conflicting effects: while going from the STD to EXC_0 configuration, both power consumption and air flow rate decrease (figure 3.12). This leads to an increased specific work (as observed before), because the air flow rate variations are relatively bigger than the power variations.

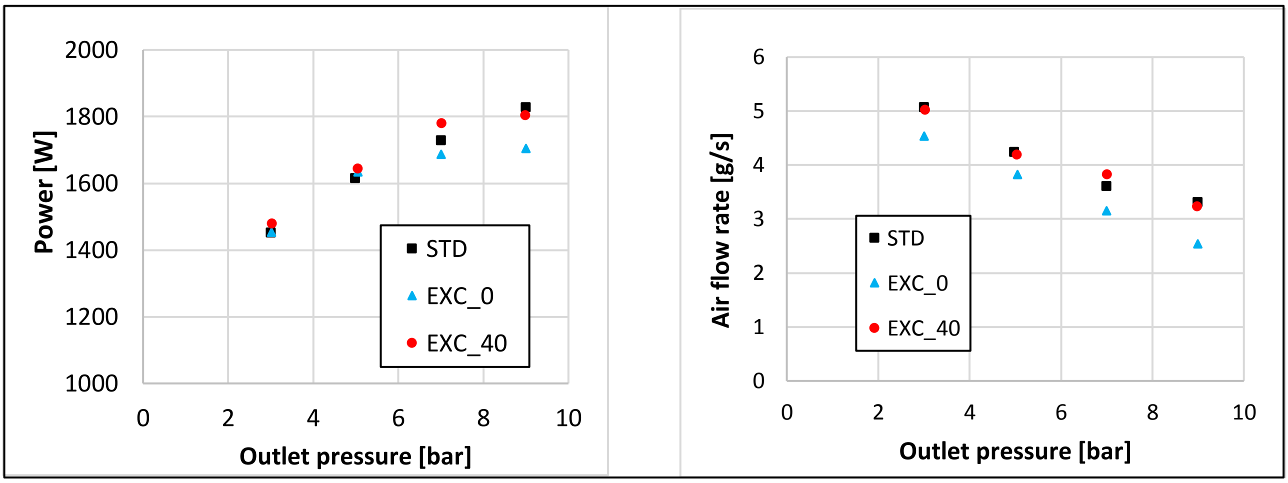

Figure 3.12a – Experimental power consumption at 1000 RPM
Figure 3.12b – Experimental air flow rate at 1000 RPM

This is true at every speed, as showed in figure 3.13 and figure 3.14. Figure 3.13 shows the percentage variation of the average power consumption and air flow rate between STD and EXC_0 configuration.

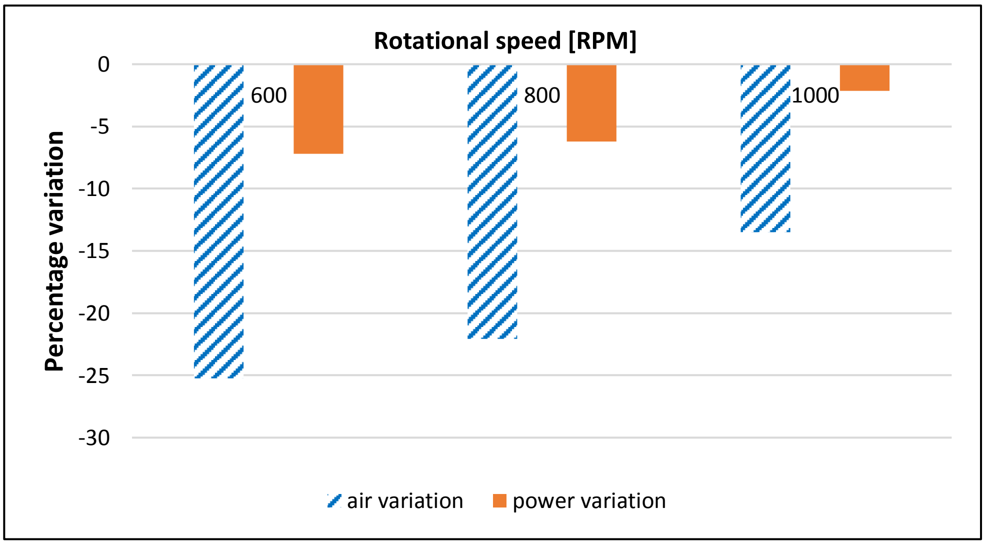

Figure 3.13 – Percentage variation of the average power consumption and air flow rate between STD and EXC_0 configuration

For example, at 600 RPM the percentage variation of the average power is

$$Percentage\ variation_{EXC_0-STD,\ 600} = \frac{\overline{P_{EXC\_0,600}} - \overline{P_{STD,600}}}{\overline{P_{STD,600}}} * 100 \qquad [3.2]$$

Where

$$\overline{P_{EXC\_0,600}} = \frac{1}{4}\left(\overline{P_{\beta=3}} + \overline{P_{\beta=5}} + \overline{P_{\beta=7}} + \overline{P_{\beta=9}}\right)_{EXC\_0\ ,\ 600RPM} \qquad [3.3]$$

$$\overline{P_{STD,600}} = \frac{1}{4}\left(\overline{P_{\beta=3}} + \overline{P_{\beta=5}} + \overline{P_{\beta=7}} + \overline{P_{\beta=9}}\right)_{STD\ ,\ 600RPM} \qquad [3.4]$$

While each $\overline{P_\beta}$ means the average of the two repetition of the same treatment (same pressure, speed, configuration). The percentage variation of the average air flow rate is calculated in the same way.

Figure 11 shows that the presence of the exchanger mainly affects the air flow rate, while the power consumption is almost unaffected. Figure 12 shows the water effect. The percentage variation is calculated between the EXC_40 and EXC_0 configuration. For example, at 600 RPM it is:

$$Percentage\ variation_{EXC\_40-EXC\_0,\ 600} = \frac{\overline{P_{EXC\_40,600}} - \overline{P_{EXC\_0,600}}}{\overline{P_{EXC\_0,600}}} * 100 \qquad [3.5]$$

$$\overline{P_{EXC\_40,600}} = \frac{1}{4}\left(\overline{P_{\beta=3}} + \overline{P_{\beta=5}} + \overline{P_{\beta=7}} + \overline{P_{\beta=9}}\right)_{EXC\_40\ ,\ 600RPM} \qquad [3.6]$$

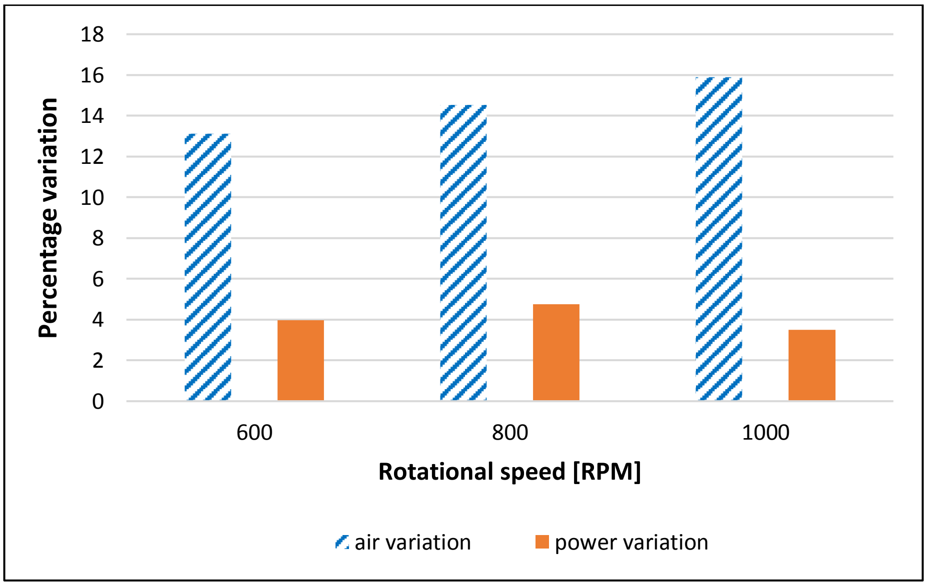

Figure 3.14 – Percentage variation of the average power consumption and air flow rate between EXC_0 and EXC_40 configuration

As before, the effects are contrasting, and the air flow rate effects are preponderant. The results are shown in figure 3.15.

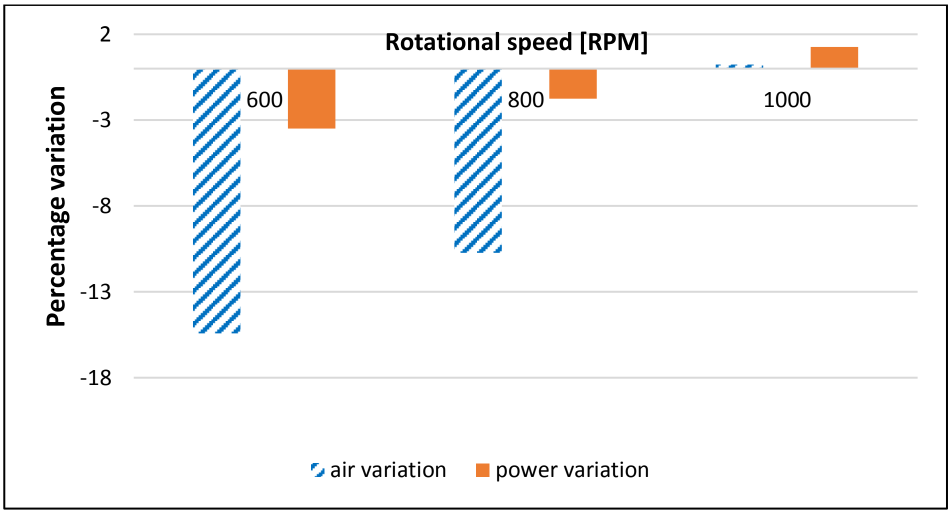

Figure 3.15 – Percentage variation of the average power consumption and air flow rate between STD and EXC_40 configuration

As shown in figures 3.13, 3.14 and 3.15, the water effect ok power consumption is insufficient to overcome the decrement of air flow rate both at 600 RPM and 800 RPM, though the situation is better at 800 RPM. This is also shown in figure 3.16. At 1000 RPM the water effect on the air flow rate almost counter the volume effect, also because the higher the speed the smaller the volume effect (see figures 3.12 and 3.13).

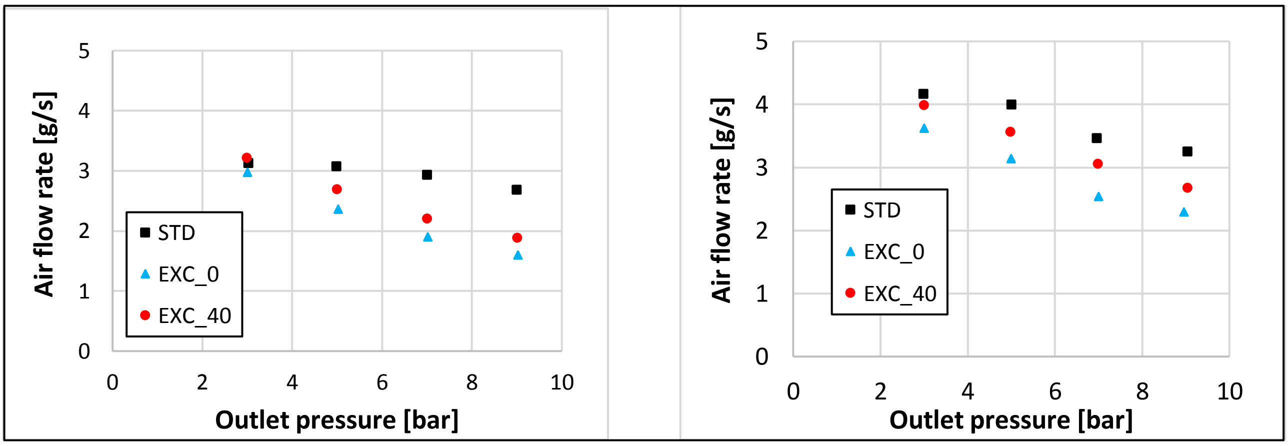

Figure 3.16a – Experimental air flow rate at 600 RPM
Figure 3.16b – Experimental air flow rate at 800 RPM

The reason why the water has an influence on the air flow rate is that the cooler the inlet air the more density it has. The compressor is a volumetric machine, so a cooler air means more air in the cylinder. The point is that a normal compressor has a hot head and crankcase, and the fresh air increase its temperature (i.e. decrease its density) passing near or through them.

The compressor with the exchanger is cooler overall. The head temperatures were measured by a manual laser thermometer: in the STD configuration and 1000 RPM the head temperatures were between 80 °C (353

K) and 120 °C (393 K), while they were between 26 °C and 35 °C (299 K and 308 K) in EXC_40 configuration at the same speed[14]

Figures 3.7, 3.9 and 3.11 show the outlet air temperature for all treatments. It can be seen that EXC_40 configuration air temperatures are always under 50 °C (323 K), while the maximum temperature in the STD configuration is 145 °C (418 K). Moreover, the increasing in temperature for each bar is few degrees in the EXC_40 configuration, while it is bigger in the STD configuration. So, the exchanger stabilizes the outlet temperatures on a low level almost regardless of the delivery pressure[15]. This effect is even stronger on lubricating oil temperature to the point that there is no more correlation between outlet pressure and oil mean temperature in the EXC_40 configuration. As showed in figures 3.17 and 3.18, the EXC_40 oil temperature is always lower than 40 °C (313 K), while they are usually above 40°C in the STD configuration. The temperature on pressure rate is bigger in the STD configuration as well[16].

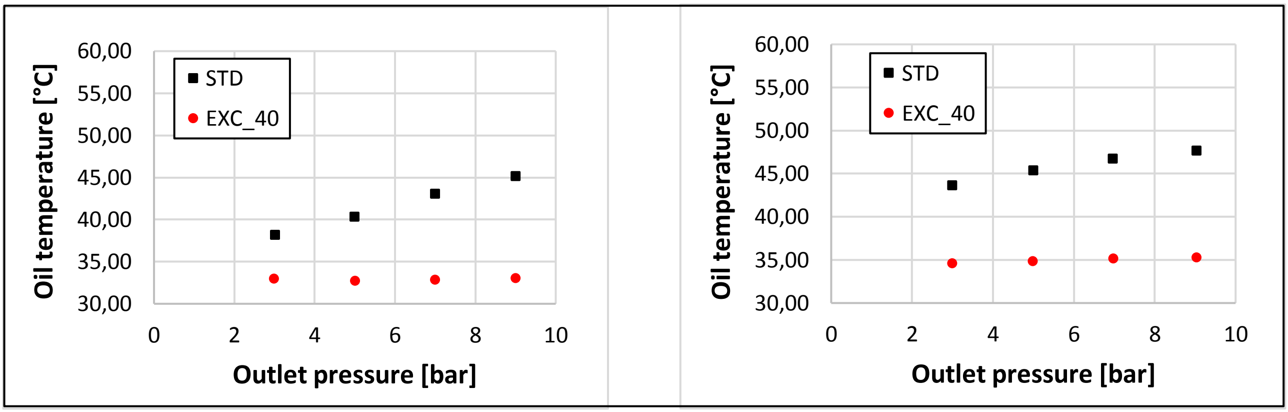

Figure 3.17a – Experimental oil temperature at 600 RPM
Figure 3.17b – Experimental oil temperature at 800 RPM

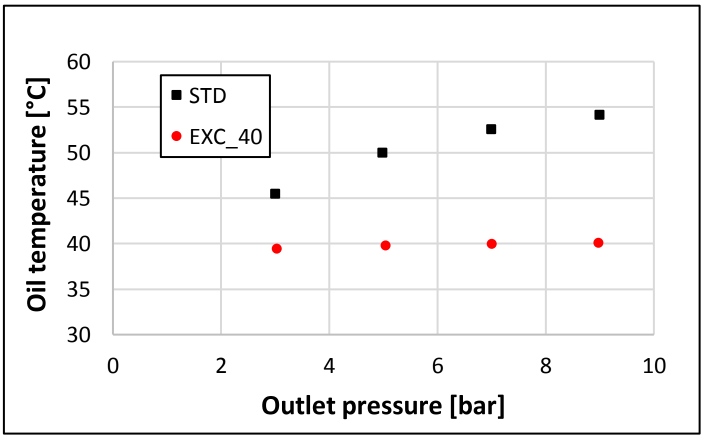

Figure 3.18 – Experimental oil temperature at 1000 RPM

[14] These measures were taken through a manual laser thermometer. The point detected was always the same, near the compressor outlet. The temperature of the head was not uniform
[15] for example, at 1000 RPM, EXC_40 configuration, the linear regression slope is 1.98 K/bar, while R^2 is 0.922 and p-value is 1.54E-4. At 1000 RPM, STD configuration, the linear regression slope is 6.69 K/bar, while R^2 is 0.919 and p-value is 1.73E-4. In both cases, the correlation is present.
[16] for example, at 1000 RPM, STD configuration, the linear regression slope is 1.43 K/bar. On the other hand, in the EXC_40 configuration at 1000 RPM the correlation is shallow: R^2 is 0.09 and p-value is 0.48. The temperatures are between 37.4 °C and 40.6 °C

3.3.2 The second campaign: achieving high compression ratio

The behaviour illustrated in the previous sub-paragraph suggest that the exchanger allow the compressor to work at a higher-pressure ratio. The tested compressor is usually used in cooling plant, so it is designed to bear up to 26 bar[17]. The test bench weak point is the outlet pipeline, so the copper outlet pipe and the tank were replaced with a steel pipe (the tank allowed no more than 10 bar).

The second campaign consist of five treatments at 1000 RPM; the outlet pressure was: 3 bar, 5 bar, 7 bar, 9 bar, 13 bar. The first four treatments were performed to compare this campaign to the previous. The last one (13 bar) was the maximum pressure allowed by the regulation valve[18]. The compressor had the exchanger and the water flow rate was 200 dm^3/min. This configuration will be named EXC_200.

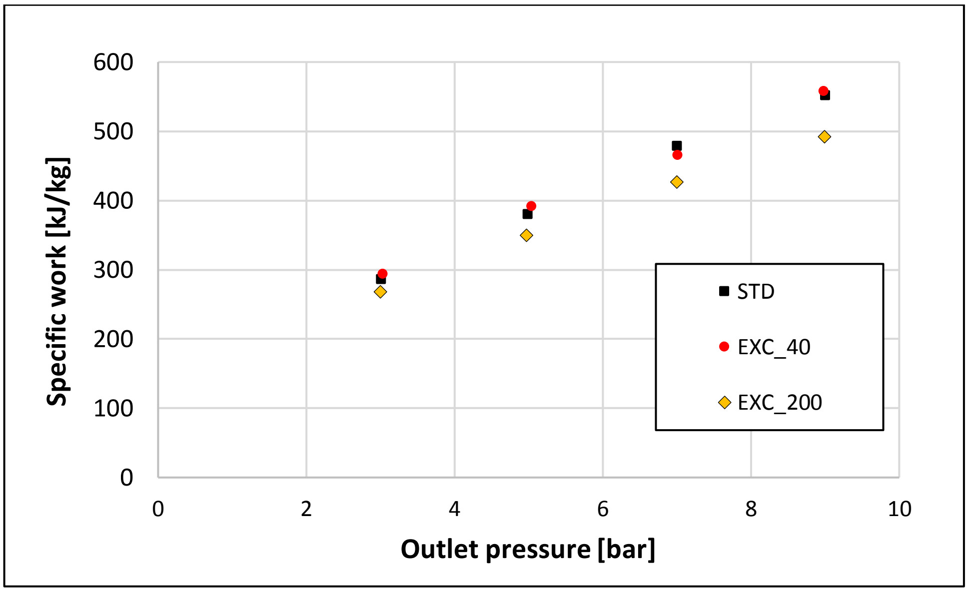

Figure 3.19 – Comparison of the specific work consumption at 1000 RPM with the EXC_200 configuration

Figures 3.19 shows the comparison between the first campaign test and the second; in particular it shows the comparison of the specific work consumption: the EXC_200 configuration has a specific work consumption that is about 10% lower than the EXC_40 and STD.

---

[17] The manufacturer allows 55 °C as limit temperature for the R404a fluid. At such condensing temperature, the pressure is about 26 bar. See appendix C for the compressor technical sheet

[18] Without the dumping tank, the regulation was problematic. The higher the pressure the coarser the regulation. The last treatment outlet pressure was 12.7 bar, while the other pressures were no more than 0.05 bar away from the nominal pressure

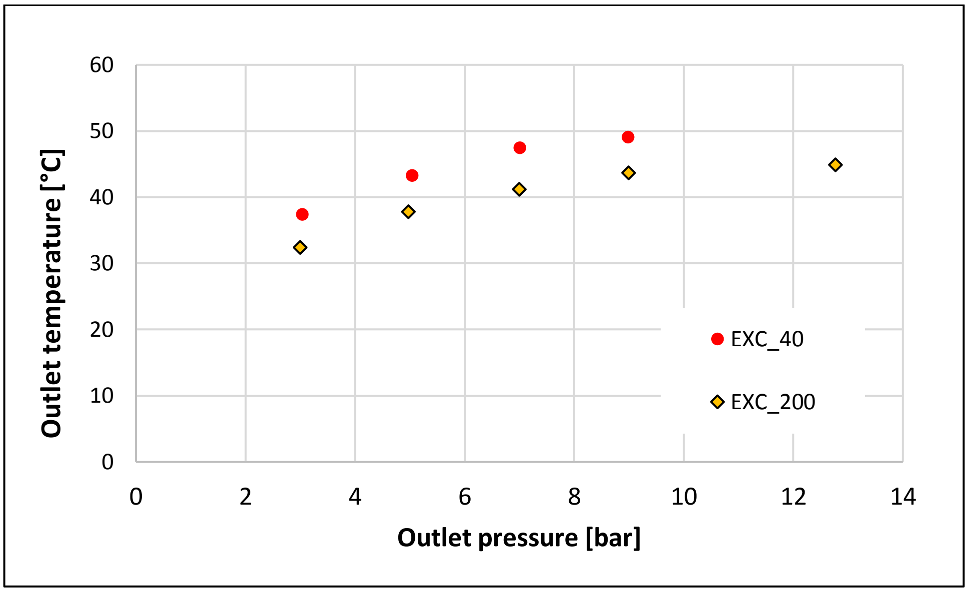

Figure 3.20 – Comparison with the outlet temperature between EXC_40 and EXC_200 configuration

Moreover, the temperatures are so low that reaching higher pressure is safe, as regard oil degradation and thermal stress of sensible component, such as valves and sealing gasket (Of course, it is meant that it is safe within the structural limits of the test bench). Figure 3.20 shows that an increased water flow rate strengthens the cooling effect: on average, the air outlet temperatures are 5 °C lower than in the EXC_40 configuration. The last treatment (13 bar) is in line with the others (figures 3.21 and 3.22). The EXC_200 configuration is not only capable of reaching high pressure without any thermal issue (see also figure 3.23 and 3.24), but it is also convenient compared to a single stage compressor.

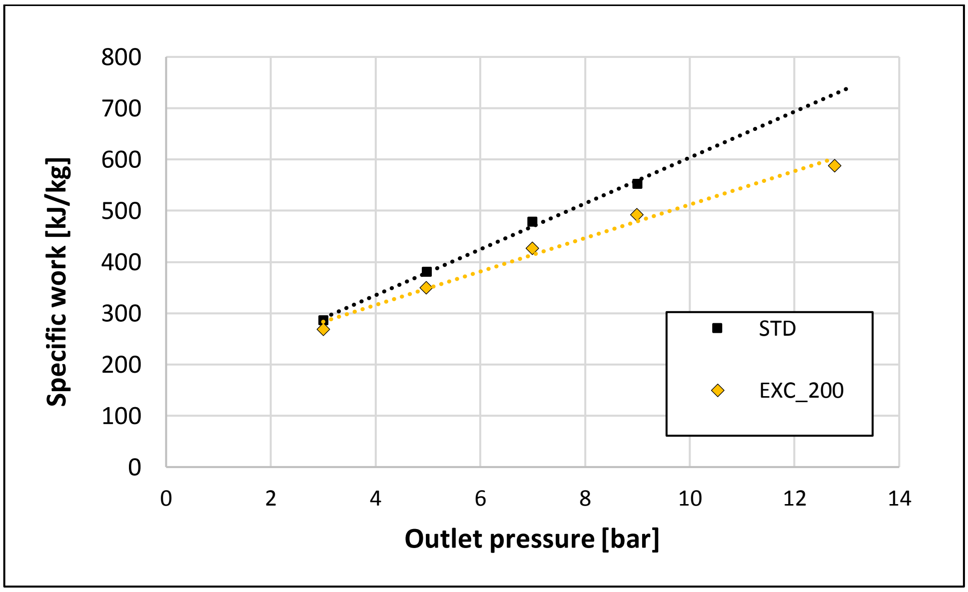

Figure 3.21 – Focus on the specific work consumption vantages of the EXC_200 configuration

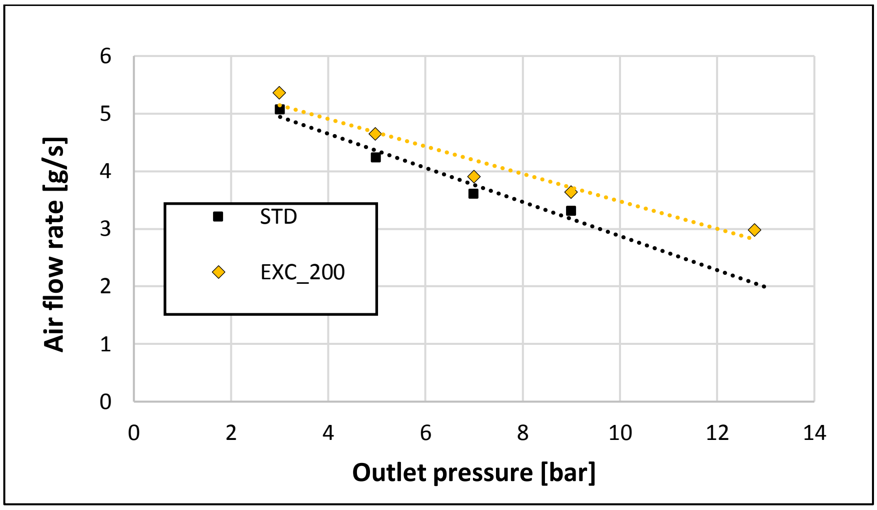

Figure 3.22 – Focus on the air flow rate vantages of the EXC_200 configuration

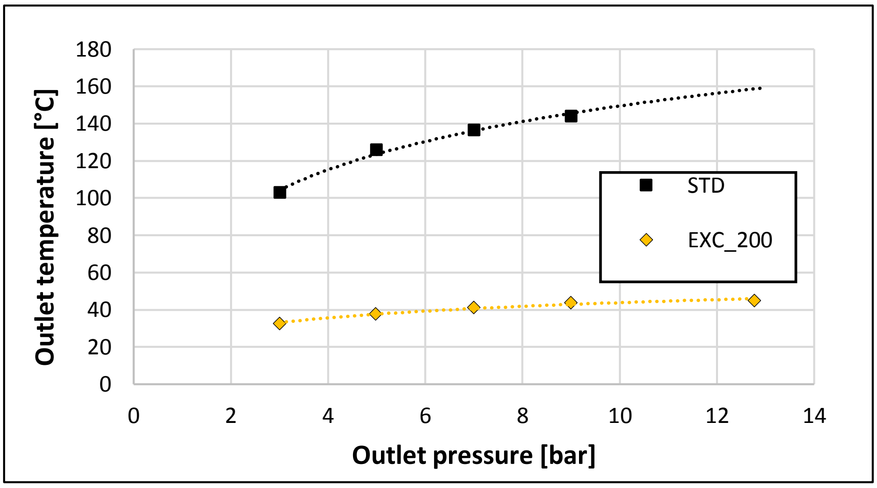

Figure 3.23 – Comparison with the outlet temperature between STD and EXC_200 configuration

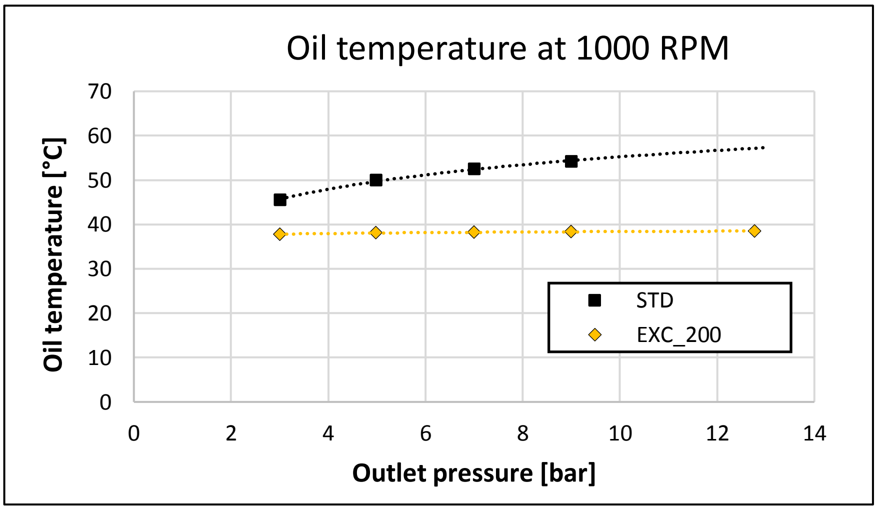

Figure 3.24 – Comparison with the oil temperature between STD and EXC_200 configuration

3.3.3 Indicated diagrams analysis

In this paragraph, the indicated diagrams are being analysed. For the sake of brevity, this paragraph deals with the 1000 RPM tests indicated diagrams only. Figure 3.25 shows the indicated specific work variance between the repetitions of each treatment at 1000 RPM. It was calculated as below:

$$Variance\ \% = \left|100 * \left(\frac{w_1 - w_2}{\overline{w_{1-2}}}\right)\right| \qquad [3.7]$$

Where w_1 and w_2 are the two repetitions indicated work and $\overline{w_{1-2}}$ is the average between them.

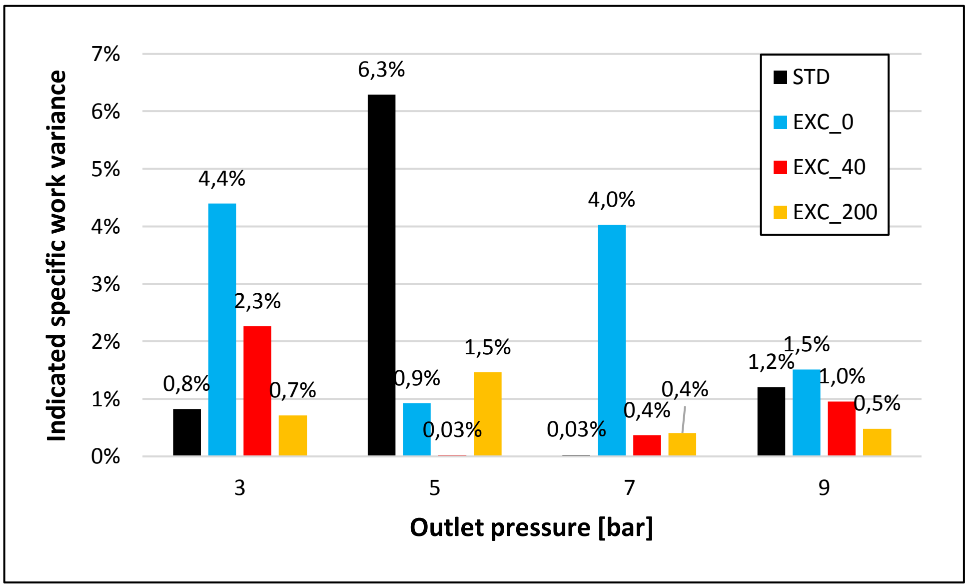

Figure 3.25 – Indicated specific work variance between repetitions of the same treatment at 1000 RPM

In general, the variance is under 3% and it exceeds 5% only once. So, for the sake of clarity, the next figures (figure 3.26, 3.27, 3.28, 3.29) show the average indicated diagram of each treatment (3 bar, 5 bar, 7 bar, 9 bar).

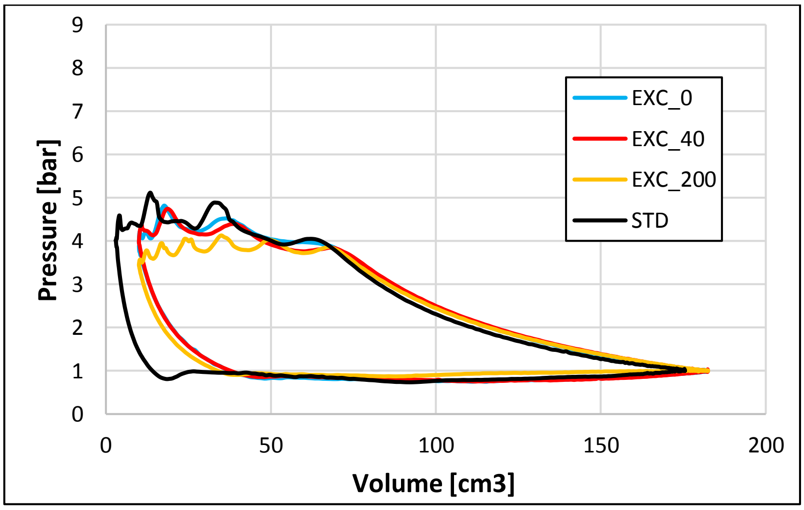

Figure 3.26 – Comparison of the indicated diagrams at 1000 RPM and 3 bar

The most evident common characteristic of these diagrams is the irregular discharge phase. This pattern is present at every speed and only in the discharge phase. A simple test was performed to identify the cause: a piece of rubber was used to partially block the discharge valve on the discharge ducts so that the stiffness and the dumper of the valve system was modified. The irregular pattern vanished, but of course the valve pressure losses were huge. It can be concluded that the pattern was caused by the discharge valve vibrations, and that it is part of the normal functioning of this compressor.

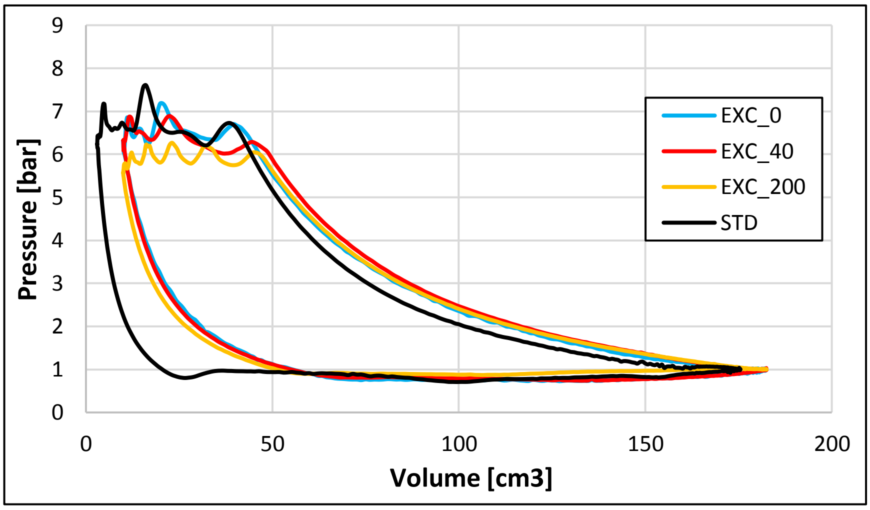

Figure 3.27 – Comparison of the indicated diagrams at 1000 RPM and 5 bar

These figures show the deleterious effect of the exchanger volume. The EXC configurations expansion phases end far more on the right than in the STD configuration, leading to a lower filling coefficient. The water refrigerating effect partially counter this effect due to an increased air density (see figure 3.14)

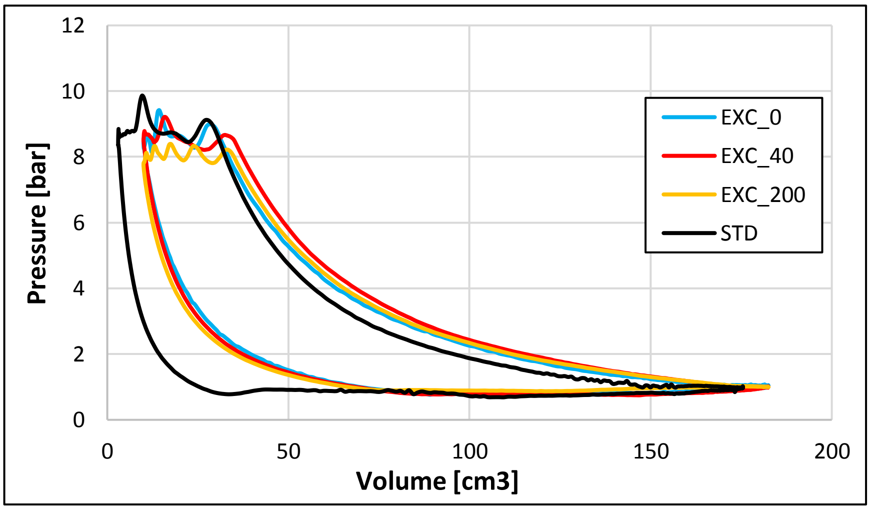

Figure 3.28 – Comparison of the indicated diagrams at 1000 RPM and 7 bar

The EXC configurations have very little differences among them, especially in the compression phase. This confirm that the water has a poor effect on the compressor work (as stated in the paragraphs 3.3.1 and 3.3.2), and then the advantages on the specific work are related to the effect on the air flow rate.

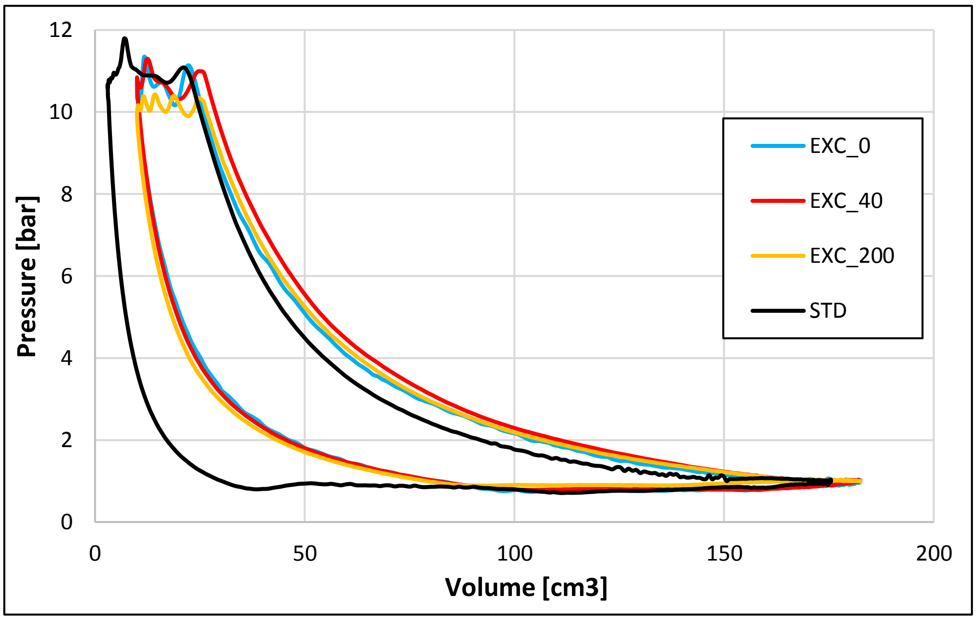

Figure 3.29 – Comparison of the indicated diagrams at 1000 RPM and 9 bar

The EXC configuration diagrams are off 7 cm^3 to the right due to the exchanger volume. As well, the compression phase starting point is further on the right than the STD compression phase starting point. Bear in mind that, in this case, the compression curves cannot be compared.

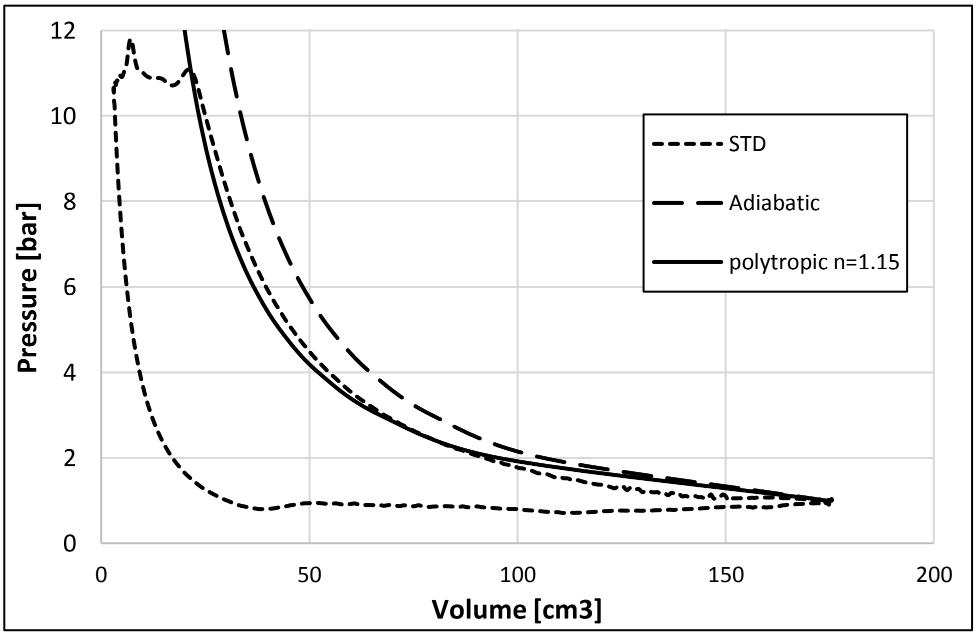

Figure 3.30 – Comparison between STD indicated diagram (at 1000 RPM and 9 bar) and ideal curves

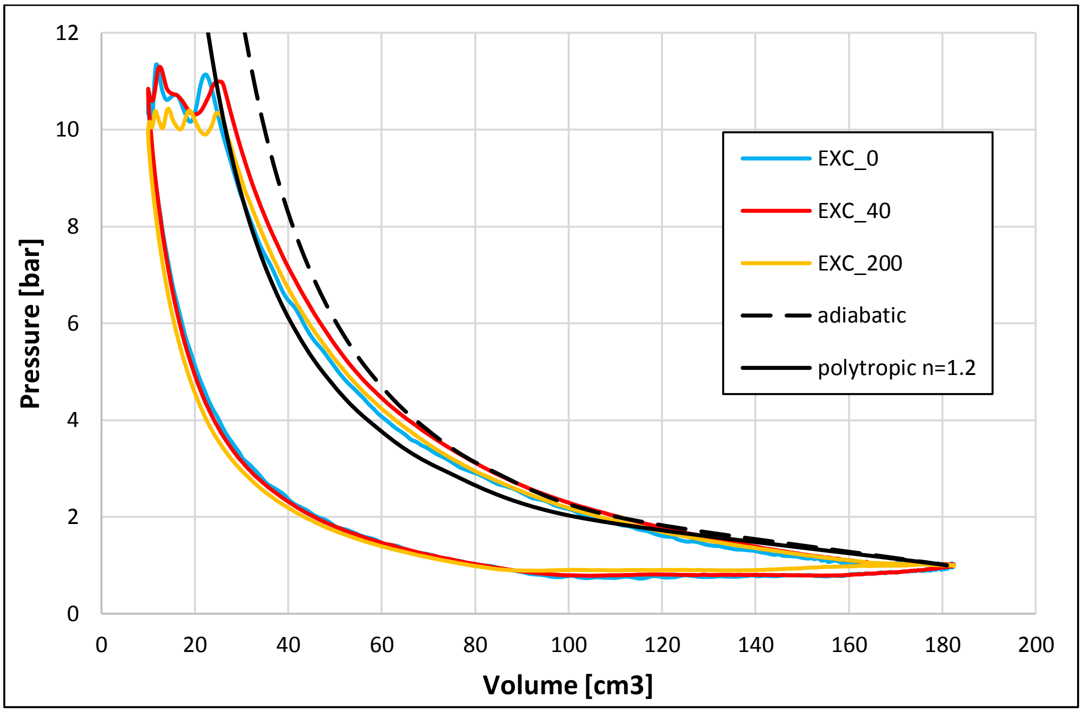

Figure 3.31 – Comparison between EXC indicated diagrams (at 1000 RPM and 9 bar) and ideal curves

Figures 3.30 and 3.31 shows the indicated diagram at 1000 RPM and 9 bar and compare them to ideal compression curves. It can be seen that the exchanger has no beneficial effect on the real compression polytropic coefficient, actually it has a slightly negative effect. As observed above (see figure 3.5) the standard compressor structure successfully dissipates the heat generated. The STD compressor heat dissipation is better than the EXC ones in the first part of the compression, when in the EXC configuration the temperature difference toward the cold fluid is still too low. This temperature difference is low because the entire machine has a low temperature. Moreover, a low air temperature at the beginning of the expansion phase implicate very low temperatures at the end of this phase and so lower temperatures at the beginning of the compression (see chapter 1). However, the differences between the compression curve in STD configuration and those in EXC configuration are shallow and has almost no effect on the global performances of the machine.

3.3.4 Focus on the exchanger

As shown in the previous paragraph, the polytropic exponent is poorly affected by the exchanger. On the other hand, the air outlet temperature is heavily lowered by it (see figures 3.7,3.9,3.11,3.23). This paragraph focuses on the exchanger performances.

Figure 3.32 shows the water temperature for every pressure ratio tested when the water flow rate is 40 l/h (EXC_40 configuration) or 200 l/h (EXC_200 configuration) at 1000 RPM.

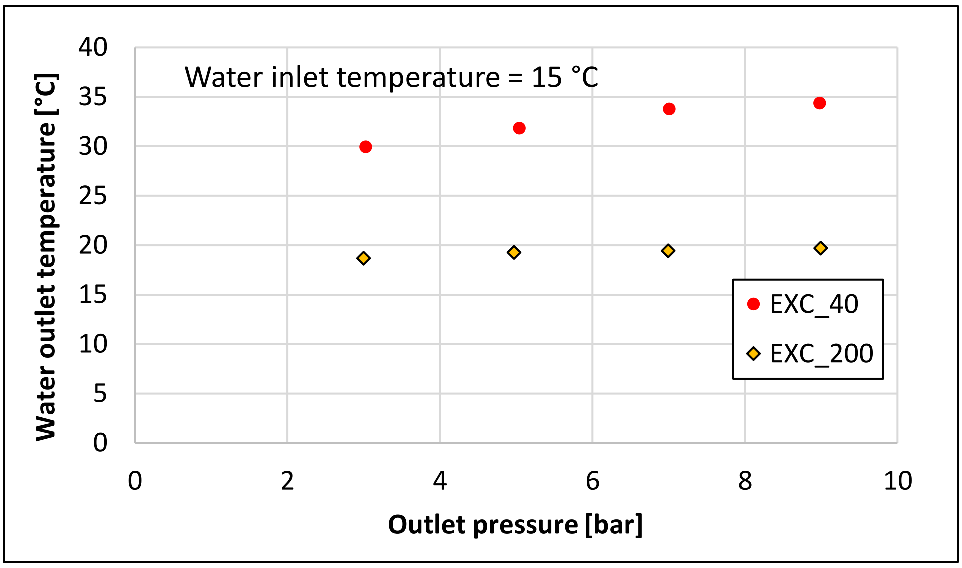

Figure 3.32 – Comparison of the exchanger water outlet temperature between EXC_40 and EXC_200 configuration

To calculate the heat absorbed by the water is nearly impossible in the case EXC_200, as the differences between the water inlet and outlet temperatures are heavily affected by the measure tolerance (a high-quality K type thermocouple has ha tolerance of 1.5 K. See also appendix 1).

To maximize the temperature differences, the configuration chosen for this analysis is the EXC_40 at 1000 RPM.

One of the most important quantities needed to characterize an exchanger is the efficiency, also mentioned in chapter 2 (see equation 2.1) and herein reported (equation 3.8).

$$\varepsilon_f = \frac{heat\ exchanged}{max\ heat\ available} = \frac{T_{air\_in} - T_{air\_out}}{T_{air\_in} - T_{water\_in}} = \frac{\dot{C}_{water}\left(T_{water\_in} - T_{water\_out}\right)}{\dot{C}_{air}\left(T_{air\_in} - T_{water\_in}\right)} \quad [3.8]$$

Where $\dot{C}_{water}$ and $\dot{C}_{air}$ are the thermal capacity rates of the streams of water and air (equation3.9).

$$\dot{C}_{water} = \dot{m}_{water} c_{water} \ ; \ \dot{C}_{air} = \dot{m}_{air} c_{p,air} \quad [3.9]$$

Where $\dot{m}$ is the mass flow rate, c is the specific heat, and c_p is the specific heat at constant pressure.

In this case, equation 3.8 is useless. In fact, the air inlet temperature (T_{air_in}) unknown as there is no sensor capable of measure the instantaneous temperature inside the cylinder, before the air goes through the exchanger.

Figure 3.33 shows the heat absorbed from the water (orange points), calculated from the experimental data through the numerator of equation 3.8 (last fraction). The absorbed power reaches 900 W at 9 bar. In chapter 2, two targets for the exchanger power absorption were defined (last pages of paragraph 2.7). The stricter of the two was calculated as the heat that must be released by the air to obtain an isothermal compression. At the time, the nominal compression ratio and the mass flow rate of the standard machine were used for the calculation. In figure 3.33, an adjusted power target is shown. This adjusted target is calculated using the actual compression ratio (as measured by the instantaneous pressure sensor in the compression chamber) and the mass flow rate measured for each pressure ratio (β) in EXC_40 configuration, as shown in equation 3.10.

$$Adjusted\ target = \left[\frac{\dot{m}_{air,\beta}}{2} R_{air} T_{in\_air,\beta} ln(\beta_{real})\right]_{EXC\_40} \qquad [3.10]$$

It may seem a bit unfair, as the heat absorbed refers to the isothermal transformation (the theoretical maximum heat that it could be absorbed during a compression). Nevertheless, the actual heat absorbed is significantly higher than the target.

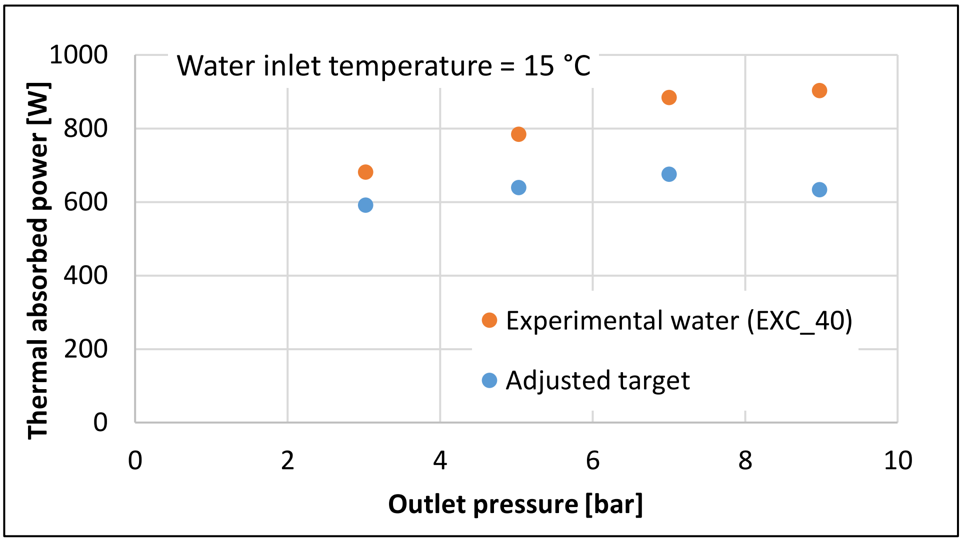

Figure 3.33 – Comparison between EXC_40 thermal absorbed power and the adjusted target

The exchanger absorbs more than the target. Figure 3.34 shows a comparison between the thermal absorbed power by the water and the ideal adiabatic enthalpic power for each pressure ratio. The ideal adiabatic power is also the subtracted heat rate needed to cool down the adiabatic compressed gas to the initial temperature via isobaric transformation. The adiabatic work is calculated using the actual maximum pressure reached in the compression chamber for each nominal pressure ratio and the measured mass flow rate.

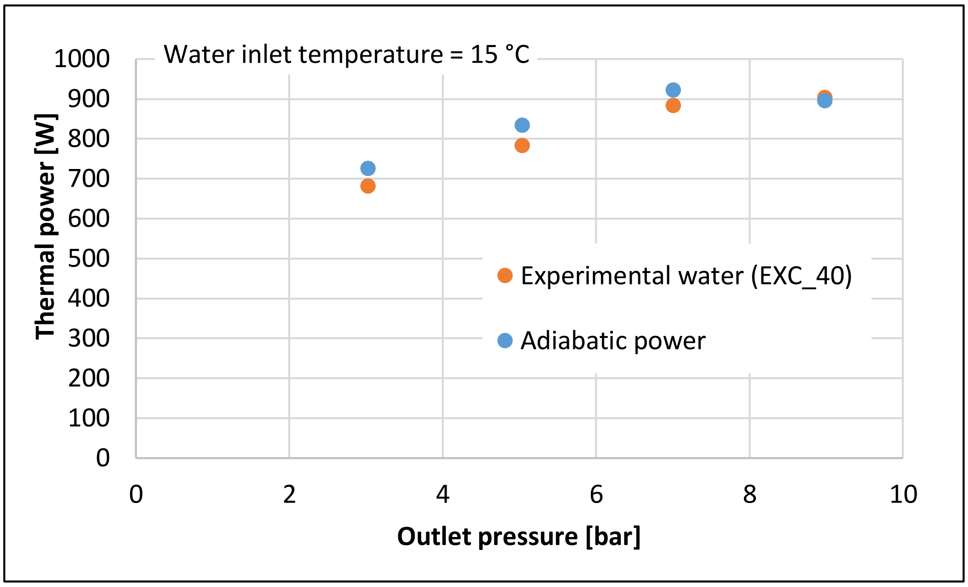

Figure 3.34 – Comparison between EXC_40 thermal absorbed power and the adiabatic power

Figure 3.34 suggest that most of the cooling is performed after the compression, during the discharge phase. On the other hand, the mean polytropic coefficient is smaller than 1.4: still some heat is absorbed during the compression. Moreover, the heat caused by the mechanical losses complicates the evaluation even more.

The measured thermal quantities are mean values. The actual absorbed heat rate is not constant throughout the compression phases. The air flow conditions inside the exchanger vary from very low velocities (when the valves are closed) to very high (the estimated Reynolds number fluctuates from less than 1000 to over 30000, see next chapter). It is reasonable that the convective exchange coefficient fluctuates over the phases. The valve closed phases will always suffer from too low heat exchange, or at least too low heat exchange to reach low mean polytropic exponents. Increasing the exchanging surface could be a possible solution. The question is how much more surface is needed and if it is technically possible to increase it to that extend.

In the next chapter a numerical simulation is used to estimate the instantaneous convective exchange coefficient.

4 Numerical Study

A numerical model was developed to try to overcome the limits of the test bench. The test bench is not capable of measure instantaneous temperatures or instantaneous exchanged thermal power. Moreover, it is impossible to perform sensitivity analysis on the test bench for parameters such as the exchanger volume or surface without new exchangers.

4.1 Model general description

The model was written using the commercial Siemens software Amesim. Amesim is based on the bond graph theory: every block of the simulation sketch is connected to others through bonds that represent a bidirectional exchange of energy. As Amesim can simulate multidomain systems, the energy involved could be mechanical, thermal, hydraulic/pneumatic, electric and so on. In Amesim, colours are linked to a type of energy and then to a specific library or a group of libraries. The red blocks are the only exceptions, as they do not treat energy, but they are mathematical/signal blocks.

Figure 4.1 shows the sketch of the compressor model. Six libraries are involved:

- Red: Signal/control library
- Green: Mechanical library
- Purple: Pneumatic library and Pneumatic component design library
- Light blue: Thermal pneumatic library
- Brown: Thermal library (for solid elements)

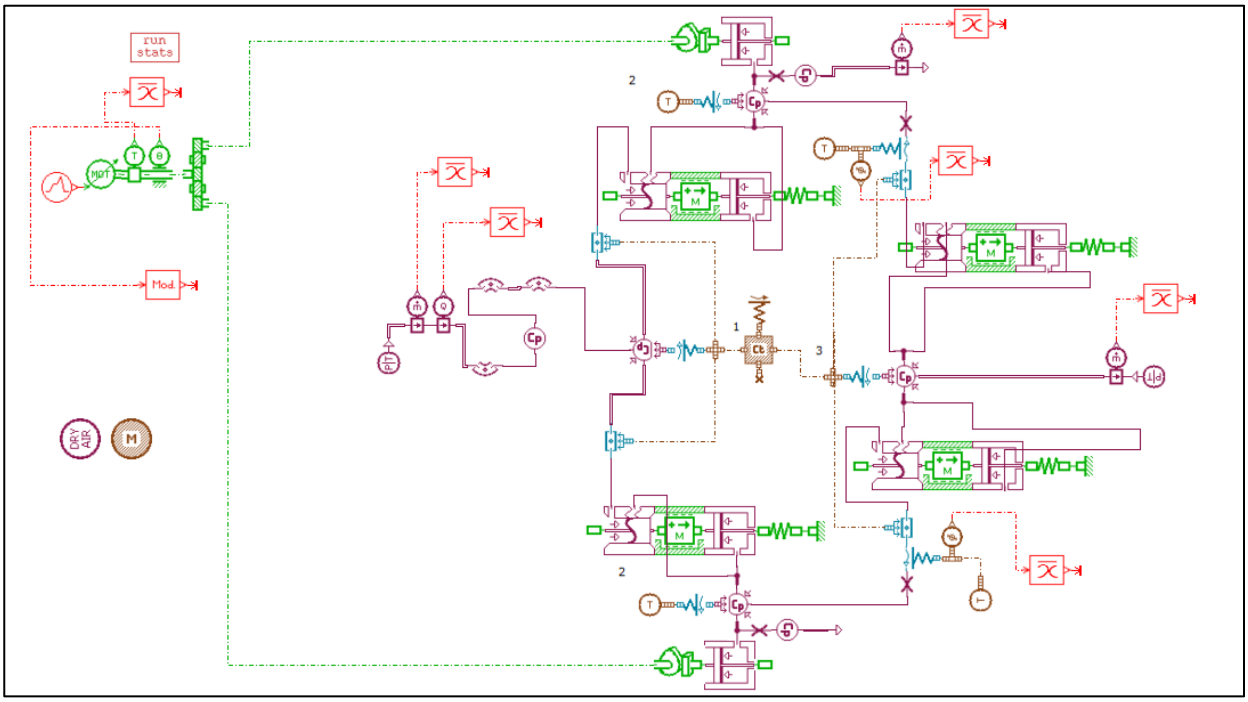

Figure 4.1 – Sketch of the AMESIM model of the compressor with MCHE

4.2 Model detailed description

In the figures below groups of blocks are shown. Each group represent a specific part of the test bench, such as the compressor, the valves, the exchanger and so on.

Figure 4.2 shows special blocks that have no bonds. These blocks affect the whole sketch, setting the properties of the fluids and the solids.

Figure 4.2 – Blocks setting the properties of the fluids and solid

The first block controls the gas properties, and the gas selected is dry air even though it may be a rough simplification. The latter controls the solid properties. The chosen metal is the aluminium, as the exchanger is made of this metal. The other parts of the compressor are made of steel or cast iron. Future improvements of the model may include more types of metal in the calculation.

The group in figure 4.3 is used to model both the inlet and the outlet compressor valves. It is a classic mass spring model (green blocks) linked to two chambers (purple blocks). The first purple block on the left (pneumatic spool) connect or interrupt the flow between the cylinder and the inlet/outlet duct (flow between port 1 and 2). The second block takes the pressure level from port 3. Both blocks have a parameter for the area on which the gas pressure operate.

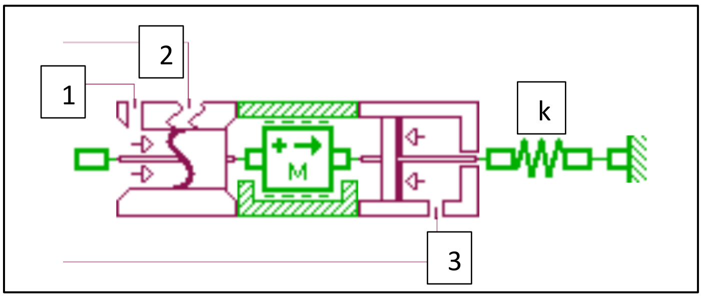

Figure 4.3 – Model sketch of the compressor valves

$$p_1A_1 - p_3A_3 = M\ddot{x} + k_e x \qquad [4.1]$$

Equation 4.1 is the classical mass-spring relationship, where M is the mass of the system and k_e is the elastic rate in [N/m].

The group showed in figure 4.4 represents one of the compressor cylinders. The group includes the crankshaft mechanism (green bigger block), that gives motion to the piston (purple block). The volume is computed and added to the volume chamber connected to a light blue block representing the thermal transmission through the cylinder walls. This chamber is connected to the inlet valve and the exchanger (not visible in figure). A collateral bond lead to the ambient through an orifice, a chamber and a flow rate indicator (it is not real, but only a calculation tool). This series represents the cylinder gas leakages.

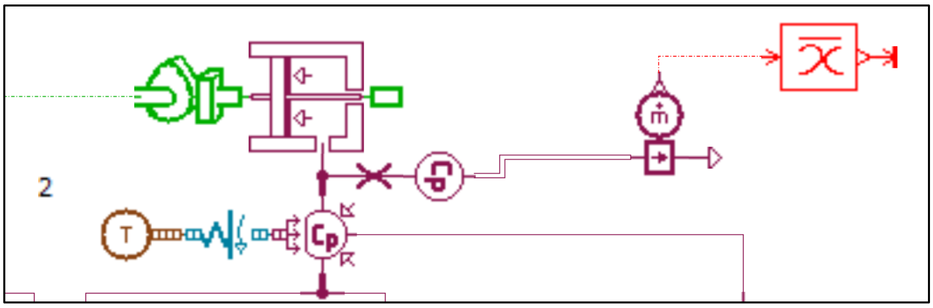

Figure 4.4 – Model sketch of the compressor cylinder

The crankshaft block has a bond on the left that gives it the angular displacement. Through a table the block converts the angular displacement to a linear displacement. The thermal transmission block (light blue) uses the Dittus Boelter correlation to calculate the Nusselt number (see equation 4.2) and then the heat transfer coefficient via equation 4.3. The brown block gives a constant wall temperature.

$$Nu = 0.023\, Pr^{0.33} Re^{0.8} \qquad [4.2]$$

$$h = Nu * \frac{\lambda_f}{D_h} \qquad [4.3]$$

Where Pr is the Prandtl number, Re is the Reynolds number, λ_f is the fluid thermal conductivity and D_h is the hydraulic diameter of the exchanger gas passages.

In figure 4.5 the electric motor group is shown. It is an ideal motor which velocity is set to 800 RPM. Two signal converters (one for the torque and one for the angular displacement) were added as development indicators. At last, the transmission block duplicates the bond. The information delivered to the two cylinders is the same, but the two crankshaft blocks have different tables so that the two pistons have a 180 degrees phase shift.

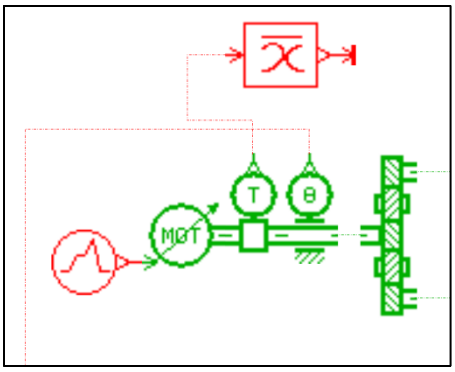

Figure 4.5 – Model sketch of the compressor cylinder

Figure 4.6 shows the air side exchanger group. It is made by three main blocks: from top to down there is a purple block and two light blue blocks. The brown block on the left side is simply a heat rate transducer. The purple block represents the narrowing from the cylinder cross section to the exchanger cross section. The first light blue block represents the exchanger. The heat rate functions are shown in equation 4.4 for laminar flow and equation 4.2 and 4.3 for turbulent flow.

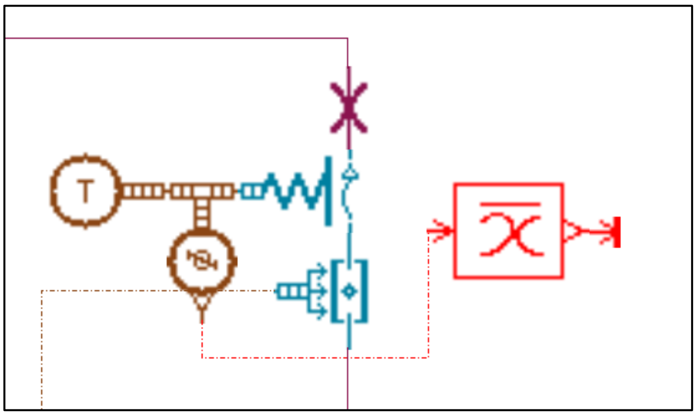

Figure 4.6 – Model sketch of the exchanger air side

$$h = 1.86 * \left(\frac{D}{X}\right)^{\frac{1}{3}} (Re\mathrm{Pr}\,)^{0.33} * \frac{\lambda_f}{D_h} \qquad [4.4]$$

Where Re is the Reynolds number, Pr is the Prandtl number, D is the hydraulic diameter of the gas passages and X is the length of the gas passages. The last block represents the passage through the valve plate and the thermal exchanges between the air and the valve plate itself. As the speed is relatively high it may be significant in the case without the exchanger or without water flowing in the exchanger.

The heat exchange relationships for the liquid side are the same of the other side: they are shown in equations 4.2 , 4.3 and 4.4. The last orange block is simply an infinite volume tank. The brown blocks provide thermal inertia (squared “Ct” block) and a convective thermal dissipation toward the ambient (block on the far right), whose equations are shown in equations 4.2 and 4.3 (the flow is considered turbulent).

Figure 4.7 shows the inlet duct group. The first block represents the ambient with air at predefined pressure and temperature. Then two transducers are placed. The first is a mass flow meter and the second is a volumetric flow meter. Then, three curves are placed and a tank, resembling the test bench, as in the inlet duct even small pressure drops could have a large impact on the flow rate.

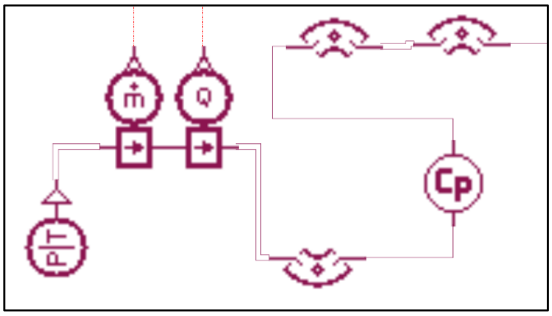

Figure 4.7 – Model sketch of the inlet duct

Figure 4.8 shows the group representing the cylinders head. The inlet and outlet chambers are pneumatically separated, but the heat exchange between them is possible through the light blue and brown blocks. The light blue blocks are the same of figure 4.6. The brown blocks represent the head thermal inertia (squared "Ct" block) and a convective dissipation block toward the ambient (placed on the brown block).

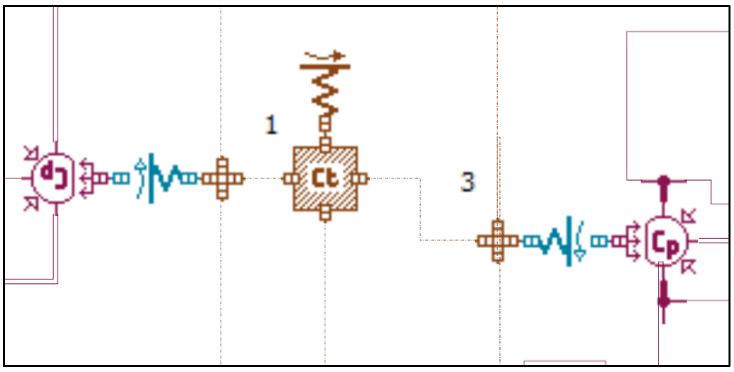

Figure 4.8 – Model sketch of the cylinders head

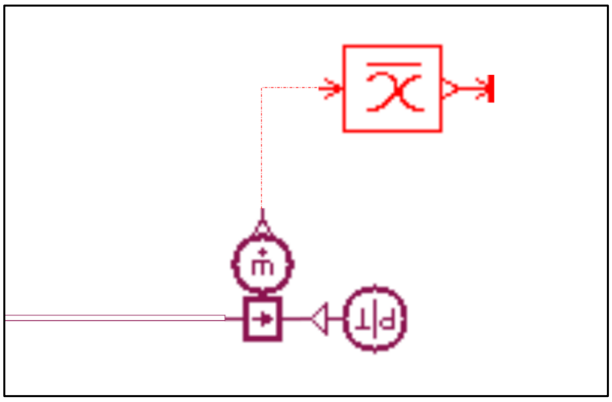

Figure 4.9 – Model sketch of the outlet duct

At last, figure 4.9 shows the outlet duct. It is a simple duct, with a mass flow rate transducer. The regulation valve is replaced with a pressure control (last purple block on the right).

4.3 Model calibration and settings

The model was calibrated on the 800 RPM test in EXC_40 configuration at 5 bar and 7 bar. Whenever possible, the inputs are the results of measurements on the real compressor. Some data were missing, such as the valves stiffness, the air leaks passages cross section, the cylinders inner walls temperatures. Moreover, the light blue block representing the thermal transmission through the cylinder walls cannot follow a dynamic behaviour in terms of internal air pressure and velocity. For that reasons, the model can be improved through future activities. Nevertheless, the accordance is satisfying for this work purpose, that is to have indications on the heat exchanging mechanism.

Table 15- Main model inputs for both the calibration and the various simulations.

	EXC_0	EXC_40
Cylinder bore	60.5 mm	
Cylinder stroke	60 mm	
Shaft speed	800 RPM	
Dead volume	3000 mm^3	
Cylinder wall surface	11000 mm^2	
Exchanger volume	7000 mm^3	
Exchanger surface	20800 mm^2+30%	
Exchanger wall temperature	67 °C (3 bar)| 83 °C (5 bar) 89 °C (5 bar)| 95 °C (9 bar)	30 °C
Inlet pressure	1 bar	
Inlet temperature	20 °C	
Cylinder wall temperature	67 °C (3 bar)| 83 °C (5 bar) 89 °C (5 bar)| 95 °C (9 bar)	30 °C
Head temperature	67 °C (3 bar)| 83 °C (5 bar) 89 °C (5 bar)| 95 °C (9 bar)	30 °C

As a first attempt, the temperatures were set at the external exchanger temperature. These data were acquired during the experimental runs through a laser thermometer (see appendix B).

The simulated time interval between each calculated point (print interval) was set to 0.001 seconds.

All the other parameters were set through a calibration process. The target data used were the inlet air flow rate and the indicated diagrams at 5 and 7 bar of delivery pressure were used).

Figure 4.10 shows the comparison between the experimental indicated diagrams and the calculated ones. Numerical diagrams show a satisfactory level of accuracy, except that the discharge valves oscillations were not simulated.

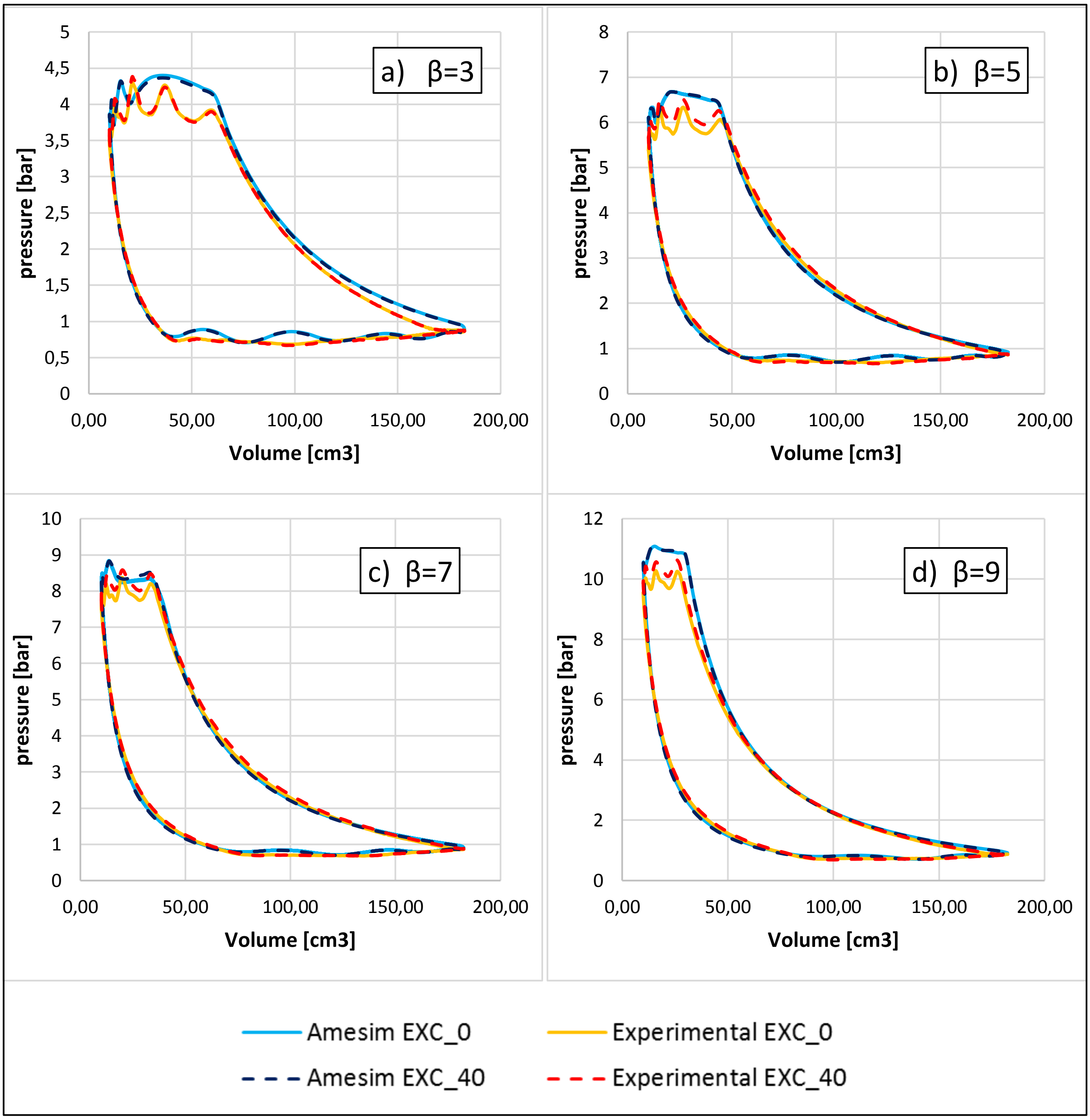

Figure 4.10 – Comparison between experimental and simulated indicated diagrams

The compression phase has a nearly perfect match. The expansion phase is also perfectly simulated in every condition. More effort is needed to perfectly match the delivery phase, nevertheless the average valves losses are satisfying.

Figure 4.11 shows the comparison between the experimental and the calculated air flow rate. The dotted lines are linear regressions of the experimental data.

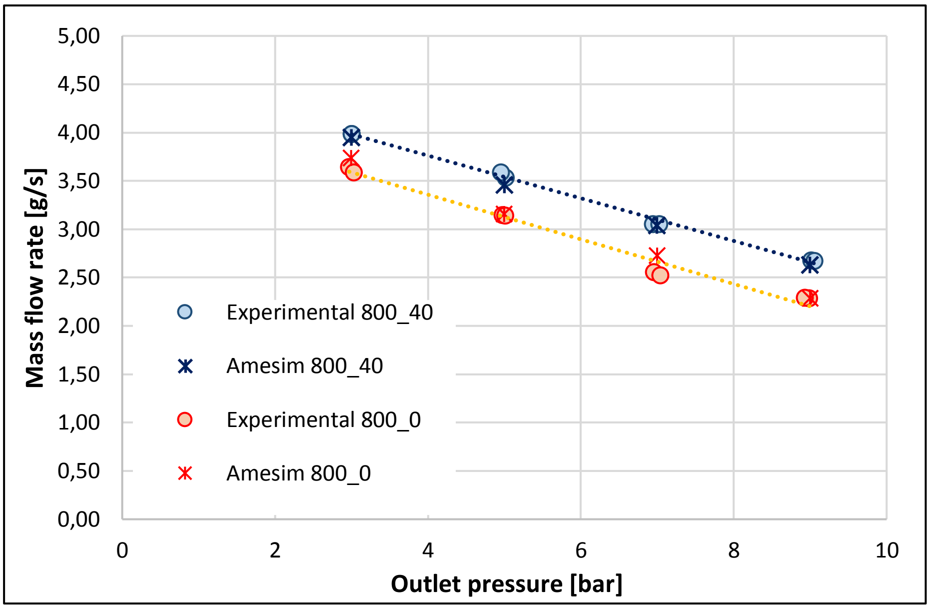

Figure 4.11 – comparison between the experimental and the calculated air flow rate

The experimental and simulated values lay on very similar lines. The average simulated air flow rate of each case (EXC_0 or EXC_40) depends on the inlet valve block calibration: the spring stiffness and the correct function between the flow area and the spring displacement were the main parameters of this block.

The slope of the lines where lays the simulated values also depends on the gas leakages. The leakages also affect the slope of the expansion phase on the pV diagram.

The difference between the EXC_0 and EXC_40 simulated air flow rate is caused by the cylinders head temperature, as no other parameter than the temperature inputs changed between simulations at the same pressure level. This confirms part of the conclusions of the previous chapter. The cooling has a secondary effect on the mass flow rate. Moreover, as the pV diagrams do not change between the EXC_0 and the EXC_40 series, that effect is the only cause for the specific work changing (see paragraph 3.3).

4.4 Model results

The model was used to extrapolate result and data that cannot be measured. Figure 4.13 refers to the simulation of the EXC_40 configuration at a discharge pressure of 9. It shows the instantaneous Reynolds number inside the exchanger using a Re-V diagram. The Reynolds number varies from values very close to zero to values over twenty thousand. So, the y-axis has logarithmic scale.

The points naming refers to figure 4.12: the compression phase goes form point 1 to point 2, the discharge phase from point 2 to point 3, the expansion phase from point 3 to 4 and the intake phase from point 4 to 1.

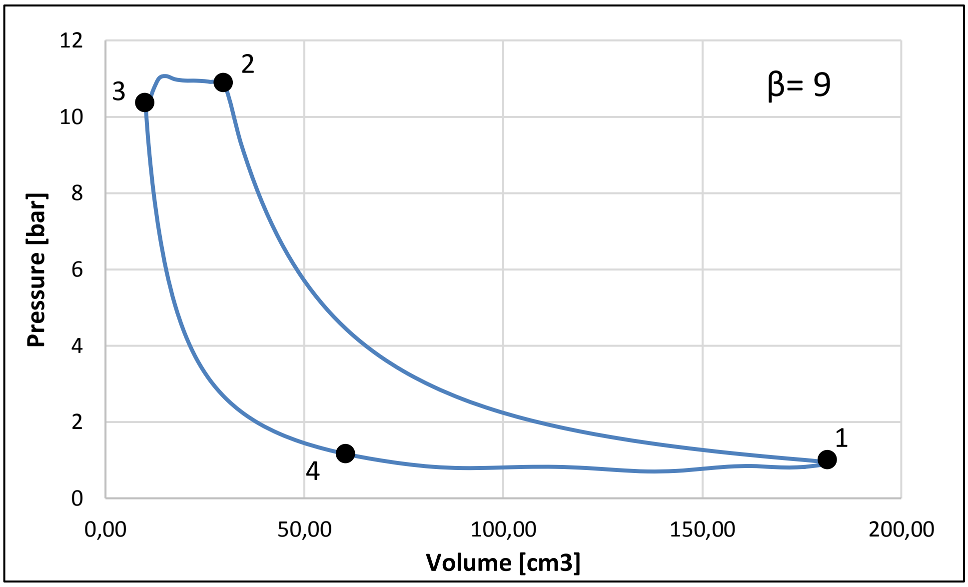

Figure 4.12 – Simulated indicated diagram at 9 bar and EXC_40 configuration

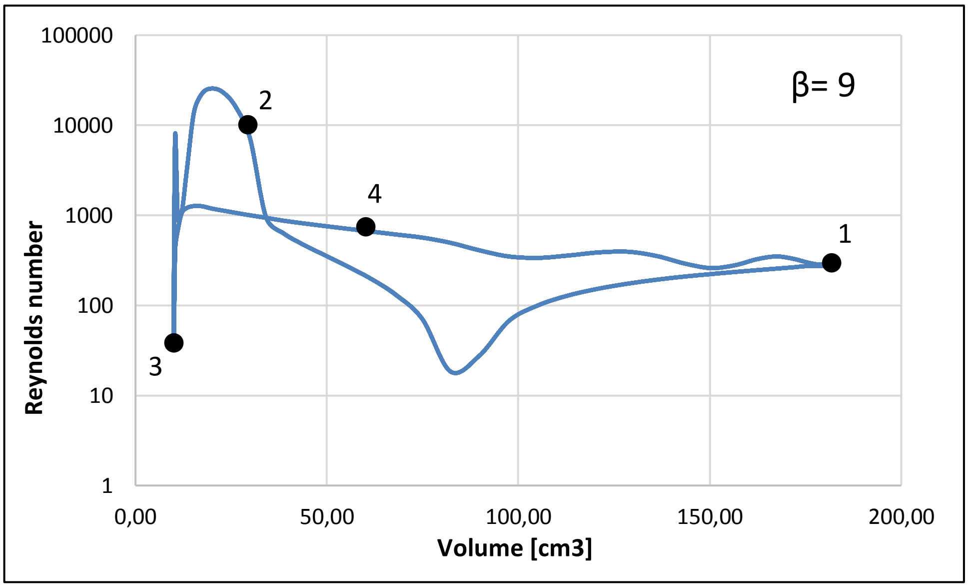

Figure 4.13 – Simulated instantaneous Reynolds number at 9 bar and EXC_40 configuration

This figure shows that during most the compression phase (the first part) the Reynolds number is low. This is reasonable, as both the gas density and speed are low as well. During most of the time, the flow inside the exchanger is laminar, or, at most, transitional.

The other cases are similar, such as the 5 bar shown in figure 4.14.

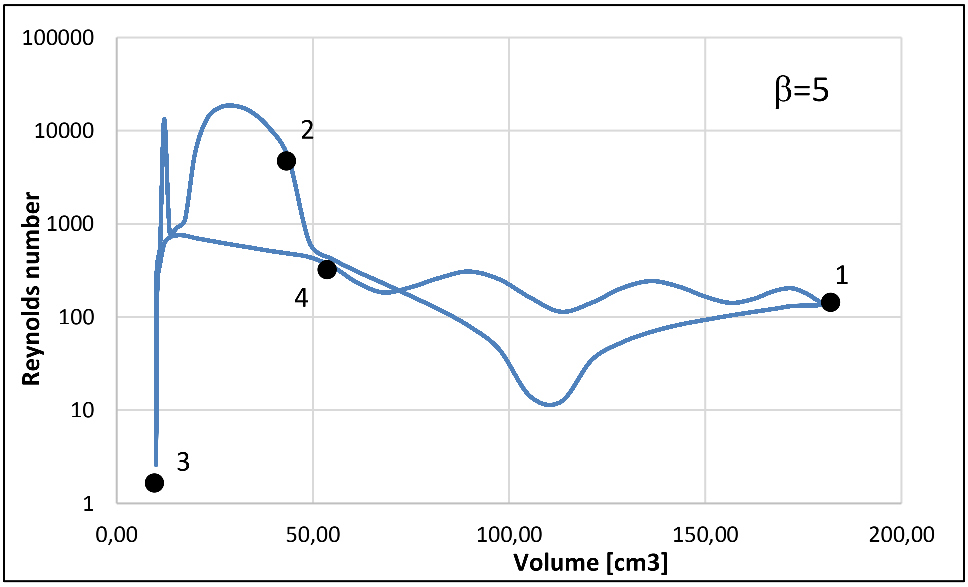

Figure 4.14 – Simulated instantaneous Reynolds number at 5 bar and EXC_40 configuration

This pattern affects the convective transfer coefficient (h). Figure 4.15 shows the instantaneous convective transfer coefficient inside the exchanger using a h_c-V diagram.

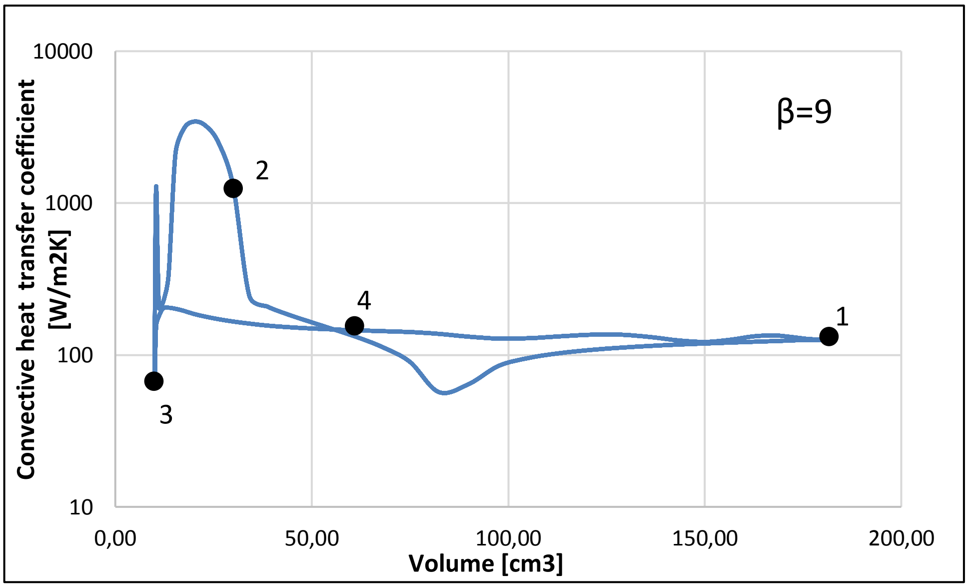

Figure 4.15 – Simulated instantaneous convective heat transfer coefficient at 9 bar and EXC_40 configuration

The heat transfer rate follows a similar pattern (figure 4.16). These figures explain the cause of the little effect of the cooling on the indicated diagram. The gas speed is too low; thus, the heat transfer coefficient is insufficient to achieve very low polytropic exponents.

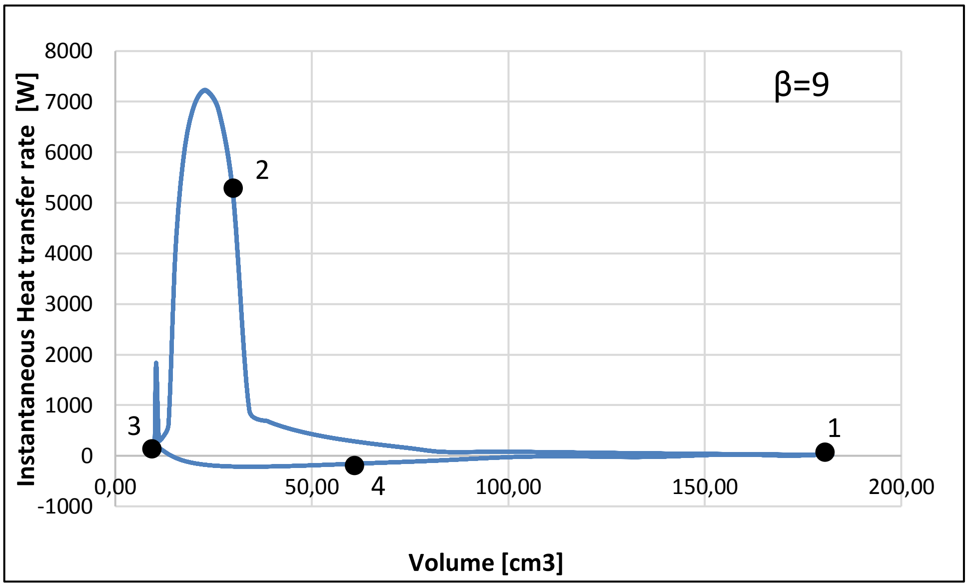

Figure 4.16 – Simulated instantaneous heat transfer rate at 9 bar and EXC_40 configuration

The next chapter illustrates a new idea to overcome this limit. The aim is to give the gas some speed during the compression phase.

5 A new proposed solution

In the last chapter some simulation results were shown. Those results clarified that the exchanger has excellent performance when the air has some speed and awful performance when it has not. So, in the compression phase, with closed valves, the exchanger performance is not satisfying. In this paragraph an idea is developed. The aim is to give speed during the compression phase. Herein, the idea is developed at theoretical level.

5.1 Addition by subtraction

Concepts like "addition by subtraction" are common in the sport culture. The meaning is that sometimes a very talented player does not fit the team composition, and, moreover, his playing style may disrupt the team playing principles; so, whenever this very talented player cannot play or whenever this player goes away, the team performs better.

Consider a multistage reciprocating compressor (figure 5.1).

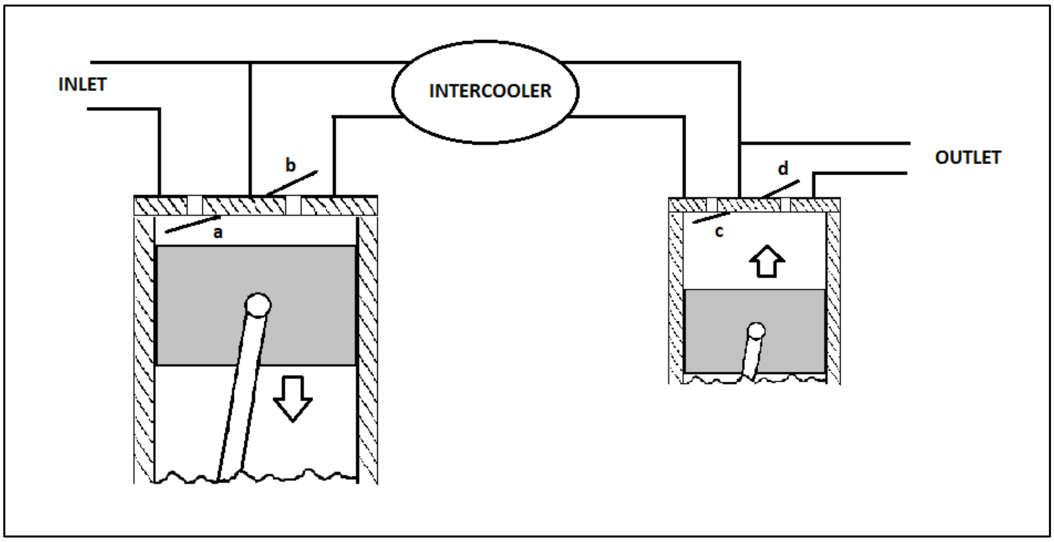

Figure 5.1 – Outline of a multistage compressor

It consists of two reciprocating machines in series: the first is bigger than the latter. Between them there is an intercooler. The first compressor delivers its compressed gas into the intercooler and the second compressors intakes from the exchanger. In general, the pistons may be in phase or not. In this case the pistons are exactly 180° out of phase. The valves are automatic. The first compressor intake valve is called "a", the first compressor discharge valve is called "b", the second compressor intake valve is called "c" and the second compressor discharge valve is called "d".

The idea is to eliminate one valve: the "b" valve or the "c" valve. In the first case the intercooler is part of the first machine, in the latter the intercooler is part of the second. Either ways, when the first piston tries to compress the gas, the second piston goes from the top dead centre to the bottom dead centre. Meanwhile, the valve between the two compressors is open and the gas is pushed from the first cylinder to the second while being compressed because the second cylinder is smaller than the first one.

So, the gas was given some speed while being compressed. The intercooler must have a very small volume because it is dead volume: if the eliminated valve is the valve “c”, the exchanger volume is part of the first machine dead volume, otherwise it is part of the second machine dead volume. So, the intercooler is ideally replaced with a Micro Channel Heat Exchanger. Different Outlines of this modified machine are shown in figures 5.6 and 5.7b.

The dead volumes make this new series of machine more complex than may be expected. In the next paragraph a detailed theoretical analysis clarified the phases successions and the differences between eliminating the valve “b” or “c”.

5.2 Theoretical study: overview of the modified multistage

In the following figures, the idea pV diagrams of the two cylinders are represented on the same plane. On the x-axis the sum of the volumes of the two cylinders are represented. A second y axis is present to separate the two cylinders volumes. In figure 5.2 these two diagrams are shown. The red curves are the first cylinder pV diagram and the blue curves are the second cylinder pV diagram.

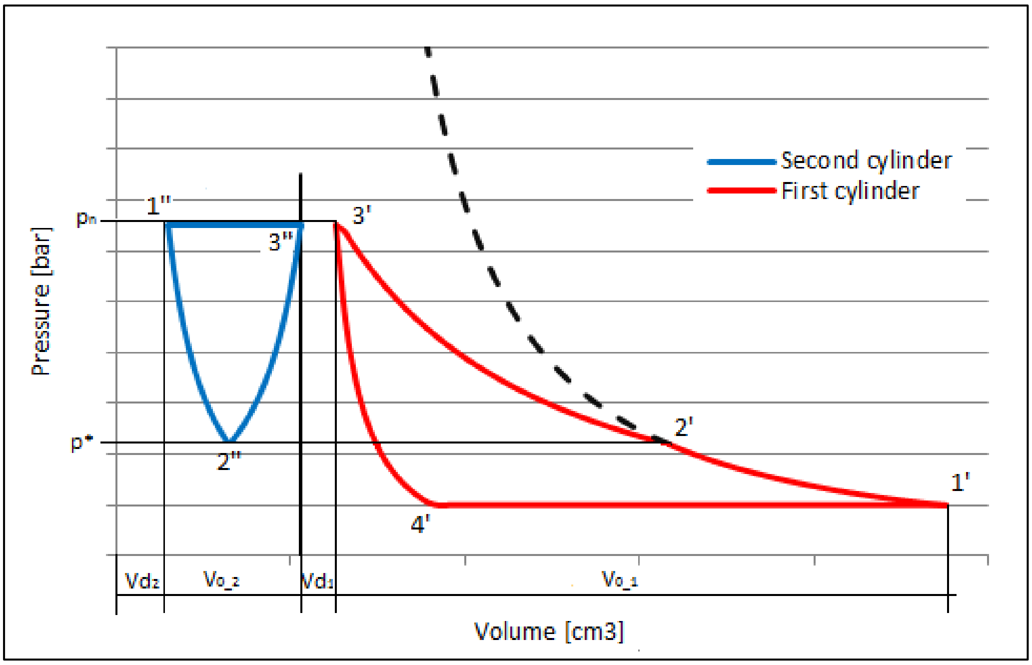

Figure 5.2 – Ideal indicated diagram of the modified machine: outlet pressure equal to p_n

In figure 5.2, Vd_2 is the dead volume of the second cylinder, V_{0_2} is the second cylinder cubic capacity, Vd_1 is the dead volume of the first cylinder and V_{0_1} is the first cylinder cubic capacity.

The points with a single quote mark refer to the first cylinder, the ones with double quote marks refer to the second cylinder. Point 1 represent the state when the first piston is at the bottom dead centre and the second is at the top dead centre. The valve between the two cylinders is closed until the pressures in the cylinders is equal. So, in the first cylinder there is a compression of the intake gas, while in the second cylinder there is an expansion of the gas trapped into the dead volume (Vd_2). In point 2, the two pressures are the same (p*) and the valve between the cylinders opens. The second piston is going towards the bottom dead centre, but the mass of gas coming from the first cylinder is enough to increase the pressure. Actually, in this phase the two cylinders and the exchanger are the same machine. So, point 2' is a cusp: the black dashed curve is the extension of the 1'-2' curve. As the volume is now much more, the shape of the compression curve is modified. The total volume that traps the gas is reducing itself and then the gas is compressed until the pressure equals the outlet pipe pressure and valve "d" opens. In the case represented in figure 5.2, the valve "d" opens exactly when the dead centre (top dead centre for the first piston and bottom dead centre for the latter) is reached, and this point is marked as point 3. This is an exceptional case but also the simplest case. The pressure needed in the outlet pipe to obtain this case is not simple to calculate. More details will be added in the next paragraphs. However, this pressure value is near the pressure ratio obtained from the volume ratio (equation 5.1).

$$\frac{p_n}{p_{1'}} \approx \left(\frac{V_{0\_1}}{V_{0\_2}}\right)^m \qquad [5.1]$$

Where m is the polytropic exponent. After point 3, the first piston starts moving towards the bottom dead centre and the valve between the cylinders closes. While in the first cylinders the expansion and intake phases (3'-4' and 4'-1') take place, the second piston goes from the bottom to the top dead centre, discharging (3''-1'').

In case the outlet pressure is higher than p_n the diagram is modified as in figure 5.3.

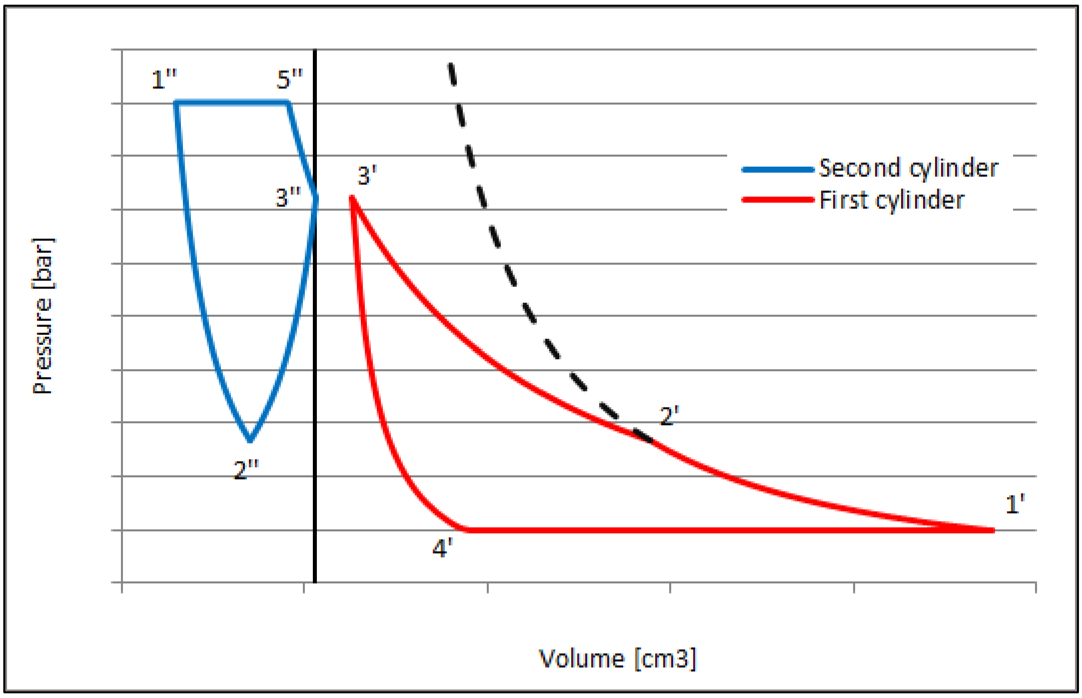

Figure 5.3 – Ideal indicated diagram of the modified machine: outlet pressure higher than p_n

The phases succession is the same except that reached point 3 the “d” valve does not open. However, the valve between the cylinders closes and the expansion phase starts in the first cylinder. The second piston starts going towards the top dead centre compressing the gas until the “d” valve opens (3’’-5’’). This point is named 5’’ instead of 4’’ because point 4’ and 5’’ has no simultaneity. Whether point 4’ occur before point 5’’ or not depends on the dead volumes capacity and the actual outlet pressure.

On the other hand, if the outlet pressure is lower than p_n, then the diagrams are modified as in figure 5.4.

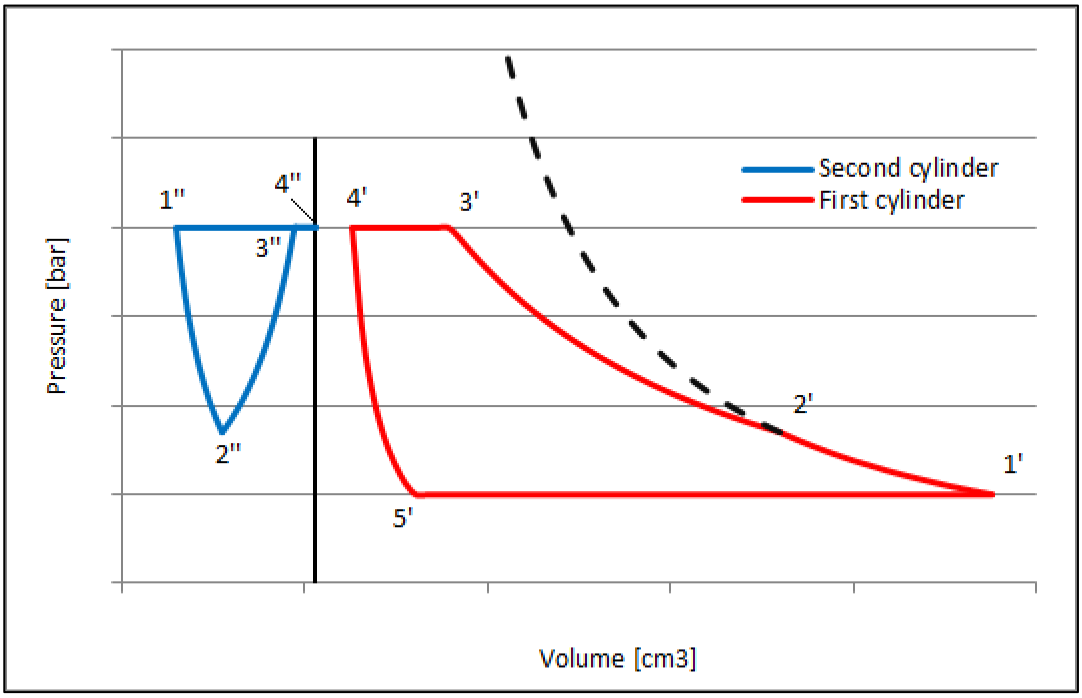

Figure 5.4 – Ideal indicated diagram of the modified machine: outlet pressure lower than p_n

In this case, the “d” valve opens before the dead centre (point 3). The pressure is kept constant by the discharge volume and the gas starts to be discharged through the valve “d” (3-4). Once the dead centre is reached the valve between the cylinder closes, and the first cylinder behave as a normal compressor. The second piston starts going towards the top dead centre discharging the gas through the “d” valve (4’’-1’’).

5.3 Theoretical study: in-depth analysis

In this paragraph the analytical equations of the curves shown in the previous paragraph are illustrated. All the equations refer to figure 5.5 and figure 5.6.

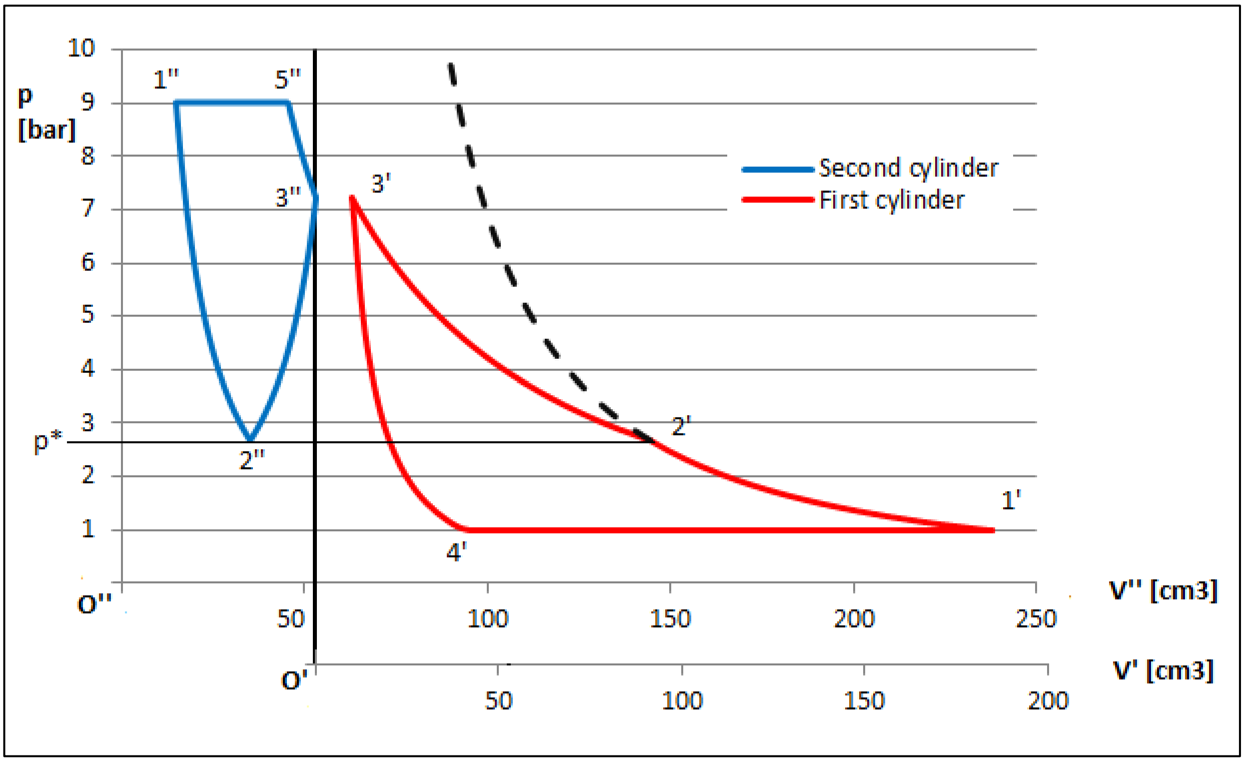

Figure 5.5 – Ideal indicated diagram of the modified machine with two volume axes.

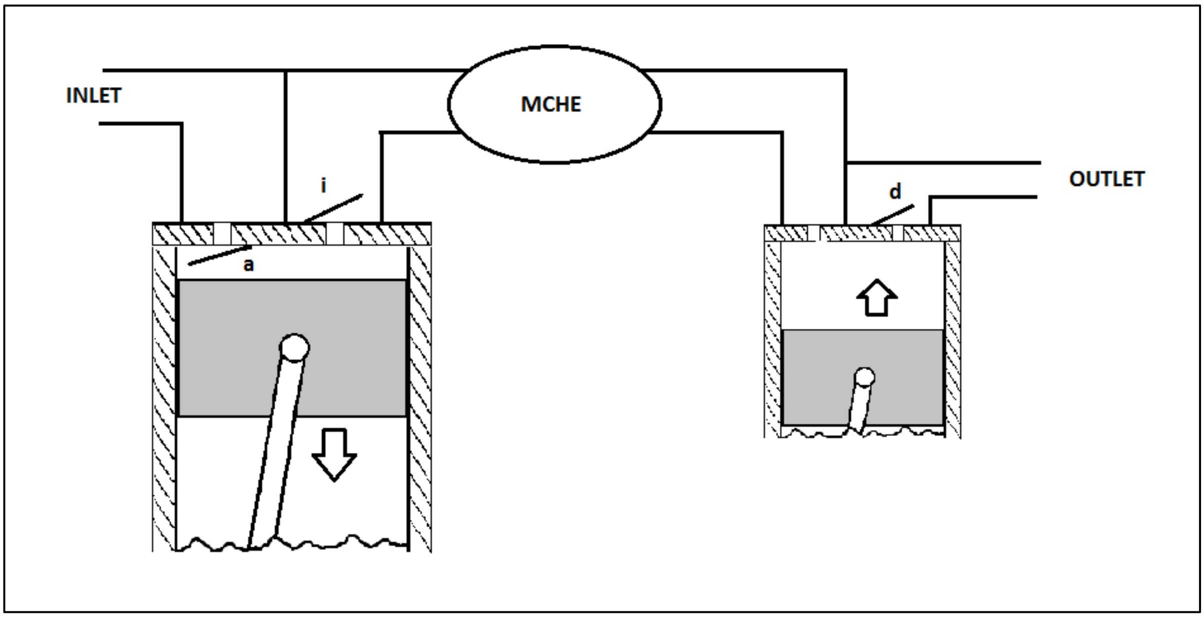

Figure 5.6 – Outline of the modified machine without the "c" valve

In figure 5.6 the valve c was eliminated, and the valve between the two cylinders is named “i”. In general, this valve could be placed before the MCHE (as in figure) or after. The differences between these two configurations will be illustrated in the next paragraph (5.3), but they do not affect the analysis of this paragraph.

The compression 1’-2’ and the expansion 1’’-2’’ are supposed to be adiabatic, as the exchanger should have a low efficiency because of the low speed of the gas. So, the compression 1’-2’ curve is an adiabatic curve on the pO’V’ plane, and expansion 1’’-2’’ is an adiabatic curve on the pO’’V’’ plane.

The first problem is the determination of p_2. Given the pressures of points 1’’ and 1’, and given that the volume of the two cylinders is have a fixed relationship due to the pistons mechanism, the solving system of equations is shown below.

$$p_2 V_{2\prime}^k = p_{1\prime} V_{1\prime}^k \quad [5.2]$$

$$p_2 V_{2\prime\prime}^k = p_{1\prime\prime} V_{1\prime\prime}^k \quad [5.3]$$

$$V'' = f(V') \quad [5.4]$$

Where V’ is the generic volume trapped in the first cylinder, V’’ the generic volume trapped in the second cylinder, $V_{1'}$ and $V_{2'}$ are respectively the volume of points 1’ and 2’ in the plane pO’V’ , $V_{1''}$ and $V_{2''}$ are respectively the volume of points 1’’ and 2’’ in the plane pO’’V’’, $p_{1'}$ and $p_{1''}$ are respectively the pressures of points 1’ and 1’’, and p_2 is the pressure needed for the opening of the “i” valve.

Once p2 is reached, the “i” valve opens and the volumes of the two cylinders are connected. The transformation is polytropic with an exponent “m” (equation 5.5). The exponent value depends on the actual efficiency of the exchanger.

$$pV_{tot}^m = p(V' + V'')^m = constant = p_2(V_{2\prime} + V_{2\prime\prime})^m \quad [5.5]$$

Where V’ is the generic volume trapped in the first cylinder, V’’ the generic volume trapped in the second cylinder (the dead volumes are included). To obtain the curves 2’-3’ and 2’’-3’’ equation 5.4 is needed. Equation 5.5 is transformed into equations 5.6 and 5.7.

$$p = \frac{constant}{(V' + f(V'))^m} \quad [5.6]$$

$$p = \frac{constant}{(f^{-1}(V'') + V'')^m} \quad [5.7]$$

Equation 5.6 refers to the pO'V' plane and equation 5.7 to the pO''V'' plane, in the sense that the independent variables (respectively V' and V'') are on those planes. A graphical representation of equation 5.5 should use the pO''V'' plane that can consider the sum of the volumes.

After point 3, the "i" valve closes, and the two cylinders transformations are the same of a classical reciprocating compressor. As the compression 1'-2' and the expansion 1''-2'', all the other phases are considered adiabatic.

It is possible to calculate the work consumption of this ideal machine as the sum of the areas of the diagrams (for example in figure 5.5). However, the more the function in equation 5.4 is complex, the more equations 5.6 and 5.7 are difficult to integrate. The simplest way to calculate the work consumption for the transformation 2-3 (as a whole) is to use equation 5.5. Regardless of how the volumes in brackets changes, overall it is a classical polytropic equation that links the total volume and the pressure. So, its integral is known (equation 5.8).

$$W_{2-3} = \frac{1}{m-1} p_2 (V_{2'} + V_{2''}) \left(\left(\frac{p_3}{p_2} \right)^{\frac{m-1}{m}} + 1 \right) \qquad [5.8]$$

Where W_{2-3} is the work related to the transformation 2-3. The other curves are classical curves when referred to their own plane (pO'V' or pO''V''), so their integrals are known.

It is also possible to calculate the ideal mass of gas compressed per round using equation 5.9.

$$m = \rho_1 (V_{1'} - V_{4'}) \qquad [5.9]$$

Where ρ_1 is the gas density at the inlet thermodynamic state; $V_{4'}$ is the volume full of gas trapped in the first cylinder at the end of the expansion (3'-4'); $V_{1'}$ is the volume full of gas trapped in the first cylinder at the end of the intake phase (4'-1'). The quantity calculated via equation 5.9 does not consider both leakages and heat exchange (aside that in the exchanger during the compression 2-3).

5.4 Theoretical study: results

This paragraph shows some results based on the pervious paragraph analysis. The main aim is to clarify the effect of the dead volume on the machine performance. The dead volume consists of the exchanger volume, the volume of the ducts between the two cylinders, the two cylinders original dead volume.

These results refer to the case shown in figure 5.2 (herein copied in figure 5.7a): the delivery pressure and the pressure reached in point 3 are the same. On the other hand, the Outline is modified as in figure 5.7b: the exchanger is split into two exchangers and the “I” valve is placed between them. In general, the two exchangers are different, and one of them could have no volume at all; these two cases (exchanger 1 suppressed and exchanger 2 supressed) are equivalent to the ones seen in the previous paragraphs, respectively the one with valve “c” suppressed and the one with valve “b” suppressed. This Outline was adopted because there are some differences on the machine performance depending on the “position” of the dead volume (before or after the “i” valve).

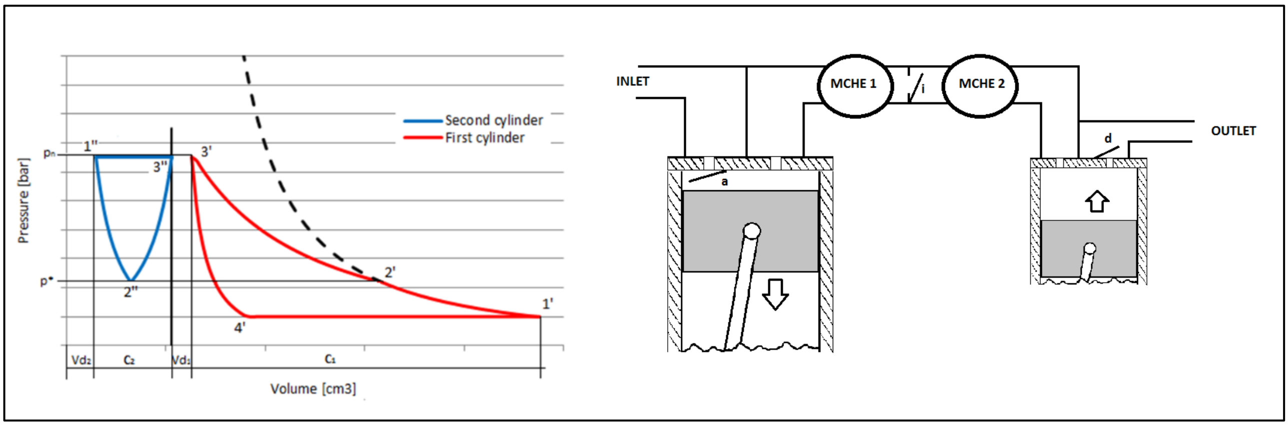

Figure 5.7a – Copy of figure 5.2
Figure 5.7b – Outline of the modified machine with two MCHE

The results shown in this paragraph are obtained presuming that the two cylinders are on the same crankshaft and simplifying the piston motion equation into a perfect sinusoid. Equation 5.4 is modified as in equation 5.10 and 5.11.

$$V' = V_{3'} + \frac{V_{0\_1}}{2}(1+\cos\alpha) \qquad [5.10]$$

$$V'' = V_{1''} + \frac{V_{0\_2}}{2}(1-\cos\alpha) \qquad [5.10]$$

Together with equations 5.2 and 5.3 they give equation 5.11.

$$\cos\alpha_2 = \frac{\dfrac{2V_{1''}+V_{0\_2}}{2p_{1''}^{1/k}V_{1''}} - \dfrac{2V_{3'}+V_{0\_1}}{2p_{1'}^{1/k}V_{1'}}}{\dfrac{V_{0\_1}}{2p_{1'}^{1/k}V_{1'}} - \dfrac{V_{0\_2}}{2p_{1''}^{1/k}V_{1''}}} \qquad [5.11]$$

And thus equation 5.12 or 5.13 (they are equivalent).

$$p_2 = \frac{p_{1'} V_{1'}^k}{V_{3'} + \frac{V_{0\_1}}{2}(1+\cos\alpha_2)} \qquad [5.12]$$

$$p_2 = \frac{p_{1''} V_{1''}^k}{V_{1''} + \frac{V_{0\_2}}{2}(1-\cos\alpha_2)} \qquad [5.13]$$

So, p_2 depends on 6 parameters: $p_{1'}$, $p_{1''}$, $V_{1'}$, $V_{1''}$, $V_{3'}$, $V_{3''}$ (V_{0_1} and V_{0_2} are respectively $V_{1'}$ - $V_{3'}$ and $V_{3''}$ - $V_{1''}$). Moreover, $p_{1''}$ depends also from p_2 and m (exponent of the polytropic 2-3). This relationship is shown in equation 5.14.

$$p_{1''} = p_3 = \frac{p_2 (V_{2'} + V_{2''})^m}{(V_{3'} + V_{3''})^m} \qquad [5.14]$$

There are two possibilities: the first one is to arbitrarily set the $p_{1''}$ and then calculate everything else. However, this means to discard equation 5.14, then the actual case could be anyone of those illustrated in paragraph 5.2. The other possibility is to solve the problem via successive approximations. The values of $p_{1'}$, V_{0_1}, V_{0_2} and m were fixed to obtain the following figures. Also, the sum of $V_{1''}$ and $V_{3'}$ was fixed, while the $p_{1''}$ is determined via successive approximations. In figure 5.8 the value of p_2 , the intake of gas per round, and the adiabatic efficiency as function of the dead volumes before and after the "i" valve ($V_{1''}$ and $V_{3'}$) are shown. In figure 5.9 the value of p_3 as function of $V_{1''}$ and $V_{3'}$ is shown. In table 14 are collected the parameters values used to obtain these figures.

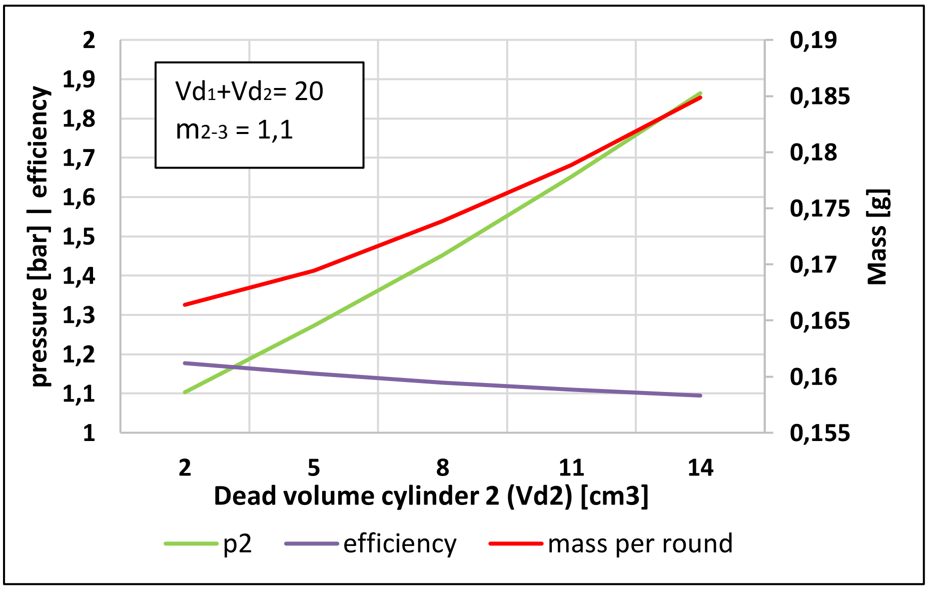

Figure 5.8 – Calculated values of p_2*, adiabatic efficiency and intake of gas per round*

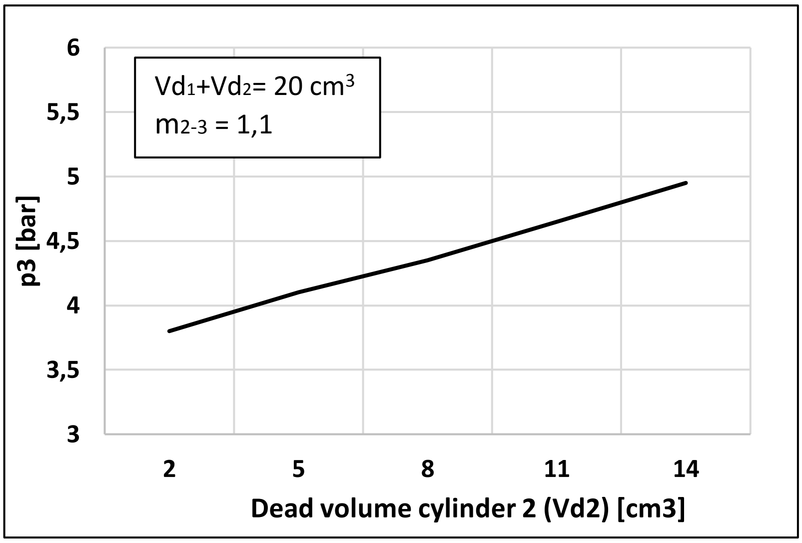

Figure 5.9 – Calculated values of p_3

Table 16- Parameters values used the modified multistage calculations

Inlet pressure	$p_{1'}$	1 bar
Cylinder 1 cubic capacity	V_{0_1}	172 cm^3
Cylinder 2 cubic capacity	V_{0_2}	38 cm^3
Polytropic exponent of compression 2-3	m	1.1
Sum of the dead volumes	$Vd_1 + Vd_2$	20 cm^3

Figure 5.8 shows that p_2 increase with the increasing of the second cylinder dead volume (despite the first cylinder dead volume is decreasing). This reduces the compression ratio of the compression 2-3 that is the one affected by the exchanger. This is the reason why the efficiency decreases with the increasing dead volume in the second cylinder. So, the dilemma on which valve is better to suppress between the "b" and the "c" (see paragraph 5.1) is solved: it is better to suppress the "b" valve so that the exchanger volume is added to the first cylinder dead volume and not to the second.

Figure 5.8 shows also that the mass compressed per round increase with the increasing of the second cylinder dead volume, because in this case the dead volume of the first cylinder is decreasing. In fact, this mass depends on the volumetric efficiency that, in this ideal case, depends only by the first cylinder dead volume and the maximum pressure reached by the first cylinder. This effect somehow counters the previous analysed effect. However, it is not enough to neutralise it, despite the maximum pressure is also increasing (see figure 5.9).

These evaluations are only the starting point for more detailed studies on theoretical, numerical and experimental basis. An a-dimensional approach may help to handle all those parameters. Probably, only the experimental tests will provide an answer on the actual mean polytropic exponent that can be reached.

6 Conclusions and future activities

6.1 Summary

This work aim was to explore a new solution to achieve near isothermal compression and expansion. The final aim was to use these solutions to obtain an Erikson's cycle in order to maximise the exploitations of low temperature thermal sources (up to 250 °C / 523 K). The solution adopted is the usage of a micro channel heat exchanger placed into the compression chamber of a reciprocating compressor.

An analysis on thermodynamic cycles at low maximum temperature has been performed and it is reported in paragraph 1.5. The compression measured polytropic exponent was not lowered by the exchanger throughout the experimental activities described in chapter three (the results are shown in chapter four).

Nevertheless, the tests on the compressor with the exchanger and high water flow rate (EXC_200 configuration) show that the performance can be improved through the internal exchanger. In fact, the air flow rate increased due to the lower air inlet temperature, even though the exchanger was designed to avoid secondary effects during the inlet phase. The temperatures of the outlet air and the lubricating oil were kept at exceptionally low levels: even with a water flow rate of 40 kg/h (EXC_40), at 9 barA, the maximum measured temperature is below 50 °C. In the future, smaller exchanger could be tested to determine the optimum between two contrasting aim: having high exchanging surfaces; keep the dead volume as small as possible.

The tests on the exchanger (chapter two) show that the exchanger efficiency is high (over 80%) even for low Reynolds number (from 580 to 1100). However, inside the compression chambers, the Reynolds chamber is extremely variable. In chapter four the calculation show that the Reynolds number goes from 40 (compression phase) to over 20000 (discharge phase). Extremely low Reynolds numbers lead to very low convective heat transfer coefficients during the compression phase, so that the compression polytropic exponent is not affected by the exchanger.

In chapter five a theoretical analysis on a new solution is carried. The low Reynolds number during the compression phase is a huge limit to the exchanger efficiency. This new solution tries to overcome this problem compressing the gas while it is moved from on cylinder to another. The theoretical analysis gives some hint on the best configuration for a new prototype. Also, it gives guidelines for more complex models that could help the next activities.

6.2 Main results

Even though the compressor cooling has not achieved a lower polytropic mean exponent, it managed to lower the both the overall machine temperature and the compressor specific work consumption. Moreover, further studies may lead to a better design of the exchanger and thus obtain even lower specific work consumption.

The low temperatures give less stress on the lubricating oil and the valves. Low temperatures also make the cooling fan useless: suppressing or downsizing the cooling fan lead to additional power saving. Moreover, they allow to achieve higher compression ratio within one compression stage. As a multistage compressor has its own drawbacks (more valves, friction and pressure losses), it is questionable whether the compressors with internal exchanger can be a possible alternative to multistage systems, given that the proposed solution is properly studied to optimize the exchanger design.

The proposed solution is also interesting in the hermetic compressor field, as the heat generated by the electric engine is added to the internal generated heat. Of course, while open type compressors can be modified aftermarket, the hermetic compressors cannot. However,

At the moment, the proposed solution is not suitable for a direct Ericsson engine. However, reciprocating compressors are used in heat pump cycles, cryogenic systems and many chemical and industrial processes. The practical possible advantages of the proposed solution may be discovered over time.

6.3 Future activities

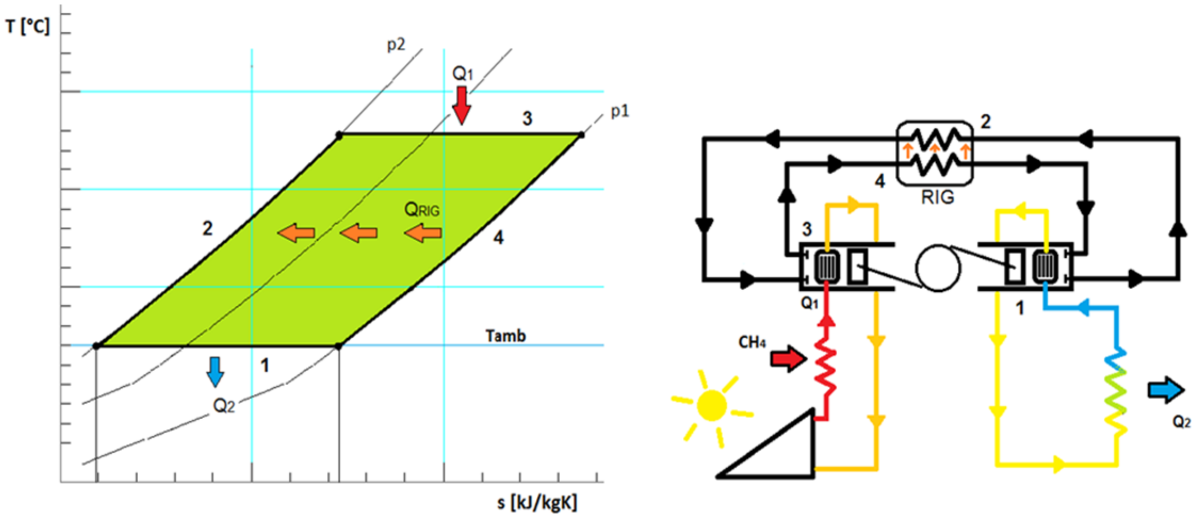

Figure 6.1 – Ericsson's cycle Ts diagram and Ericsson's engine

The final aim of the project is to obtain an Ericsson's engine that follows as much as possible the Ericsson cycle. Its main features are the machines (compressor and expander), the regenerator, the hot source and cold source exchangers. The key features are the machines, as the other components are already studied as parts of other engines (e.g. ORC and Stirling engines).

For example, the needed regenerator is a common device used in Joule cycles based engines (the type used in the Stirling engines is not suitable), solar collectors or burners are mature technologies, normal exchangers are not an issue. So, the main issue is to obtain transformations close to isothermal.

The most important missing technology for an actual Ericsson's engine is the one that allows near isothermal compressions and expansion, without too heavy drawbacks. This work tried to fill this gap, but, as already stated, it has not succeeded (yet). In chapter five another idea to overcome this issue is shown and theoretically analysed, but it is not experimentally verified yet. A prototype of the new compressor presented in chapter five is nearly completed. The prototype is similar to a multistage compressor: two bi-cylindrical compressors are combined to obtain a balanced machine. Both the valves "b" and "c" are present, and they will be suppressed one at a time, so that it is possible to test various configurations. The volume between the cylinders is reduced as much as possible: a MCHE is used and the basements of the two compressors are almost in contact. In the next future, a series of tests will be performed to verify whether it is possible to achieve a polytropic transformation near to an isothermal one. Also, a new Amesim model is under development. Until the tests, there are no data available to calibrate it, except the data on the compressor studied in this work.

Another issue is the presence of valves. The main physical difference between an Ericsson engine and a Stirling engine is that the former has machines with valves. The presence of the valves is a problem that must not be underestimated. The valves are a loss source and a practical complication. The expander valves are controlled valves. The control method is problematic especially at relatively high speed. In fact, the opening time of the inlet valve is just a small fraction of the piston stroke (from 30% to 50%). In appendix D, a study on a valve control system for an expander prototype is shown. The system was tested experimentally, and the results were not satisfying. However, the possibility to switch to an architecture similar to that shown in chapter five lead to an opening time of around 100% of the piston stroke, halving the requirements for the system. Other possible technical improvements of the tested control system are discussed in appendix D.

Overall bibliography

[1] Kang, Seok Hun. "Design and experimental study of ORC (organic Rankine cycle) and radial turbine using R245fa working fluid." Energy 41.1 (2012): 514-524.

[2] Blunier, B., et al. "A new analytical and dynamical model of a scroll compressor with experimental validation." International Journal of Refrigeration 32.5 (2009): 874-891.

[3] Gimelli, A., et al. "Reciprocating compressor 1D thermofluid dynamic simulation: problems and comparison with experimental data." International Journal of Rotating Machinery 2012 (2012).

[4] Elhaj, M., et al. "Numerical simulation and experimental study of a two-stage reciprocating compressor for condition monitoring." Mechanical Systems and Signal Processing 22.2 (2008): 374-389.

[5] Galindo, José, et al. "Modeling and experimental validation of a volumetric expander suitable for waste heat recovery from an automotive internal combustion engine using an organic rankine cycle with ethanol." Energies 9.4 (2016): 279.

[6] Nagy, Daniel, et al. "Valve lift measurement for the validation of a compressor simulation model." International Compressor Engineering Conference (2008).

[7] Stiaccini, Isacco, et al. "A reciprocating compressor hybrid model with acoustic FEM characterization." International Journal of Refrigeration 63 (2016): 171-183.

[8] Stouffs, Pascal, Mohand Tazerout, and Pierre Wauters. "Thermodynamic analysis of reciprocating compressors." International journal of thermal sciences 40.1 (2001): 52-66.

[9] Winandy, Eric, Claudio Saavedra, and Jean Lebrun. "Simplified modelling of an open-type reciprocating compressor." International journal of thermal sciences 41.2 (2002): 183-192.

[10] Longo, Giovanni A., and Andrea Gasparella. "Unsteady state analysis of the compression cycle of a hermetic reciprocating compressor." International journal of refrigeration 26.6 (2003): 681-689.

[11] Pereira, Evandro LL, Cesar J. Deschamps, and Fernando A. Ribas. "A comparative analysis of numerical simulation approaches for reciprocating Compressors." (2008).

[12] Dai, Yiping, Jiangfeng Wang, and Lin Gao. "Parametric optimization and comparative study of organic Rankine cycle (ORC) for low grade waste heat recovery." Energy Conversion and Management 50.3 (2009): 576-582.

[13] Gnutek, Z., and A. Bryszewska-Mazurek. "The thermodynamic analysis of multicycle ORC engine." Energy 26.12 (2001): 1075-1082.

[14] Loukopoulos, Panagiotis, et al. "Abrupt fault remaining useful life estimation using measurements from a reciprocating compressor valve failure." Mechanical Systems and Signal Processing 121 (2019): 359-372.

[15] Sharma, Vikas, and Anand Parey. "Performance evaluation of decomposition methods to diagnose leakage in a reciprocating compressor under limited speed variation." Mechanical Systems and Signal Processing 125 (2019): 275-287.

[16] Loukopoulos, Panagiotis, et al. "Reciprocating Compressor Valve Leakage Detection Under Varying Load Conditions." Asset Intelligence through Integration and Interoperability and Contemporary Vibration Engineering Technologies. Springer, Cham, 2019. 405-414.

[17] Xiao, Shungen, et al. "Nonlinear dynamic response of reciprocating compressor system with rub-impact fault caused by subsidence." Journal of Vibration and Control 25.11 (2019): 1737-1751.

[18] Tran, Van Tung, et al. "Single and combined fault diagnosis of reciprocating compressor valves using a hybrid deep belief network." Proceedings of the Institution of Mechanical Engineers, Part C: Journal of Mechanical Engineering Science 232.20 (2018): 3767-3780.

[19] Brok, S. W.; Touber, S.; and der Meer, J. S. Van, "Modeling of Cylinder Heat Transfer - Large Effort, Little Effect?" (1980). International Compressor Engineering Conference. Paper 305.

[20] Heidari, Mahbod; Lemofouet, Sylvain; and Rufer, Alfred, "On The Strategies Towards Isothermal Gas Compression And Expansion" (2014). International Compressor Engineering Conference. Paper 2285.

[21] Coney, M. W.; Stephenson, P.; Malmgren, A.; Linnemann, C.; Morgan, R. E.; Richards, R. A.; Huxley, R.; and Abdallah, H., " Development Of A Reciprocating Compressor Using Water Injection To Achieve Quasi-Isothermal Compression " (2002). International Compressor Engineering Conference. Paper 1508.

[22] Kremer, Rodrigo; Deschamps, Cesar J.; and Barbosa, Jader R., "Theoretical Analysis of the Effect of Oil Atomization in the Cylinder of a Reciprocating Ammonia Compressor" (2008). International Compressor Engineering Conference. Paper 1909.

[23] Guanwei, Jia, et al. "Micron-sized water spray-cooled quasi-isothermal compression for compressed air energy storage." Experimental Thermal and Fluid Science 96 (2018): 470-481

[24] Van de Ven, James D., and Perry Y. Li. "Liquid piston gas compression." Applied Energy 86.10 (2009): 2183-2191.

[25] Qin, Chao, and Eric Loth. "Liquid piston compression efficiency with droplet heat transfer." Applied Energy 114 (2014): 539-550.

[26] Acharya, Pinaki, Vikram C. Patil, and Paul Ro. "Experimental Investigation of Water Spray Cooling for Temperature Reduction in Liquid Piston Compressor." 24th International Compressor Engineering Conference at Purdue. 2018.

[27] Heidari, Mahbod, and Alfred Rufer. "Fluid Flow Analysis of a New Finned Piston Reciprocating Compressor Using Pneumatic Analogy." FDTT2014, Antalya, Turkey (2014).

[28] COZZOLINO, Raffaele. Surface heat exchanger for compressible fluid alternative volumetric machines. U.S. Patent Application No 13/584,202, 2013.

[29] Chlumski Vladimir, “Reciprocating and Rotary Compressors”, E & F N Spon, London, 1966

[30] Stone C. “The efficiency of Roots compressors and compressors with fixed internal compression”, Proceedings of the Institution of Mechanical Engineers, Part A: Power and Process Engineering (1988), 202(3), 199-205

[31] G.Brun, Thermodynamique des machine a fluide compressible, Paris, J.&R. Sennac, 1959

[32] Murugan, Sivalingam, and Bohumil Horák. "A review of micro combined heat and power systems for residential applications." Renewable and Sustainable Energy Reviews 64 (2016): 144-162.

[33] Rettig, A., Lagler, M., Lamare, T., Li, S., Mahadea, V., McCallion, S., & Chernushevich, J. (2011, September). “Application of organic Rankine cycles (ORC)”. In World Engineers’ Convention (pp. 1-10).

[34] Darvish, Kamyar, et al. "Selection of optimum working fluid for organic Rankine cycles by exergy and exergy-economic analyses." Sustainability 7.11 (2015): 15362-15383.

[35] Pereira, João S., et al. "ORC based micro-cogeneration systems for residential application–A state of the art review and current challenges." Renewable and Sustainable Energy Reviews 92 (2018): 728-743.

[36] Maghanki, Maryam Mohammadi, et al. "Micro combined heat and power (MCHP) technologies and applications." Renewable and Sustainable Energy Reviews 28 (2013): 510-524.

[37] Kongtragool, B., & Wongwises, S. (2003). “A review of solar-powered Stirling engines and low temperature differential Stirling engines”. Renewable and Sustainable energy reviews, 7(2), 131-154.

[38] Fula, A., Stouffs, P., & Sierra, F. (2013, March). “In-cylinder heat transfer in an Ericsson engine prototype”. In International Conference on Renewable Energies and Power Quality (ICREPQ’13) Bilbao (Spain), 20th to (No. 11, p. 6).

[39] Aksoy, F., Solmaz, H., Çinar, C., & Karabulut, H. (2017). “1.2 kW beta type Stirling engine with rhombic drive mechanism”. International Journal of Energy Research.

[40] Kong, X. Q., Wang, R. Z., & Huang, X. H. (2004). Energy efficiency and economic feasibility of CCHP driven by stirling engine. Energy Conversion and Management, 45(9), 1433-1442.

[41] Naso, V. (1991). La macchina di Stirling. Editoriale ESA, Masson, Milano.

[42] Wang, Kai, et al. "Stirling cycle engines for recovering low and moderate temperature heat: A review." Renewable and Sustainable Energy Reviews 62 (2016): 89-108.

[43] Gheith, Ramla, Fethi Aloui, and Sassi Ben Nasrallah. "Determination of adequate regenerator for a Gamma-type Stirling engine." Applied Energy 139 (2015): 272-280.

[44] Touré, A., & Stouffs, P. (2014). Modeling of the Ericsson engine. Energy, 76, 445-452.

[45] Ngangué, Max Ndamé, and Pascal Stouffs. "Dynamic simulation of an original Joule cycle liquid pistons hot air Ericsson engine." Energy 190 (2020): 116293.

[46] Creyx, M., et al. "Energetic optimization of the performances of a hot air engine for micro-CHP systems working with a Joule or an Ericsson cycle." Energy 49 (2013): 229-239.

[47] Hachem, Houda, et al. "Comparison based on exergetic analyses of two hot air engines: A Gamma type Stirling engine and an open joule cycle Ericsson engine." Entropy 17.11 (2015): 7331-7348.

[48] Cardone, M., and Gargiulo, B. "Design and experimental testing of a Mini Channel Heat Exchanger made in Additive Manufacturing". Energy Procedia, 148 (2018), 932-939.

[49] Esarte, J., et al. "Optimizing the design of a two-phase cooling system loop heat pipe: Wick manufacturing with the 3D selective laser melting printing technique and prototype testing." Applied Thermal Engineering 111 (2017): 407-419.

[50] Thompson, Scott M., et al. "Additive manufacturing of heat exchangers: A case study on a multi-layered Ti–6Al–4V oscillating heat pipe." Additive Manufacturing 8 (2015): 163-174.

[51] Arie, Martinus A., Amir H. Shooshtari, and Michael M. Ohadi. "Experimental characterization of an additively manufactured heat exchanger for dry cooling of power plants." Applied Thermal Engineering 129 (2018): 187-198.

[52] Khan, Mesbah G., and Amir Fartaj. "A review on microchannel heat exchangers and potential applications." International journal of energy research 35.7 (2011): 553-582.

[53] Wang, Hailei, and Richard B. Peterson. "Performance enhancement of a thermally activated cooling system using microchannel heat exchangers." Applied Thermal Engineering31.14-15 (2011): 2951-2962.

[54] Qi, Zhaogang, Yu Zhao, and Jiangping Chen. "Performance enhancement study of mobile air conditioning system using microchannel heat exchangers." International Journal of refrigeration 33.2 (2010): 301-312.

[55] Kwon, Beomjin, et al. "High power density air-cooled microchannel heat exchanger." International Journal of Heat and Mass Transfer 118 (2018): 1276-1283.

[56] Mundinger, D., et al. "Demonstration of high-performance silicon microchannel heat exchangers for laser diode array cooling." Applied physics letters 53.12 (1988): 1030-1032.

[57] Wu, Peiyi, and W. A. Little. "Measurement of the heat transfer characteristics of gas flow in fine channel heat exchangers used for microminiature refrigerators." Cryogenics 24.8 (1984): 415-420.

[58] W.M. Kays, A.L. London, "Compact Heat Exchangers", Third Edition, Krieger Pub, Co, Malabar,FL, 1998.

[59] Shah, Ramesh K., and Alexander Louis London. "Laminar flow forced convection in ducts: a source book for compact heat exchanger analytical data". Academic press, 2014.

[60] Chattopadhyay, Himadri, Franz Durst, and Subhashis Ray. "Analysis of heat transfer in simultaneously developing pulsating laminar flow in a pipe with constant wall temperature." International communications in heat and mass transfer 33.4 (2006): 475-481.

[61] Hemida, H. N., et al. "Theoretical analysis of heat transfer in laminar pulsating flow." International Journal of Heat and Mass Transfer 45.8 (2002): 1767-1780.

[62] Frazier, William E. "Metal additive manufacturing: a review." Journal of Materials Engineering and Performance 23.6 (2014): 1917-1928.

[63] STOUFFS, Pascal, Max Ndamé Ngangué, and Olivier Sosso Mayi. "Study of three valves command laws of the expansion cylinder of a hot air engine." International Journal of Thermodynamics 22.2 (2019): 84-96.

Appendix A Sensors

A1 Load cell

A load cell is a transducer that gives an electric signal proportional to the applied force. It is placed at the end of the arm of an oscillating casing electric motor. In this way, it is possible to measure the compressor torque. Multiplying it with the compressor angular speed, the compressor power consumption is obtained:

$$P = T \cdot \omega = F \cdot r \cdot \omega \qquad [A.1]$$

where T is the torque, ω is the angular speed, F is the applied force and r is the length of the arm.

Document A1 – Load cell TPR 25 technical specifications

PAVONESYSTEMS

Load Cells

S-Type load cell **TRP**

available with certification • EAC

Technical specifications

PVS1020190912

Rated load RL:	2, 5, 10, 15, 25, 50 Kg
Combined error:	±0.05 % RL
Repeatability:	±0.02 % RL
Creep (20 minutes):	±0.03 % RL
Safe overload:	150 % RL
Ultimate overload:	> 300 % RL
Ultimate sideload:	300 % RL
Material:	Stainless steel
Degree of protection:	IP65
Deflection:	0.4 mm
Compensated Temperature:	-10 ÷ +50°C
Temperature range:	-20 ÷ +70°C
Temperature effect on zero balance:	±0.005 % RO/°C
Temperature effect on output:	±0.005 % output/°C
Rated output RO:	2.0 mV/V ±0.1 %
Zero balance:	±1 % RO
Insulation resistance:	> 5000 MOhm
Input resistance:	350 ±10 Ohm
Output resistance:	350 ±10 Ohm
Recommended input:	5 ÷ 15 Vdc/ac
Power supply:	2 ÷ 15 Vdc/ac

Figure A.1 – Load cell TRP25

A2 Pressure sensors: average pressure and instantaneous pressure

The used average pressure sensor is a piezoresistive transducer. The model is Druck PMP 1400, with a maximum operating pressure of 16 bar g.

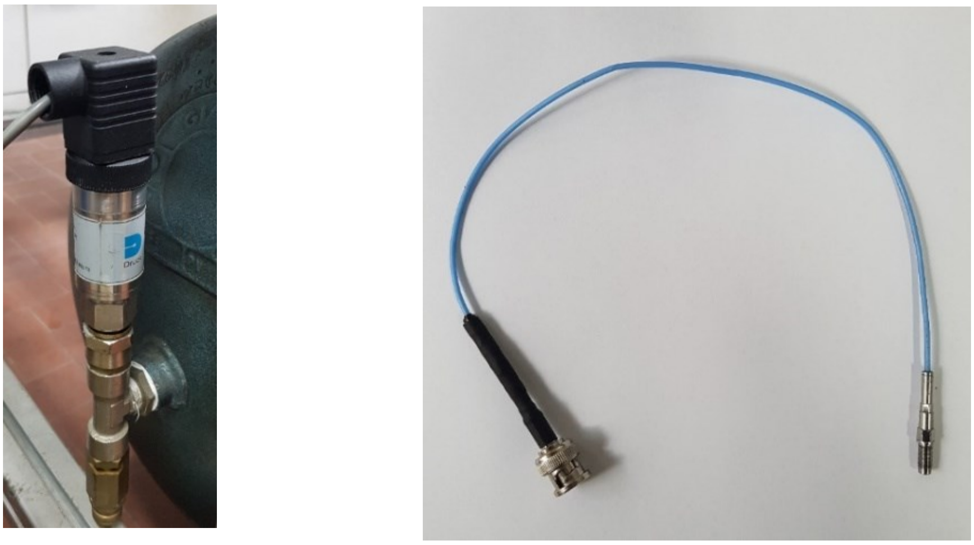

Figure A.2 – Average pressure sensor (left); Instantaneous pressure sensor (right)

GE
Sensing

PTX/PMP 1400 Specifications

Pressure Measurement

Operating Pressure Ranges
- 0, to 1.5, 3.75, 6, 9, 15, 24, 37.5, 60, 90, 160, 240, 375, 600, 900 psi (0 to 100, 250, 400, 600 mbar, 1, 1.6, 2.5, 4, 6, 10, 16, 25, 40, 60 bar) gauge and absolute
- 0 to 1500, 2400, 3750, 6000, 9000, psi (0 to 100, 160, 250, 400, 600 bar) sealed gauge and absolute
- Barometric
  - 12 to 18 psia (800 to 1200 mbar); PTX 1400 only
  - -15 to 24 psig (-1 to 1.6 bar); compound
  - -15 to 37.5 psig (-1 to 2.5 bar); compound
  - -15 to 60 psig (-1 to 4 bar); compound

Overpressure
The rated pressure range can be exceeded by the following without degrading performance:
- 4 x FS for ranges up to 15 psi (1 bar)
- 2 x FS (2700 psi/180 bar maximum) for ranges 15 to 1500 psi (1 to 100 bar)
- 2 x FS (13,500 psi/900 bar maximum) for ranges 2400 to 9000 psi (160 to 600 bar)

Containment
- 6 x FS for ranges up to 15 psi (1 bar)
- 3 x FS for ranges up to 1500 up to 2700 psi (100 bar to 180 bar) max
- 20,000 psi (1400 bar) max above 1500 psi (100 bar).

Pressure Media
Fluids compatible with a fully welded assembly of:
- 316L stainless steel for ranges 3.75 psi (250 mbar) and below
- 316L stainless steel and Hastelloy C276 for all other ranges

Supply Voltage
PMP 1400: 9 to 30 VDC
PTX 1400: 9 to 28 VDC
Minimum supply voltage that must appear across transmitter terminals is 9V and is given by
Vmin= Vs - (0.02 x RL)
Where Vs = supply volts
RL = total loop Ohms

Supply voltage reversal–units will withstand reversed polarity without damage.

Output Voltage
PMP 1400: 0 to 5V - calibrated between 5 to 100% full scale (FS) (three-wire pedestal configuration)
PTX 1400: 4 to 20mA (two-wire configuration)

Load Impedance (PMP version)
Greater than 100 k ohms for quoted performance

Performance

Accuracy
Combined non-linearity, hysteresis and repeatability: ±0.15% typical, ±0.25% maximum best straight line (BSL) definition

Zero Offset and Span Setting
Factory set to 0.5% FS, then ±5% site adjustable by sealed, non-interacting potentiometers

Long Term Stability
0.2% FS range per annum typical

Operating Temperature Range
-4°F to 176°F (-20°C to 80°C)

Temperature Effects
- Total error band (TEB) 1.5% FS typical, 2% FS maximum, -4°F to 176°F (-20°C to 80°C)
- For ranges below 6 psi (400 mbar) values increase pro-rata with calibrated span

Physical

Pressure Connection
G 1/4 female

Electrical Connection
DIN 43650 plug supplied with mating socket

Weight
0.4 lb (200 g) nominal

Ingress Protection
Sealed to IP65

CE marking
CE marked for use in potentially explosive atmospheres, pressure equipment directive and electromagnetic compatibility

The instantaneous pressure sensor is a piezoelectric transducer produced by Kistler. The model is Kistler 6052B.

Type	Measuring range	Sensitivity
6052B	1) 0…250 bar 2) 0…50 bar	1) -19.6 pC/bar 2) -19.5 pC/bar

Document A3 – Kistler 6052B technical specifications

High-Temperature Pressure Sensor for combustion engine measurement, Type 6052B

KISTLER
measure. analyze. innovate.

Technical Data

Range	bar	0 … 250
Calibrated partial range	bar	0 … 50
Overload	bar	300
Sensitivity	pC/bar	≈-20
Natural frequency (sensor element)	kHZ	≈130
Linearity, all ranges at RT	% FSO	≤±0,4
Acceleration sensitivity		
axial	bar/g	<0,0002
radial	bar/g	<0,0005
Operating temperature range	°C	-50 … 400
Sensitivity shift		
200 ±50 °C	%	<0,5
23 - 350 °C	%	<2
Thermal shock error		
at 1500 u/min, 9 bar pmi		
P (short-time drift)	bar	≤ ± 0,5
Pmi	%	≤ ± 2
Pmax	%	≤ ± 1,5
Insulation resistance		
at 20 °C	TΩ	≥10
Shock resistance	g	2000
Tightening torque	Nm	1,5
Capacitance, without cable	pF	5
Weight, with cable	g	20
Plug, ceramic insulator		M4 x 0,35

It converts a pressure into an electric charge, so an amplifier is needed. The amplifier was the Kistler type 5011B.

Figure A.3 – Charge amplifier

Document A4 – Kistler 5011B technical specifications

Charge Amplifier – Single-channel multi-range laboratory charge amplifier, Type 5011B...

KISTLER
measure. analyze. innovate.

Technical Data

Basic unit		
Measuring range for 10 V FS	pC	±10 ... ±999 000
Sensor sensitivity [T] (M.U. = Mechanical units)	pC/M.U.	±0,01 ... ±9 990
Scale [S]	M.U./V	0,001 ... 9'990'000
Output voltage	V	±10
Output current (short-circuit protected)	mA	±5
Output impedance	Ω	10
Frequency range (–3dB, Filter "OFF")	kHz	≈0 ... 200
Low-pass filter upper cutoff frequency -3dB Butterworth, 2 pin 8 stages (1, 3, 10 ...)	kHz (%)	0,01 ... 30 (±10)
Time constant [TC] (high pass filter)		
Long	s	>1 000 ... 100 000
Medium ($T = R_g \cdot C_g$)	s	1 ... 10 000
Short ($T = R_g \cdot C_g$)	s	0,01 ... 100
Error		
<±100 pC FS (max./typ.)	%	<±3/<±2
≥±100 pC FS (max./typ.)	%	<±1/<±0,5
Linearity	% FS	<±0,05
Noise	mV_{rms}	<0,5 (<1,5)

Version ...Y50, Drift compensation; at [TC] setting "Drco"		
Time constant [TC] (High-pass filter)		
Long	s	>1 000 ... 100 000
Drco	–	Driftcompensation
Short ($T = R_g \cdot C_g$)	s	0,01 ... 100
Driftcompensation; at [TC] setting "Drco"		
Range for ±10 V FS	pC	±100 ... ±999 000
Zero point error	mV	<±20
Max. Error in signal repetition frequency range	%	<1
Signal repetition frequency range	Hz	5 ... in dependence of the selected low-pass filter

Option: Parallel Interface IEEE-488 Type 5605A

Standardized interface with IEC 625-1 electrically compatible for remote control and checking of all parameters. Measured data are not transmitted.

Standard used	Type	IEEE-488-1978
Max. distance between 2 instruments	m	2
Max. bus length	m	20
Max. number of instruments on the bus	–	15

9,99 pC/V (1 pC/V)	mV_{pp}	<4 (<8)
Loss due to cable capacitance	pC_{rms}/pF	$<2 \cdot 10^{-5}$
Drift at 25 °C	pC/s	<±0,07

General Data

Operating temperature range	°C	0 ... 50
Connections		
Measuring input/signal output	–	BNC negative
Remote control	–	Connector 6 pin
(Operate, Overload, ...)		DIN 45322
Power plug	–	IEC 320 C 14
Conformity to EC Directive		
Safety	–	EN 61010-1
EMC Interference Emission	–	EN 50081-1/EN 50081-2
EMC Interference Immunity	–	EN 50082-1/EN 50082-2
Power, switchable	VAC (%)	230/115 (-22/+15)
(Protection class I)	Hz (VA)	48 ... 62 (20)
Voltage between protection and measuring ground	V_{rms}	<50
Dimensions		
with desktop case Type 5747A1	mm	94x141x195
for rack mounting	mm	71,12x128,7x169
Front panel according to	HE (mm)	3 (128,7)
DIN 41494 (Part 5)	TE (mm)	14 (71,12)
Weight (incl. IEEE-488 or RS-232C)	kg	≈2

Address range	–	30
Functions	–	Listener, Talker

Option: Serial Interface RS-232C Type 5611A

Standardized interface for remote control and checking of all parameters. Measured data not transmitted.

Standard used	Type	RS-232C resp. V24
Max. cable length	m (pF)	20 (2 500)
Baud rates	Baud	50, 110, 250, 300, 600, 1 200, 2 400, 4 800
Number of data bit	Bit	7 or 8
Number of stop bit	Bit	1 or 2
Parity	–	without, even or odd
Software protocol	XON/XOFF	not allowed

5011B_000-296e-12.05

Page 2/6

This information corresponds to the current state of knowledge. Kistler reserves the right to make technical changes. Liability for consequential damage resulting from the use of Kistler products is excluded.

A3 The encoder

The encoder is a transducer of angular displacement. It gives a fixed number of digital pulses per round. In this case there are 500 pulses per round. The pulses are given at regular angular displacement. At any time, it is possible to know the shaft angular position thanks to a pulses counter. Moreover, it is possible to measure the rotational speed considering the period between the pulses. The used encoder was produced by Baumer. The model is: Bhk 06.05A500-B6-5.

Figure A.4 – Encoder

Part number

BHK 16. [ ][ ] - [ ] - [ ]

Connection
5 Cable 1 m, radial
9 Connector radial

Shaft
B2 End shaft ø12 mm, IP 42, with clamping ring
B6 Hollow shaft ø6 mm, IP 42, with clamping ring
E6 Hollow shaft ø6 mm, IP 64, with clamping ring
I2 End shaft ø12 mm, IP 42, with clamping ring and sping plate
M6 Hollow shaft ø6 mm, IP 64, with clamping ring and spring plate

See part number (pulses)

Voltage supply / signals
05A 5 VDC / antivalent (TTL compatible)
24K 10...30 VDC / push-pull short circuit-proof

Part number (pulses)

10	50	120	360	1024
20	60	200	500	2000
30	100	250	1000	2048

Other pulse numbers upon request.

Trigger level

Outputs 05A	**Complementary Linedriver RS422**
Output level High	>2,4 V (I = -20 mA)
Output level Low	<0,4 V (I = 20 mA)
Load High	<20 mA
Load Low	<20 mA

Outputs 24K (125 Ω)	**Push-pull** short-circuit protection
Output level High	>+Vs - 5,7 V (I = -30 mA)
Output level Low	<5,7 V (I = 30 mA)
Load High	<30 mA
Load Low	<30 mA

Accessories

Connectors and cables	
10132983	Female connector M9, 8-pin, straight
10123168	Female connector M9, 8-pin, straight, 2 m cable
10123169	Female connector M9, 8-pin, straight, shielded, 5 m cable
10123166	Female connector M9, 5-pin, straight, shielded, 2 m cable
10123167	Female connector M9, 5-pin, straight, shielded, 5 m cable
Mounting accessories	
10158423	Set of spring coupling (round) for hollow shaft encoder (<ø8 mm)
10158424	Set of spring coupling (square) for hollow shaft encoder (≥ø8 mm)

A4 Air and oil temperature sensors

Two thermocouples measure the air temperature, one at the intake and the other at the compressor delivery. They are class B K-type thermocouples.

Figure A.5 – Termocouple

Document A6 – Thermocouple technical specifications

Tolerance classes for thermocouples according to the IEC 60 584-2:1995

Thermocouple	Class 1 (°C)	Class 2 (°C)	Class 3 (°C)
Type T			
Temperature	- 40 ≤ t ≤ 125	-40 ≤ t ≤ 133	-67 ≤ t ≤ 40
Tolerance	±0,5	±1	±1
Temperature	125 ≤ t ≤ 350	133 ≤ t ≤ 350	-200 ≤ t ≤ -67
Tolerance	±0,004•|t|	±0,0075•|t|	±0,015•|t|
Type E			
Temperature	-40 < t ≤ 375	-40 ≤ t ≤ 333	-167 ≤ t ≤ 40
Tolerance	±1,5	±2,5	±2,5
Temperature	375 ≤ t ≤ 800	333 ≤ t ≤ 900	-200 ≤ t ≤ -167
Tolerance	±0,004•|t|	±0,0075•|t|	±0,015•|t|
Type J			
Temperature	-40 < t ≤ 375	-40 ≤ t ≤ 333	-
Tolerance	±1,5	±2,5	-
Temperature	375 ≤ t ≤ 750	333 ≤ t ≤ 750	-
Tolerance	±0,004•|t|	±0,0075•|t|	-
Type K and N	*Also see the diagramme below*		
Temperature	-40 < t ≤ 375	-40 ≤ t ≤ 333	-167 ≤ t ≤ 40
Tolerance	±1,5	±2,5	±2,5
Temperature	375 ≤ t ≤ 1000	333 ≤ t ≤ 1200	-200 ≤ t ≤ -167
Tolerance	±0,004•|t|	±0,0075•|t|	±0,015•|t|
Type S and R			
Temperature	0 < t ≤ 1100	0 ≤ t ≤ 600	-
Tolerance	±1	±1,5	-
Temperature	1100 ≤ t ≤ 1600	600 ≤ t ≤ 1600	-
Tolerance	±[1+0,003(t-1100)]	±0,0025•|t|	-
Type B			
Temperature	-	-	600 ≤ t ≤ 800
Tolerance	-	-	±4
Temperature	-	600 ≤ t ≤ 1700	800 ≤ t ≤ 1700
Tolerance	-	±0,0025•|t|	±0,005•|t|

Temperature referency
Reference point is 0 °C

Explanation
|t| = is the positive value of the temperature t.

Tolerances
The tolerances of the table should be taken as guideline values. They are valid only for unused thermocouples.

Sources of error
Many factors such as high temperature combined with time of exposure, vacuum, or drawn wire can quickly lead to deviations that override the tolerances given in the table.

NB
The coloured markings used here have nothing to do with any colour coding of thermocouples.

A5 Water temperature sensor

In order to measure small temperature differences between the exchanger inlet and outlet, two class B 2 wires Pt100 thermoresistance are used.

Document A7 – Thermoresistences technical specifications

Tolerances, Pt100 and Pt1000

The tolerance values of resistance thermometers are classified as follows:

Tolerance class	Tolerance (°C)
A	0.15 + 0.002 |*t*|*
B	0.3 + 0.005 |*t*|

* \|*t*\| = modulus of temperature in degrees Celsius without regard to sign.

Temperature (°C)	Tolerance Class A (± °C)	Class A (± Ω)	Class B (± °C)	Class B (± Ω)
-200	0.55	0.24	1.3	0.56
-100	0.35	0.14	0.8	0.32
0	0.15	0.06	0.3	0.12
100	0.35	0.13	0.8	0.30
200	0.55	0.20	1.3	0.48
300	0.75	0.27	1.8	0.64
400	0.95	0.33	2.3	0.79
500	1.15	0.38	2.8	0.93
600	1.35	0.43	3.3	1.06
650	1.45	0.46	3.6	1.13
700	-	-	3.8	1.17
800	-	-	4.3	1.28
850	-	-	4.6	1.34

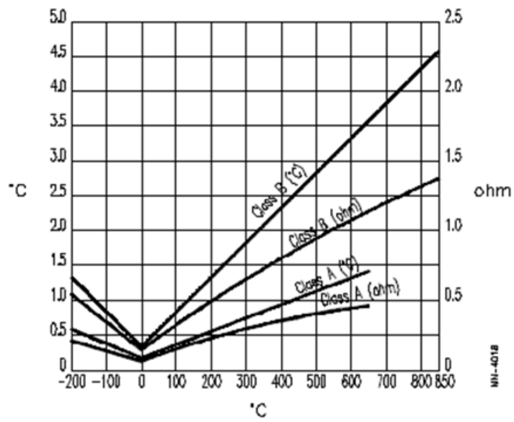

A6 Volumetric air flow meter

The air flow meter was a pulse quantometer Elster QAe40 25GI E200. It gives 500 pulses per cubic meter. Once calculated the air density, it is possible to trace it back to the mass flow rate.

Figura A.6 – Volumetric air flow meter

Document A8 – Elster quantometer technical specifications

Elster Quantometer QA / QAe Technical Specifications

Technical data								
			Max. working pressure		Accuracy		Pulse values [imp/m³]	
Nominal Size	Type	Measuring range [m³/h]	Air, inert gases	Flammable gases e.g. natural gas	20% to 100% Qmax	10% to 20% of Qmax	LF output (E1)	MF output (E200)
DN 25 / 1"	10	1.6 - 16	16 bar	4 bar	+/-1.5%	+/-6%	10	500
DN 25 / 1"	16	2 - 25				+/-3%		
DN 25 / 1"	25	2.5 - 40						
DN 25 / 1"	40	3.3 - 65						
DN 40 / 1.5"	40	5 - 65					1	250
DN 50 / 2"	65	6 - 100	16 bar (PN16) 20 bar (ANSI 150)					
DN 80 / 3"	100	10 - 160						187.5
DN 80 / 3"	160	13 - 250						
DN 80 / 3"	250	20 - 400						
DN 100 / 4"	250	20 - 400						
DN 100 / 4"	400	32 - 650						
DN 150 / 6"	400	32 - 650						
DN 150 / 6"	650	50 - 1000						
DN 150 / 6"	1000	80 - 1600						

A7 Water flow meter

The water flow meter was a Promag 50 HART that is a magnetic transducer. It uses the electromagnetic induction. The liquid acts as a metal spiral. As it gets through a magnetic field with a certain speed, a magnetic flux variation is made and then an electric voltage difference.

Figure A.7 – Promag 50 HART

10 Technical data

10.1 Application

→ 📄 4

10.2 Function and system design

Measuring principle	Electromagnetic flow measurement on the basis of Faraday's Law.
Measuring system	→ 📄 6

10.3 Input

Measured variable	Flow velocity (proportional to induced voltage)
Measuring range	Typically v = 0.01 to 10 m/s (0.033 to 33 ft/s) with the specified accuracy
Operable flow range	Over 1000 : 1
Input signal	**Status input (auxiliary input)** ▪ Galvanically isolated ▪ U = 3 to 30 V DC ▪ Ri = 5 kΩ ▪ Can be configured for: totalizer reset, positive zero return, error message reset.

10.4 Output

Output signal	**Current output** ▪ Galvanically isolated ▪ Active/passive can be selected: – Active: 0/4 to 20 mA, R_L < 700 Ω (HART: $R_L \geq$ 250 Ω) – Passive: 4 to 20 mA, supply voltage V_S 18 to 30 V DC, $R_i \geq$ 150 Ω) ▪ Time constant can be selected (0.01 to 100s) ▪ Full scale value adjustable ▪ Temperature coefficient: typ. 0.005% o.f.s./°C, resolution: 0.5 µA

A8 IR Thermometer

The Fluke 62 MINI is an IR thermometer. It was used to measure the external surface temperature of the basement, the cylinder head and the exchanger. The measure is affected also by the operator dexterity, so it cannot be considered very precise. However, it gives a starting point for further considerations or improvements.

Document A10 – Fluke 62 MINI technical specifications

Specifications

Measurement range	-30 °C to 500 °C (-20 °F to 932 °F)
Accuracy	10 °C to 30 °C (50 °F to 86 °F): ± 1 °C (2 °F) Outside 10 °C to 30 °C (50 °F to 86 °F): ± 1.5 °C (3 °F) or ± 1.5% of reading, whichever is greater
Repeatability	±0.5% of reading or ≤ ±1 °C (±2 °F), whichever is greater
Emissivity	Preset 0.95
Response time	< 500 mSec
Distance to spot size	10:1 calculated @ 80% energy
Spectral range	6.5–18 microns thermopile detector
Display resolution	0.2 °C (0.5 °F)
Display hold (7 seconds)	•
LCD backlit	•
Temperature display	°C or °F selectable
Ambient operating range	0 to 50 °C (32 to 120 °F)
Relative humidity	10-90% RH non-condensing, @ up to 30 °C (86 °F)
Typical distance to target (spot)	Up to 2 m (6 ft)
Laser class II	Single offset laser
Weight/dimensions	200 g (7 oz); 152 x 101 x 38 mm (6 x 4 x 1.5 in)
Power	9 V Alkaline battery (included)
Battery life (alkaline)	12 hours
Storage temperature	-20 °C to 65 °C (-4 °F to 150 °F) without battery
Options/accessories:	Includes protective boot and storage holster
Warranty:	2 years (conditional)

Appendix B Programming with Labview FPGA

All the sensors described in chapter 3, 4 and appendix A are modern transducers that convert the observed physical quantities in electric signals (current, voltage or frequency based). To digitalise those signals and transmit them to a computer, an electronic converter is needed. A possible alternative on the market is a National Instruments Corporation electronic board. The test benches described in this work used one of these board, exactly a C-Rio 9022 controller paired with a C-Rio 9114 expansion chassis. All National Instruments boards communicate with a computer through Ethernet cables, USB cables or PCI/PCIe ports. At last, the data are read by programs written in Labview code. Labview is the National Instrument program development environment. The user can write his own program that acquire data, control instruments and communicate through National Instruments boards. Through a user made program the data might be observed in real time, post processed and saved for further purposes. National Instruments provides many products. Among them, each C-Rio series board have an internal processor and FPGA circuit that allow stand alone and HIL applications. A C-Rio board is made up of three parts: the controller, the chassis and, at least, one module. The modules are the location of the analog to digital converter (ADC) and are the parts where the sensors are physically connected. Each module is built to perform a specific task, such as reading thermocouples, reading thermoresistances, reading/writing 5V TTL signals, reading/writing analog signals, control PWM motors and many others. The chassis connect them to the controller, where there is the onboard processor.

The writing of the Labview code needed to read and process the test bench data was an integral part of this doctorate work.

Among the National Instruments boards, those with FPGA (such as C-Rio, PXI and others) are more difficult to deal with than the DAQ board or the old Field Point board. As they permit higher degree of freedom, the programming must be done at a lower level (relatively low level, as the language is still the graphical language of Labview). A Labview project suitable for C-Rio boards is made up of at least two different communicating main program, but in this case three programs are needed. These programs have each a different target: the first one “runs” on the FPGA circuit (it is named FPGA program), the second one runs on the onboard operating system and processor (it is named RT program), the third one runs on the computer (it is named Host program). The three programs have different aims. Usually, the Host program duty is that of collecting the data from the other two programs, let the user visualise them, and eventually post process and save them. The RT program can act as the Host program in stand-alone applications: it acquires the digitalised data and could perform some postprocessing operations or save the data on onboard memories. However, the onboard speed and resources are limited, and if there is an external computer the RT program is used for scanning the low speed modules channels, acquire the data, and convert the electric values into physical units. This last task is particularly easy on RT programs as the modules are automatically recognised by the onboard controller, so for modules that acquire from standard sensors (such as the thermocouple modules) there are dedicated “drivers”. If there are no drivers, such as for general purpose modules, the RT program is just a medium between the channels and the Host program. The FPGA program is used whenever there are fast changing data that the onboard controller cannot acquire. The FPGA program is also used for HIL application at whenever the speed must be higher than 100 Hz. The FPGA program cannot use drivers. Even a basic edge counter must be self-programmed. On the other hand, under favourable circumstances, an FPGA loop speed can be performed in 25 ns (40 MHz)

The user must also define the communicating protocols between the three main program. There are several protocols available, but they can be classified into two groups: queued protocols and last value protocols. In the most complex cases (but not in this work case) the communication could be extended to more boards or computers through National Instruments protocols or standard protocols (such as TCP/IP protocol).

This work test bench has different sensors. Many are slow sensors, such as the thermocouples. On the other hand, the indicated cycle needs many points per revolution. At 1000 RPM, to acquire 500 point per revolution requires more than 8000 samples per second, that is beyond the onboard processor capabilities.

B1 FPGA code

The encoder (5V TTL signal) and the high-speed pressure sensors (voltage signal) are acquired by the FPGA circuit. The encoder signals are used as triggers to acquire the pressure signals. This way it is possible to associate each pressure values to a crankshaft position and then to a cylinder volume (figure B1).

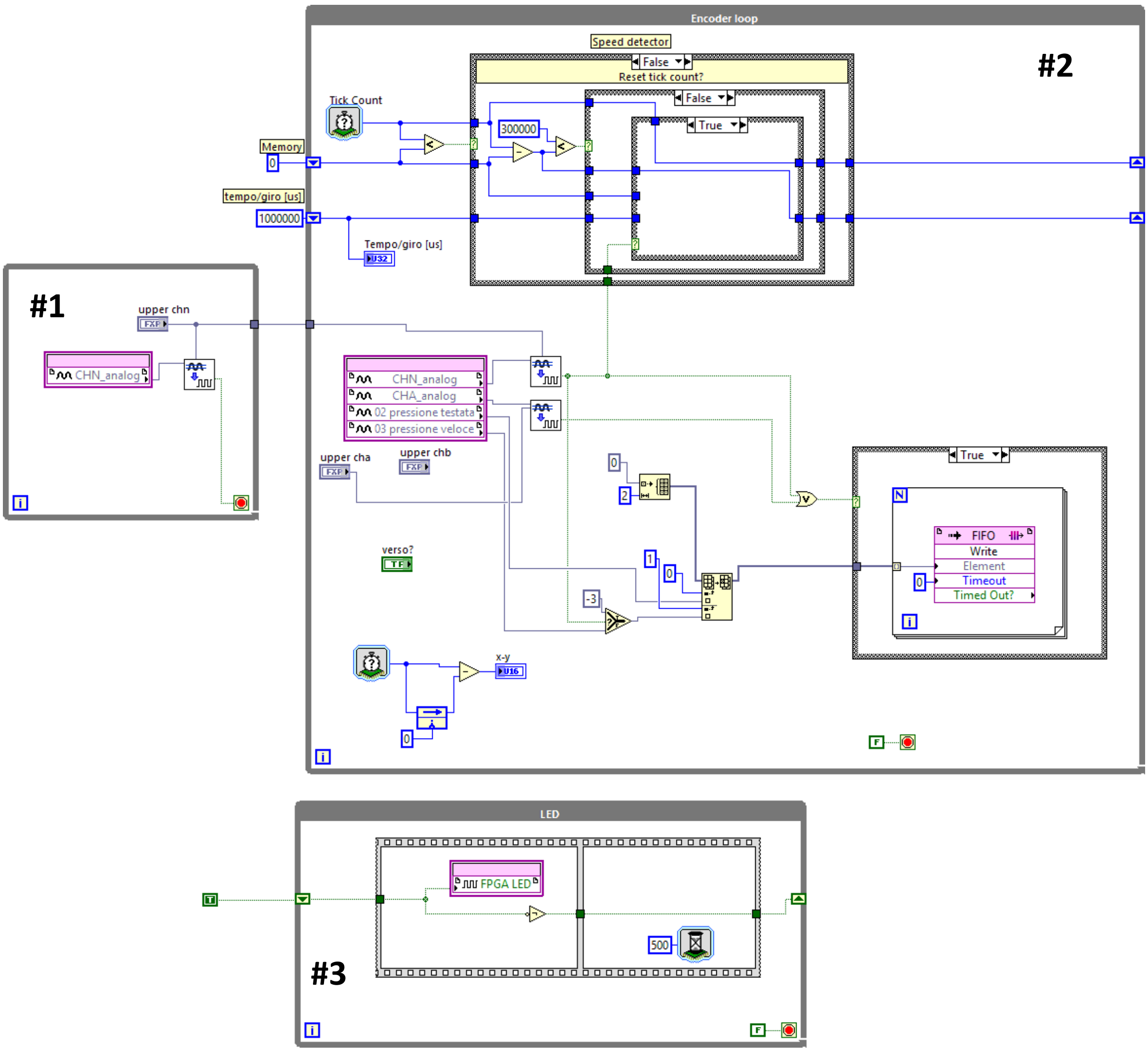

Figure B.1 – Labview FPGA code for the compressor test bench

The acquisition session starts when the Encoder CHN signal rising edge is detected (while loop #1). CHN signal gives one pulse per revolution and the encoder was set so that the rising edge of CHN signal is given at the lower dead centre of the monitored cylinder. Unluckily, the TTL signal was disturbed, so it was acquired as an analog signal and then transformed in Boolean values via software using the block shown in figure B.2. The sub-program written inside this block is shown in figure B.3.

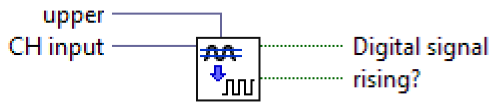

Figure B.2 – Icon of the sub-program used for the signal transformation

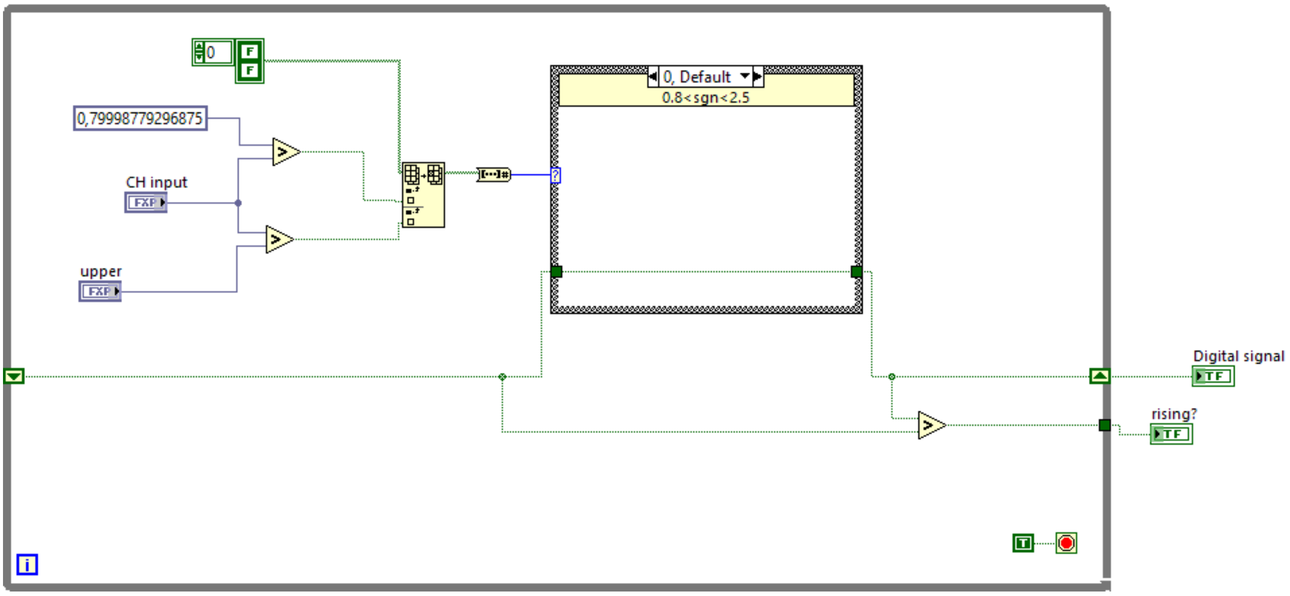

Figure B.3 – Code of the sub-program used for the signal transformation

This subprogram not only transforms the analog data in a squared wave (Boolean data), but also detect the rising edge of the square wave.

In the while loop #2 there is the core of the FPGA program. All the encoder channels are acquired and transformed to square waves by the subprogram shown above. Every time a rising edge of the CHA encoder signal is detected, the cylinder pressure is acquired. Then, all the acquired pressure values are sent to the RT program through a first in first out queue. Every time a rising edge of the CHN encoder signal is detected, a negative conventional number is insert into the queue to signal the start of a new revolution.

After the first test campaign, a second high-speed pressure sensor was added in the cylinders head. The aim was to detect potential pressure waves in the outlet pipes. However, no odd pressure wave was detected. Nevertheless, the signal was acquired. The NI 9114 chassis, used in this project, allow just one queued stream between FPGA and RT program. So, the interleaving technique was implemented to send two signals in the same queue.

The upper part of the while loop #2 uses the encoder signals to detect the shaft speed. The onboard clock ticks between two consecutive rising edges are counted to calculate the time elapsed per revolution. These speed values are sent to the RT program through a "last value" protocol, so the RT program does not read all the values but only one every RT while loop cycle (figure B.5 while loop #2).

B2 RT code

As the thermocouples and thermoresistances have a dedicated module, they are directly acquired by the RT program, as well as the mean pressure sensors (general purpose voltage module), and the water flow rate sensor (general purpose current module). All these sensors measure mean quantities that does not need high speed acquisition. The air flow rate sensor gives a frequency signal, but this frequency is low enough to be acquired by the onboard processor.

Figure B.5 shows the RT program. After some side functions, the subprogram "Connect to FPGA" is lunched. Its purpose is to initialise and set parameters concerning the communication between the FPGA circuit and the onboard processor. Finally, the communication is started (figure B.4).

Then, six parallel loops run together. Each of them has a specific task:

- The first one simply switches a led on and off repeatedly to signal that the RT program is running.
- The second loop handle the stream of data between the FPGA and the RT programs. It packages the values sent by the FPGA program in an array and sent the array to cycle #3 through a queued stream. It also transmits the "time elapsed per revolution" value sent by the FPGA program to the Host program through a "last value" communication protocol (Network Published Shared Variables).
- The third loop handle a queued communication (Network Stream) between the RT and Host program. After the connection is established, the loop uses the communication to send the data from the loop #2 to the Host program
- The fourth loop reads all the data from low speed sensors and sends them to the Host program through a "last value" communication protocol (Network Published Shared Variables). The only exception is the air flow rate data.
- The fifth loop handle the air flow rate data. It is a special loop that has priority over the others, so that it must execute every 33 ms. This way the sample rate of the acquisition is stable. This is particularly important because the air flow rate is proportional to the signal frequency, and any potential sample rate shift may distort the wavelength. After the acquisition the loop send the data to the sixth loop through a special queued communication protocol (deterministic RT FIFO).
- The sixth loop takes the data from the fifth and uses a queued communication protocol (Network Stream) to send them to the Host program.

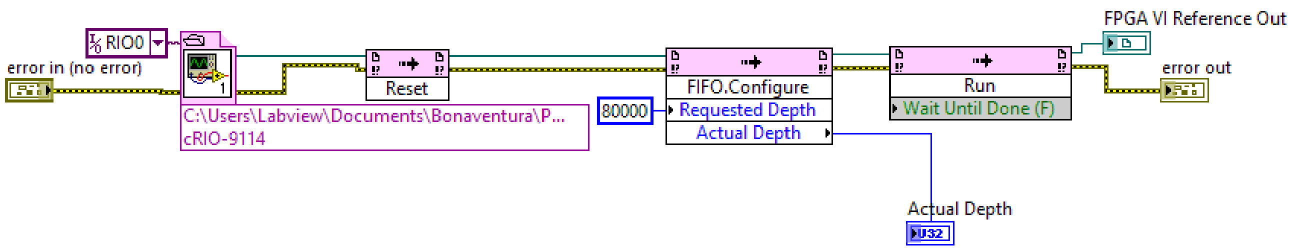

Figure B.4 – Labview RT Subprogram "Connect to FPGA"

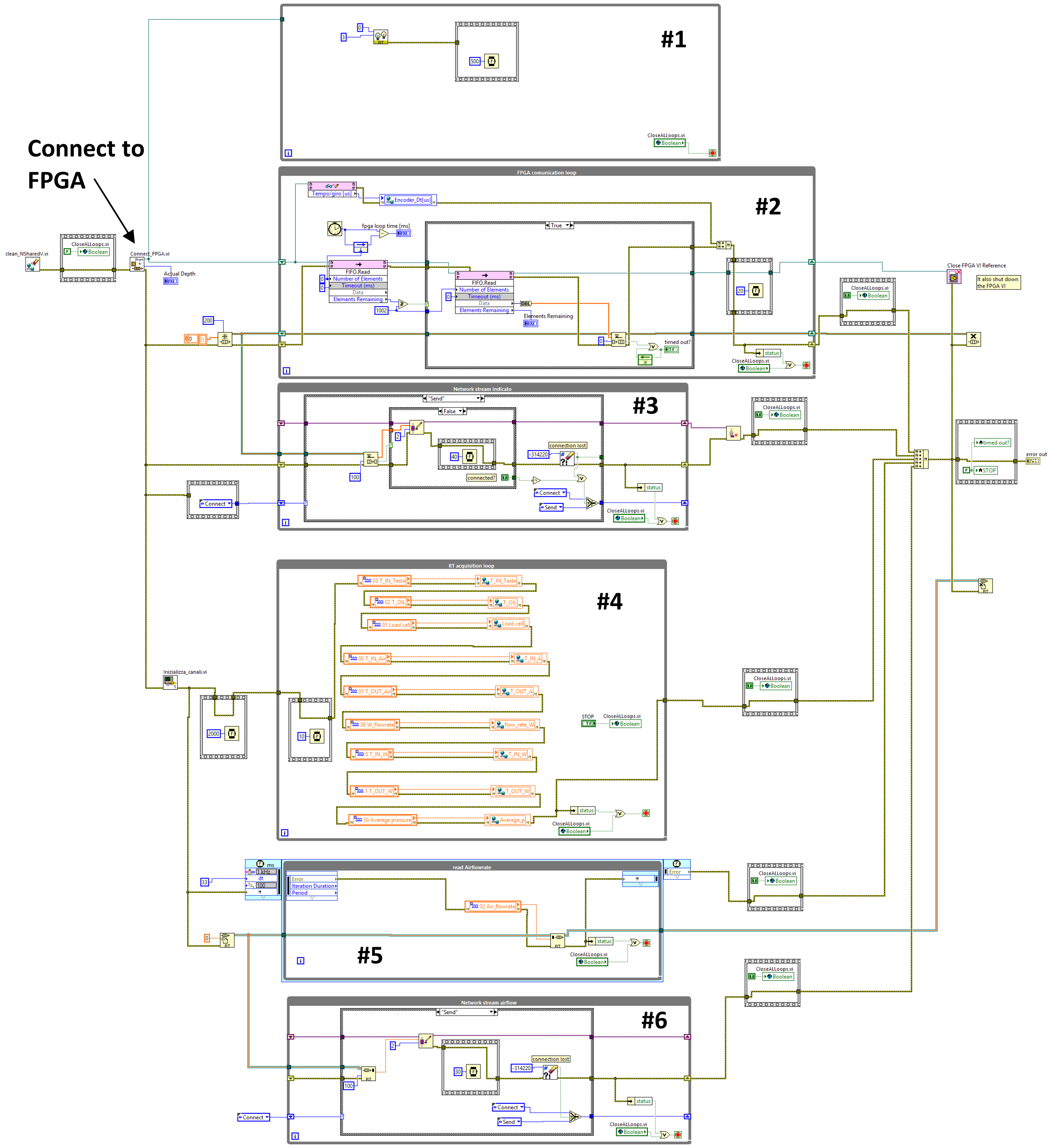

Figure B.5 – Labview RT code for the compressor test bench

B3 Host code

Figure B.6 shows the code of the Host program. It is made up by 9 while loops. The general structure of the Host program and RT program are similar, except that the Host program have to handle also the user interface and the data saving. There are two loops in series and then other parallel seven loops.

- The first two loops aim is to connect the Host program to the queued data stream sent by the RT program. When the two connections are established, then the core of the program runs.
- The third loop is ready to take the instantaneous pressure data from the fourth loop and write them into two text files: one for the indicated pressure and the other for the pressure in cylinder head. The loop is generally inactive. When the user gives the command, it starts its duties.
- The fourth loop handle the Network Stream containing the instantaneous pressure data from the RT program. First, it must divide the indicated pressure data from the cylinder head pressure data. Then, it converts the voltage signal to a pressure value and send them to the monitor as pV or pθ diagrams. When the user gives the “save” command, it starts sending the data to loop #3.
- The fifth loop read the Network Published Shared Variables containing the average pressure and the load cell data. Then, it filters their values through the moving average technique. At last, it sends the averaged values to the sixth loop through local variables.
- The sixth loop reads the data sent by the fifth loop and the eighth loop. It also reads all the other Network Published Shared Variables. Then, it applies a scale to the current value from the water flow rate meter, it converts the time elapsed per revolution into round per minute (RPM) and radians per second, it converts the force acquired by the load cell into the motor torque. All these data are sent to the computer screen to be monitored. The data are also collected into an array. Whenever the user gives the “save” command, the array is sent to loop #7.
- The seventh loop is usually idle. Whenever the user gives the “save” command, the data sent by loop #6 are written into a text file with an appropriate header.
- The eighth loop reads the Network Stream containing the air flow rate data and performs a harmonic analysis to determine the fundamental frequency. Then, this value is converted into the correspondent air flow rate value and sent to the sixth loop to be monitored.
- The ninth loop calculates the temperature variations that helps the user to determine whether thermal stationary conditions are reached.

Figure B.7 shows the user interface for monitoring and control. There are all the indicators that monitors the acquired sensors. There are also the “Save” button and the “Stop” button (needed to stop the application). There are also some buttons and indicators to monitor and handle minor problems related to the Network Streams.

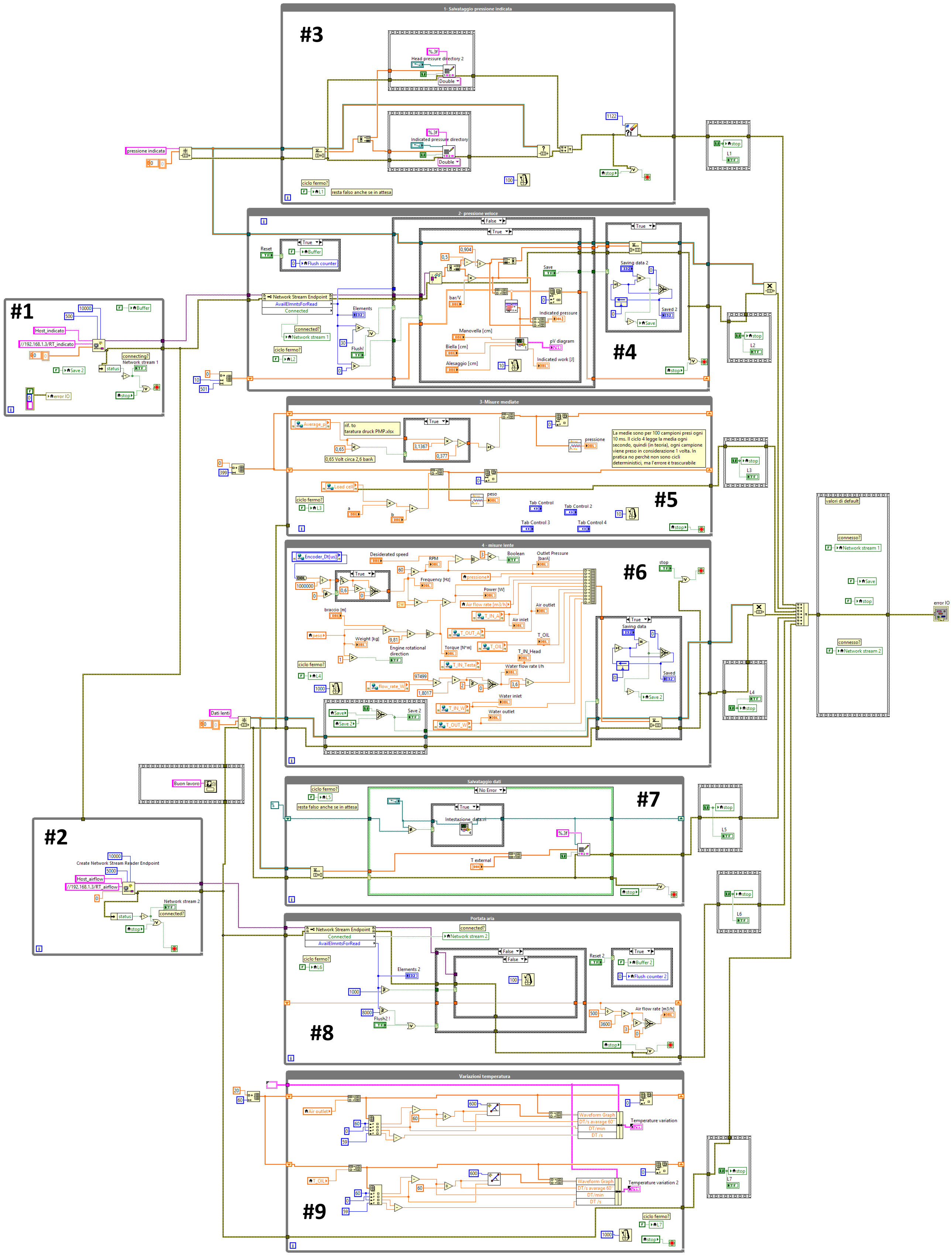

Figure B.6 – Labview Host code for the compressor test bench

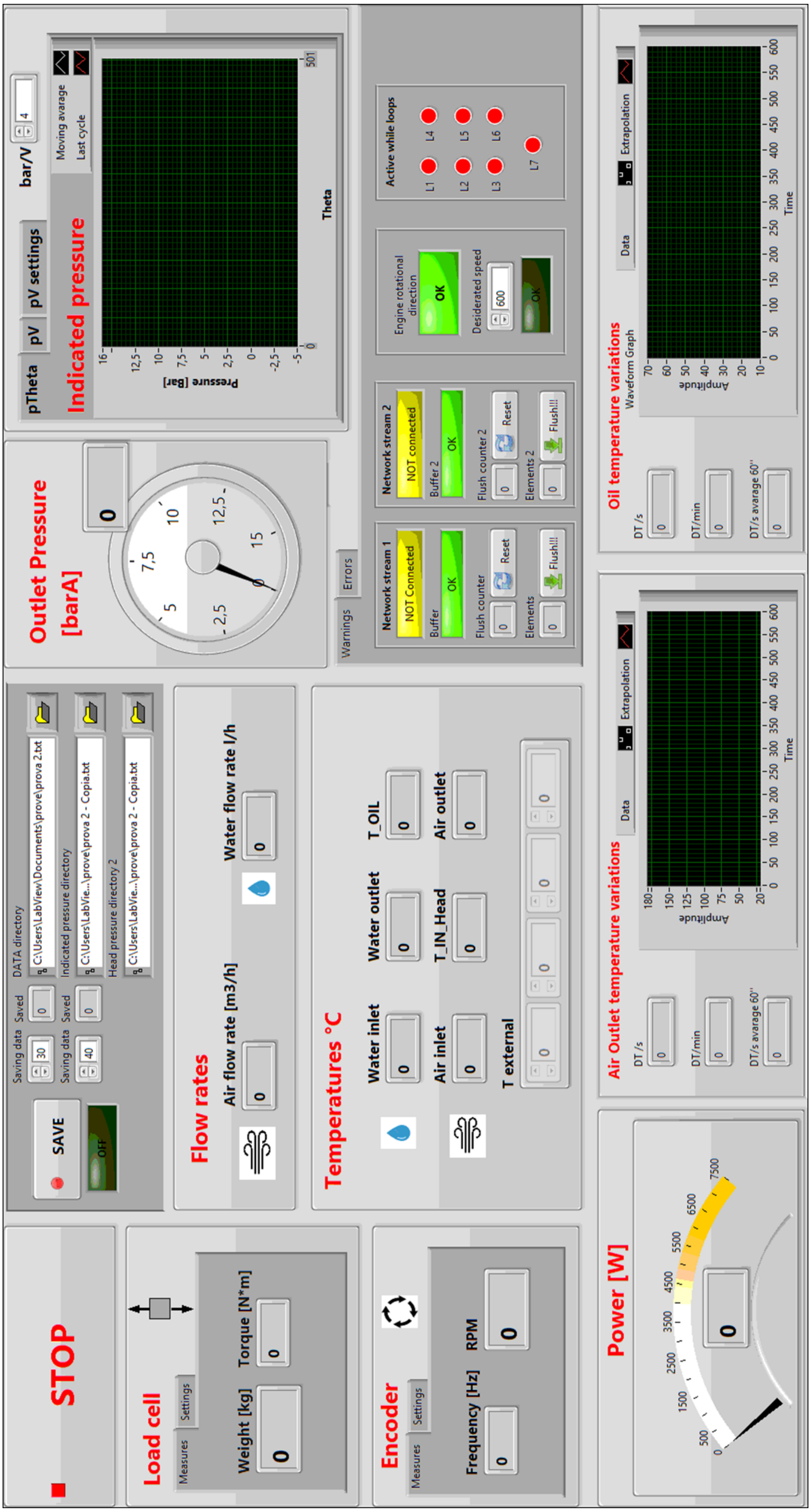

Figure B.7 –User interface of the Host program

Appendix C Compressor specifications

This appendix shows some details on the compressor used for the experimental activities illustrated in chapter 3. The compressor is an open type compressor.

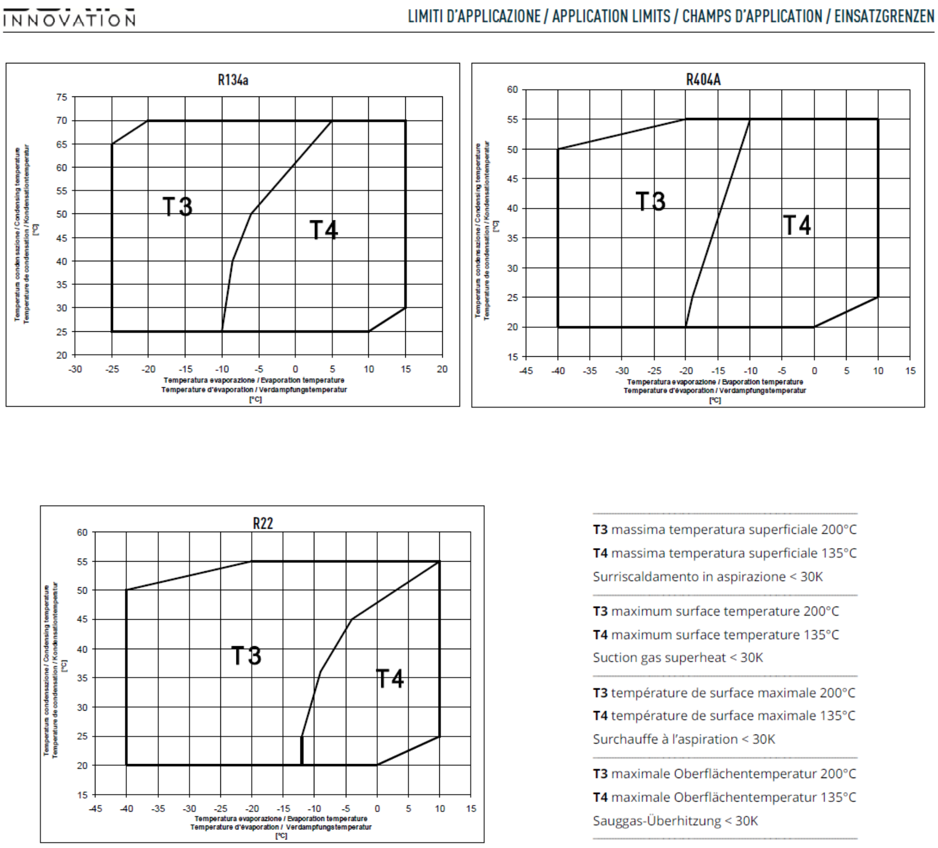

Cilindrata Swept volume Cylindrée Hubvolumen [cm³]	Aspirazione Suction Aspiration Saugventil SL [mm]	Scarico Discharge Refoulement Druckventil DL [mm]	Carica olio Oil charge Charge huile Ölfüllung [kg]	Peso Weight Poids Gewicht [kg]
27,2	10s	10s	0,4	11
34,0	10s	10s	0,4	11
43,1	12s	12s	0,4	11
54,4	12s	12s	0,4	11
76	5/8" - 16	1/2" -12	0,5	17
170	3/4" - 18	5/8" - 16	1,0	22
351	28s	3/4" - 18	1,5	38
560	28s	22s	3,0	78
560	35s	28s	3,0	78
560	35s	28s	3,0	82

Appendix D Valve control system

The main technical issue about classical reciprocating expanders are the controlled valves. The inlet valve control has strict requirements: the inlet valve should be open for 10% to 50% of the piston stroke (δ=0.1-0.5), and even less if the pressure ratio (β) is over 6. Table D.1 collects the calculated requirements for the inlet valves if the expander must achieve a complete isothermal expansion (see also paragraphs 1.3.3 and 1.4.3). The cranking degrees are calculated on the simplified hypothesis that the piston moves following a perfect sinusoidal function. These data depend also on the dead volume, the cylinder bore, and the cubic size of the expander that were assumed to be 20 cm^3 , 6 mm, and 175 cm^3.

Table D.1 – Valves requirements for an isothermal expansion (calculated)

β	δ	Cranking degrees	Time [ms] (at 480 RPM)	Time [ms] (at 1000 RPM)
4	0,164	47,8°	16,6 ms	7,9 ms
5	0,109	38,5°	13,4 ms	6,4 ms
6	0,071	31°	10,8 ms	5,2 ms

Automotive cam follower systems open the valves for more than 100% of the piston stroke halving the cam speed. The expander requires a cam with the same speed of the crankshaft, so automotive cams could open the valves for no less than 50% of the stroke. Other mechanical systems may be studied in the future. Some possibilities are shown by Stouffs et al. [63]. However, at last, a control system based on electro-pneumatic components was chosen. The flexibility of this kind of systems was decisive in this choice.

A prototype of the system was built to test its possibilities. In figure D.1 the system scheme is shown.

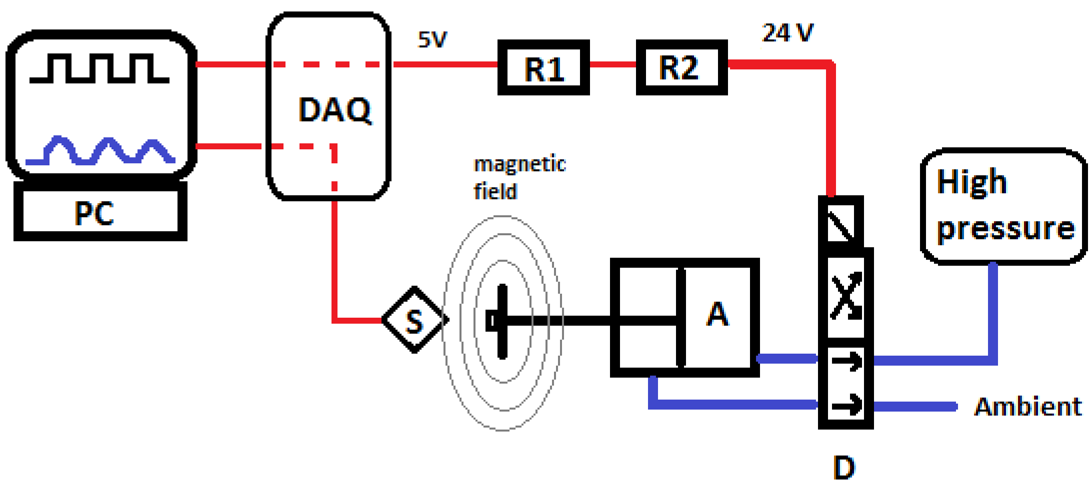

Figure D.1 – Scheme of the controlled valve system

A computer generates a square wave, and through a National Instruments DAQ board a digital signal is generated. Two electro-mechanical relays (R1 and R2) convert the 5V signal in a 24V signal. The electro-pneumatic distributor (D) gives high-pressure air to the pneumatic actuator (A) when the signal is high and opens the discharge path when the signal is low. The actuator is placed in double effect configuration, so the high-pressure air helps the valves return. A magnetic sensor (S) gives back a signal proportional to the valve displacement.

In figure D.2 the pneumatic distributor and the actuator are shown.

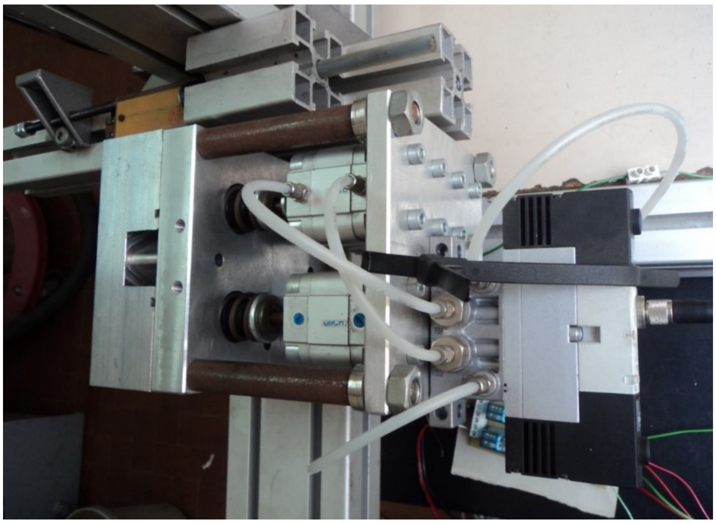

Figure D.2 – Pneumatic actuators and distributor

Figure D.3 shows the valves displacement over the time when controlled by a square wave at a frequency of 8Hz and a duty cycle of 20%. Two different valves are tested: a valve with a maximum lift of 5,5 mm and a valve with a maximum lift of 3,2 mm. Both failed the test, as the valves closes more than 25 ms after the stop signal (0 V). According to table D.1, 25 ms is more than the whole valve desired opening time at 480 RPM (8 Hz).

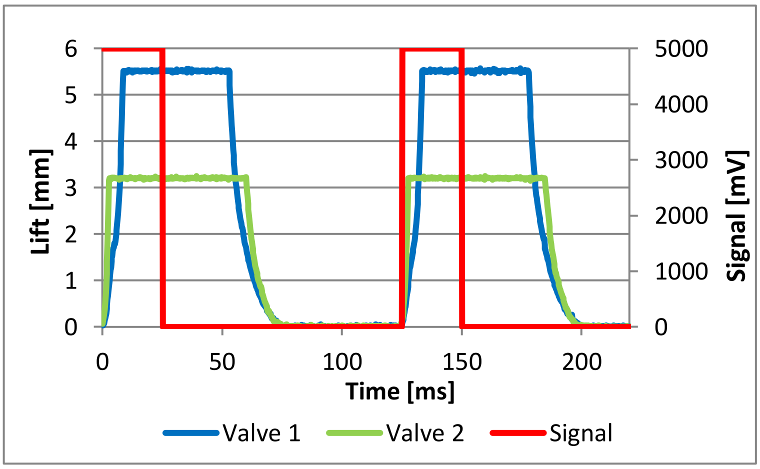

Figure D.3 – Experimental data: lift of the valves over time

The system has several problems. For example, the relays are time consuming components. Moreover, when the timing will be given by an encoder (to synchronize the valves to the crankshaft), the DAQ board will add more delay because the computer will have to process all the signals.

The next system will have the relays replaced with a MOSFET board (figure D.4). Moreover, the DAQ board will be replaced with a RIO board to bypass the computer.

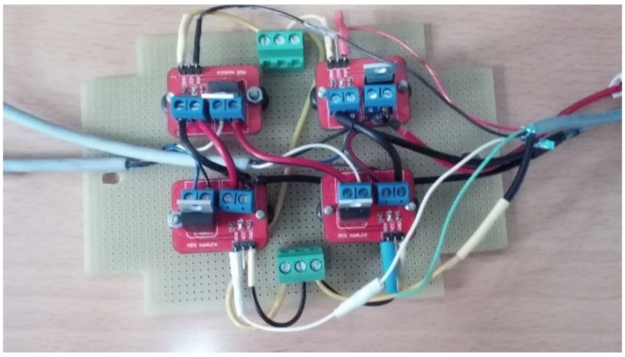

Finally, the machine architecture will follow the concept shown in chapter 5. This way, the inlet valve will have to be open for about the 100% of the piston stroke, increasing the available time to 30 ms at 1000 RPM.